

## Integrated photonics interrogator and sensors for ultrasound detection

Ouyang, B.

**DOI**

[10.4233/uuid:faaabafd-5087-4726-80f7-64ba5f864931](https://doi.org/10.4233/uuid:faaabafd-5087-4726-80f7-64ba5f864931)

**Publication date**

2020

**Document Version**

Final published version

**Citation (APA)**

Ouyang, B. (2020). *Integrated photonics interrogator and sensors for ultrasound detection*. [Dissertation (TU Delft), Delft University of Technology]. <https://doi.org/10.4233/uuid:faaabafd-5087-4726-80f7-64ba5f864931>

**Important note**

To cite this publication, please use the final published version (if applicable).  
Please check the document version above.

**Copyright**

Other than for strictly personal use, it is not permitted to download, forward or distribute the text or part of it, without the consent of the author(s) and/or copyright holder(s), unless the work is under an open content license such as Creative Commons.

**Takedown policy**

Please contact us and provide details if you believe this document breaches copyrights.  
We will remove access to the work immediately and investigate your claim.

**INTEGRATED PHOTONICS INTERROGATOR  
AND SENSORS FOR ULTRASOUND DETECTION**



# **INTEGRATED PHOTONICS INTERROGATOR AND SENSORS FOR ULTRASOUND DETECTION**

## **Proefschrift**

ter verkrijging van de graad van doctor  
aan de Technische Universiteit Delft,  
op gezag van de Rector Magnificus prof. dr. ir. T. H. J. J. van der Hagen,  
voorzitter van het College voor Promoties,  
in het openbaar te verdedigen op vrijdag 17 juli 2020 om 10:00 uur

door

**Boling OUYANG**

Master of Science in Nanoscale Engineering  
École Centrale de Lyon, Écully, France  
geboren te Hengyang, China.



Dit proefschrift is goedgekeurd door:

promotor prof. dr. ir. L. J. van Vliet en copromotor dr. J. Caro

Samenstelling promotiecommissie:

Rector Magnificus,  
Prof. dr. ir. L. J. van Vliet,  
Dr. J. Caro,

voorzitter  
Technische Universiteit Delft  
Technische Universiteit Delft

*Onafhankelijke leden:*

Prof. dr. P. G. Steeneken  
Prof. dr. ir. R. F. G. Baets  
Dr. G. van Soest  
Dr. N. Bhattacharya  
Dr. K. W. A. van Dongen  
Prof. dr. B. Dam

Technische Universiteit Delft  
Ghent University - IMEC  
Erasmus Medical Center  
Technische Universiteit Delft  
Technische Universiteit Delft  
Technische Universiteit Delft, reservelid



The work in this dissertation was conducted at Computational Imaging Group of the Department of Imaging Physics, Faculty of Applied Sciences, Delft University of Technology and was financially supported by Nederlandse Organisatie voor Wetenschappelijk Onderzoek.

*Cover designed by:* Erwin Suvaal  
*Printed by:* Ridderprint B.V.

Copyright © 2020 by B. Ouyang

ISBN 978-94-6375-972-4

An electronic version of this dissertation is available at  
<http://repository.tudelft.nl/>.

# CONTENTS

<b>Summary</b>	<b>vii</b>
<b>Samenvatting</b>	<b>ix</b>
<b>1 Introduction</b>	<b>1</b>
1.1 Integrated photonics	2
1.1.1 The concept of integrated photonics	2
1.1.2 Integrated photonics components and devices	3
1.1.3 Photonic integration platforms used in this research	12
1.2 Ultrasound transducers and imaging	13
1.2.1 Piezoelectric transducer	13
1.2.2 CMUT and PMUT	14
1.2.3 Ultrasound imaging	15
1.3 Optical ultrasound sensors	17
1.4 Research goals and thesis outline	20
References	22
<b>2 Integrated photonics interferometric interrogator for a ring-resonator ultrasound sensor</b>	<b>27</b>
2.1 Introduction	28
2.2 Ring-resonator ultrasound sensor and MediGator design	29
2.2.1 Ring-resonator ultrasound sensor	29
2.2.2 MediGator design	30
2.3 Interrogation procedure and matching of the MediGator and the ring-resonator sensor	32
2.3.1 Interrogation procedure	32
2.3.2 Matching of the MediGator and the ring-resonator sensor	33
2.4 Characterization of the ring-resonator sensor, the light source and the Mach-Zehnder interferometer	35
2.5 Experiments with the MediGator	37
2.5.1 Measurement of the frequency response of the sensor	37
2.5.2 Interrogation experiments	38
2.6 Conclusion and outlook	40
References	42
<b>3 On-chip silicon Mach-Zehnder interferometer sensor for ultrasound detection</b>	<b>45</b>
3.1 Introduction	46
3.2 Sensor design and fabrication	47

3.3	Characterization of the acoustic properties of the sensor . . . . .	48
3.3.1	Transfer function. . . . .	48
3.3.2	Sensitivity . . . . .	50
3.4	Conclusion and outlook. . . . .	52
3.5	Addendum: membrane buckling effect . . . . .	53
	References . . . . .	58
<b>4</b>	<b>Silicon ring resonators with a free spectral range robust to fabrication variations</b>	<b>61</b>
4.1	Introduction . . . . .	62
4.2	Design method . . . . .	63
4.2.1	Ring-resonator design with a robust free spectral range . . . . .	63
4.2.2	Calibration of the design inputs using the systematic width deviation . . . . .	65
4.3	Design implementation. . . . .	66
4.4	Experiment results . . . . .	67
4.5	Conclusion and outlook. . . . .	70
4.6	Addendum: silicon MZIs with a free spectral range robust to fabrication variations . . . . .	71
	References . . . . .	74
<b>5</b>	<b>Conclusion and Outlook</b>	<b>77</b>
5.1	Conclusion . . . . .	78
5.2	Outlook . . . . .	79
5.2.1	Applying the MZI ultrasound sensor to intravascular photoacoustic imaging . . . . .	79
5.2.2	Developing an array of MZI ultrasound sensors . . . . .	81
5.2.3	Developing an array of RR sensors and its interrogator. . . . .	82
	References . . . . .	84
<b>A</b>	<b>Appendix A: The chip layouts for the two multi-project wafer runs</b>	<b>87</b>
<b>B</b>	<b>Appendix B: Post-processing steps for sensor fabrication</b>	<b>91</b>
<b>C</b>	<b>Appendix C: Packaging steps for the silicon MZI ultrasound sensor</b>	<b>95</b>
	<b>Acknowledgement</b>	<b>99</b>
	<b>Curriculum Vitæ</b>	<b>103</b>
	<b>List of Publications</b>	<b>105</b>

# SUMMARY

Ultrasound transducers are devices that can generate and detect ultrasound waves. These waves are widely used in many applications, including ultrasound imaging and non-destructive testing. For medical applications, such as intravascular ultrasound imaging, there is an increasing demand of miniaturization of ultrasound transducers, to reach lateral element dimensions down to  $100\ \mu\text{m}$  or even smaller. This is rather challenging for conventional piezoelectric transducers. Manufacturing techniques new for this purpose, such as diamond-saw cutting and laser cutting, have to be pushed to their limits to reach these small dimensions in this context. The electrical wiring of an array of such small elements is also labor intensive and challenging, while the dense wiring may lead to electrical cross talk between the elements of the array.

Ultrasound sensors based on integrated photonics devices provide a new solution to meet the miniaturization demand for the detection functionality of transducers. An important example is the silicon ring-resonator (RR) ultrasound sensor developed in our department. This sensor combines a small footprint with a high sensitivity and a low detection limit. Compared with piezoelectric transducers, it has additional advantages of low cost, mass producibility, and immunity to electromagnetic interference. It is also possible to build an array of these RR sensors on a single chip. These merits make the sensor appealing for ultrasound detection in general. However, there are three challenges that have arisen from this previous work on the RR ultrasound sensor. These challenges relate to specific properties of such silicon RR ultrasound sensors and to the high sensitivity of silicon integrated photonics devices to fabrication variations. More specifically, difficulties in interrogating RR ultrasound sensors need to be overcome. Further, inherent drawbacks of RR ultrasound sensors need to be addressed, suggesting to look for an alternative silicon integrated photonics ultrasound sensor. Finally, design methods need to be developed for making RRs and Mach-Zehnder interferometers (MZIs), which are widely used in silicon photonics, robust to fabrication variations. This thesis addresses the three challenges sequentially.

A compact interrogator (called MediGator) comprising a specially designed light source and an InP integrated photonics chip has been developed for interrogating RR ultrasound sensors. The light source provides a high power density, a suitable bandwidth, and a large tuning range. Each of these properties are designed to meet the critical interrogation demands of a RR sensor. The InP chip consists of an MZI with a  $3 \times 3$  multimode interferometer and has a small footprint. Thus, the temperature of the whole chip can be well controlled during the interrogation. The interrogation procedure is mathematically presented, giving the optimum design of the MZI. The MediGator is used for measuring the frequency response of a RR sensor and its sensitivity at the resonance frequency. Interrogation experiments show a high interrogation performance. In comparison with the results from the modulation method, the previously used interrogation method, the MediGator has a much wider measurement range for ultrasound pressures, easier operation,

better temperature robustness, higher compactness, and lower cost.

We have developed a silicon MZI ultrasound sensor to overcome the limitations of the RR ultrasound sensor. One spiral arm of the MZI is located on a thin membrane, which works as the sensing part. Ultrasound waves excite the membrane's vibrational mode, thus inducing modulation of the optical transmission of the MZI. Unlike a RR, an MZI does not have enhancement of the optical field in its waveguides, which enables higher optical input power without the penalty of strong nonlinear effects. The higher input power contributes to a high sensitivity and a low detection limit, i.e., better sensor performance. In addition, the transmission of the MZI sensor is a more gradual function compared to the sharp peak or dip of a RR sensor. This characteristic makes the alignment between the light source and the sensor spectrum easier and more robust. Experimentally determined properties of the MZI ultrasound sensor are a high sensitivity, a low detection limit, and a large dynamic range. The sensor properties can be further tailored to meet the requirements of specific applications. In the addendum of the chapter on the MZI sensor, the effects of initial stress in the membrane are discussed.

Variations of geometrical device features are inherent to various fabrication steps of silicon photonics, leading to fabrication variations. Due to the strong light confinement and the nanometer-scale dimensions of silicon photonic devices, the device properties are rather sensitive to these fabrication variations. We have proposed and demonstrated a generic design method for silicon RRs with a free spectral range (FSR) robust to the waveguide-width variations originating from the fabrication. The systematic width deviation of the foundry is first extracted from a comparison of experimental results from a series of test MZIs with simulation results. Then, the systematic width deviation is used to calibrate the design inputs for a more accurate design of RRs. According to the design method, two waveguide widths are used in a single RR. Fabrication-induced width variations have opposite effects on these two waveguides with respect to the FSR, thus compensating the width-dependent FSR variations. Compared to normal designs, i.e., RRs designed with a single width and using the un-calibrated design inputs, the robust RRs show a clear decrease of the FSR variation and of the deviation from the nominal FSR value. The experimental results show a good match with the predictions of the method. We further propose a similar method for silicon MZIs with a robust FSR, based on two waveguide widths for the arms of the MZI. The developed design methods can be used for integrated photonic circuits comprising many RRs and MZIs.

In the outlook, we indicate how this work can be continued in the follow-up research. The MZI sensor properties can be tailored for developing an all-photonic solution for intravascular photoacoustic imaging. Moreover, an array of MZI ultrasound sensors can be built on a single chip. It is also possible to develop an array of RR sensors on a single chip, in combination with a dedicated integrated photonics interrogator for such an array.

# SAMENVATTING

Ultrageluid-transducenten zijn devices die ultrageluidgolven kunnen genereren en detecteren. Deze golven worden vaak gebruikt in allerlei toepassingen, waaronder beeldvorming met ultrageluid en niet-destructief testen. Voor medische toepassingen, bijvoorbeeld intravasculaire echografie, is er een toenemende vraag naar miniaturisering van ultrageluid-transducenten, om laterale afmetingen van de elementen te bereiken tot  $100\ \mu\text{m}$  of kleiner. Voor conventionele piezoelektrische ultrageluid-transducenten is dit een aanzienlijke uitdaging. Fabricagetechnieken die nieuw zijn voor dit doel, zoals snijden met een diamantzaag en een laserstraal, moeten in deze context tot het uiterste gedreven worden. Het aanbrengen van elektrische bedrading aan een array van dergelijk kleine elementen is arbeidsintensief en uitdagend, terwijl de dichte bedrading kan leiden tot overspraak tussen de elementen van de array.

Ultrageluidsensoren gebaseerd op geïntegreerde fotonica bieden een nieuwe oplossing die kan voldoen aan de vraag naar miniaturisering aangaande de detectiefunctie van transducers. Een belangrijk voorbeeld is de ultrageluidsensor gebaseerd op een silicium ringresonator (RR), die in onze afdeling is ontwikkeld. Deze sensor combineert een kleine afmeting met een hoge gevoeligheid en lage detectielimiet. Vergeleken met piezoelektrische transducenten, heeft de sensor bijkomende voordelen van lage kosten, de mogelijkheid tot massaproductie en immuniteit tegen elektromagnetische interferentie. Bovendien is het mogelijk een array van deze RR sensoren te vervaardigen op één chip. In het algemeen gesproken, maken deze gunstige eigenschappen de sensor aantrekkelijk voor de detectie van ultrageluid. Er zijn echter ook drie uitdagingen die zijn voortgekomen uit dit eerdere werk aan deze RR ultrageluidsensor. Deze uitdagingen zijn gerelateerd aan de specifieke eigenschappen van de silicium RR ultrageluidsensoren en aan de hoge gevoeligheid van silicium geïntegreerde fotonische devices voor fabricagevariaties. Meer specifiek, moeten moeilijkheden bij het uitlezen van RR ultrageluidsensoren overwonnen worden. Verder moeten inherente nadelen van RR ultrageluidsensoren geadresseerd worden, waarbij de suggestie is te zoeken naar een alternatieve ultrageluidsensor gebaseerd op silicium geïntegreerde fotonica. Tot slot is het nodig ontwerpmethoden te ontwikkelen om RRn en Mach-Zehnder interferometers (MZIs), die vaak gebruikt worden in de silicium fotonica, robuust te maken ten opzichte van fabricagevariaties. In dit proefschrift worden de drie uitdagingen achtereenvolgens aangegaan.

Een compact uitleesapparaat (genoemd MediGator), bestaande uit een special ontworpen lichtbron en een chip gebaseerd op InP geïntegreerde fotonica, is ontwikkeld voor het uitlezen van RR ultrageluidsensoren. De lichtbron heeft een hoge vermogensdichtheid, een geschikte bandbreedte en een groot afstemmingsbereik. Elk van deze eigenschappen is ontworpen om te voldoen aan de kritische eisen aan het uitlezen van een RR sensor. De InP chip bestaat uit een MZI met een  $3 \times 3$  multimodale interferometer en heeft een kleine afmeting. Daardoor kan de temperatuur van de totale chip goed gestabiliseerd worden tijdens het uitlezen van de sensor. De MediGator is gebruikt voor het

meten van de frequentiearakteristiek van een RR sensor en van zijn gevoeligheid bij de resonantiefrequentie. Uitleesexperimenten laten zien dat de uitleesprocedure zeer goed werkt. Vergeleken met resultaten verkregen met de modulatiemethode, die eerder gebruikt werd, heeft de MediGator een veel breder meetbereik voor de aangeboden ultrageluiddruk. Verder is de MediGator makkelijker te bedienen, meer robuust ten opzichte van temperatuurinvloeden, compacter en bovendien goedkoper.

Om de beperkingen van RR ultrageluidsensoren te overwinnen hebben wij een silicium ultrageluidsensor ontwikkeld die gebaseerd is op een MZI. Eén van beide spiraalvormige armen van de MZI bevindt zich op een dun membraan, dat werkt als het sensorgedeelte. Ultrageluidgolven exciteren een vibratietoestand van het membraan, waardoor modulatie wordt geïnduceerd van de optische transmissie van de MZI. In tegenstelling tot een RR, vertoont een MZI geen versterking van het optische veld in zijn golfgeleiders. Dit maakt het mogelijk hogere optische ingangsvermogens te gebruiken zonder het nadelige gevolg van niet-lineaire effecten. Het hogere ingangsvermogen draagt bij aan een hogere gevoeligheid en een lagere detectielimiet, d.w.z. betere prestatie van de sensor. Bovendien is de transmissie van de MZI sensor een meer geleidelijke functie van de optische golflengte dan de scherpe piek of het scherpe dal van een RR sensor. Deze eigenschap vergemakkelijkt het afstemmen van de lichtbron op het spectrum van de sensor en maakt de afstemming robuuster. Experimenteel bepaalde eigenschappen van de MZI sensor zijn verder een hoge gevoeligheid, een lage detectielimiet en een groot dynamisch bereik. Deze sensoreigenschappen kunnen verder toegesneden worden om te voldoen aan specifieke toepassingen. In het addendum van het hoofdstuk over de MZI sensor worden de effecten van initiële spanning in het membraan bediscussieerd.

Variaties van geometrische device-eigenschappen zijn inherent aan verscheidene fabricagestappen van silicium fotonica, leidend tot fabricagevariaties. Als gevolg van de sterke opsluiting van licht en de nanometerschaal afmetingen van silicium fotonische devices, zijn de eigenschappen van de devices nogal gevoelig voor deze fabricagevariaties. Wij hebben een generieke ontwerpmethodode voorgesteld en gedemonstreerd voor silicium RRn met een vrij spectraal bereik (VSB) dat robuust is ten opzichte van variaties van de golfgeleiderbreedte veroorzaakt door de fabricage. De systematische afwijking van de breedte als geleverd door de fabricagefaciliteit is eerst bepaald uit een vergelijking van experimentele resultaten van een reeks test MZIs met simulatieresultaten. Vervolgens is deze systematische afwijking van de breedte gebruikt om de ontwerp-invoerwaarden te calibreren, voor een nauwkeuriger ontwerp van RRn. Volgens de voorgestelde ontwerpmethodode worden twee golfgeleiderbreedtes gebruikt in één RR. Breedtevariaties veroorzaakt door de fabricage hebben een tegenovergesteld effect op de waveguides met verschillende breedte ten opzichte van het VSB, zodat VSB variaties afhankelijk van de breedte gecompenseerd worden. Vergeleken met normale ontwerpen, d.w.z. RRn ontworpen met één breedte en gebaseerd op de niet-gecalibreerde ontwerp-invoerwaarden, laten robuuste RRn een duidelijk afname zien van de VSB variatie en van de afwijking van de nominale VSB waarde. De experimentele resultaten komen goed overeen met de voorspellingen van de methode. Verder stellen wij een vergelijkbare methode voor om silicium MZIs te ontwerpen met een robuust VSB, gebaseerd op twee golfgeleiderbreedtes voor de armen van de MZI. De ontwikkelde ontwerpmethododes kunnen gebruikt worden voor geïntegreerde fotonische circuits opgebouwd uit vele RRn en MZIs.

In het vooruitzicht wordt aangegeven hoe dit werk voortgezet kan worden in vervolgonderzoek. De sensoreigenschappen van de MZI kunnen afgestemd worden op een te ontwikkelen geheel fotonische oplossing voor intravasculaire foto-akoestische beeldvorming. Tevens kan een array van MZI ultrageluidsensoren gebouwd worden op één chip. Het is ook mogelijk een array van RR sensoren op één chip te ontwikkelen, in combinatie met een specifiek uitleesapparaat voor een dergelijke array.





# 1

## INTRODUCTION

This chapter starts with providing background knowledge relevant to the research reported in the chapters to follow. In particular, in Section 1.1 the concept of integrated photonics is presented, together with the photonic components and devices used extensively in this work. In Section 1.2 a brief introduction is given to ultrasound transducers and imaging, followed in Section 1.3 by a short overview of the state-of-the-art in the field of optical ultrasound sensors and a discussion of challenges we encountered for integrated photonics ultrasound sensors at the start of this research. Finally, in Section 1.4 the research goals are formulated, together with the thesis outline.

## 1.1. INTEGRATED PHOTONICS

### 1.1.1. THE CONCEPT OF INTEGRATED PHOTONICS

To arrive at the concept of integrated photonics, which is the optical or photonic counterpart of integrated electronics, it is helpful to first discuss guiding of light by a structure with a higher refractive index than that of the surrounding material. For this, the classic experiment of the Swiss physicist Jean-Daniel Colladon is used here, which is the first documented demonstration [1] of the guiding of light, also called optical waveguiding. In his experiment, Colladon showed that light can be guided by a stream of water in air, leading to the curved water light guide shown in Figure 1.1(a). This phenomenon is based on total internal reflection (TIR) at the interface between water and air. The experiment indeed satisfies the condition for TIR, since the refractive index of water ( $n \approx 1.33$ ) is higher than that of air ( $n = 1$ ).

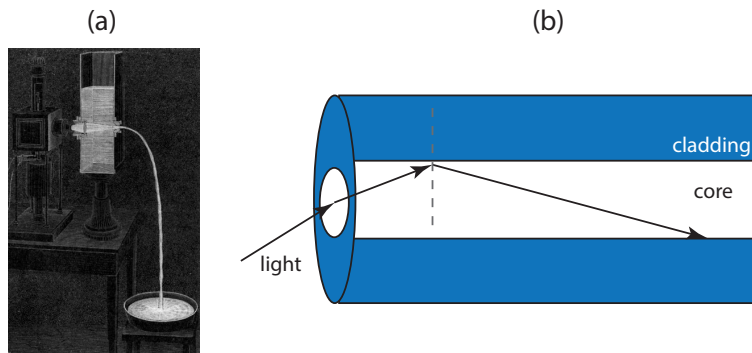


Figure 1.1: (a) Colladon's light guide [1]: a water container is emptied via a hole, giving a water stream shaped as a curved cylinder. Illumination of the water exit leads to guiding of light by the water stream as a result of total internal reflection (TIR). (b) Light coupled into an optical fiber, also leading to guiding of light as a result of TIR.

The waveguiding principle of Colladon's experiment has turned out to be extremely important, since it is applied all over the world in fiber optic communication for transmitting information over very long distances. Fiber optic communication is a method to send light pulses, usually of a wavelength in the telecom C-band (around 1550 nm), from a sender to a receiver through an optical fiber that acts as a waveguide. Thanks to the superior properties of fused silica from which optical fibers are fabricated, fiber optic

communication is an extremely powerful technique, characterized by a large bandwidth, immunity to electromagnetic interference, low loss and low cost. It has enabled many important applications, the most salient one being the Internet. A schematic of an optical fiber is shown in Figure 1.1(b). The cylindrical fiber core is covered by the cladding, which has a slightly lower refractive index than that of the core. The diameter of the core is often on the order of the wavelength of the light, but also can be much larger. For the right insertion angle at the fiber input, light pulses in the fiber will undergo TIR and propagate along its length, to deliver pulse-coded information to a receiver at the fiber end.

Miniaturized versions of the optical fiber, fabricated in an appropriate material system, have led to optical waveguides on a chip. Photonic circuits that can be made from these define the field of integrated photonics, in analogy to the field of integrated electronics. Integrated photonics encompasses all aspects of photonic integrated circuits (PICs). Including more complex functional structures into the circuit enables dedicated functionalities of PICs [2, 3]. Integrated photonics has taken off as an important enabling technology for many applications in the last decades. This is the result of exploiting the highly developed nanofabrication techniques of nanoelectronics in developing various photonic platforms based on different material systems. In the telecommunication field, integrated optical transceivers and receivers are beneficial to high-speed communication systems [4–6]. In the sensing field, integrated photonic sensors have many advantages. Sensors based on integrated photonics have been developed to sense temperature [7, 8], strain [9], pressure [10], ultrasound [11], and chemical components [12].

### 1.1.2. INTEGRATED PHOTONICS COMPONENTS AND DEVICES

The photonic part of the acoustic sensors and interrogator in Chapters 2 and 3, and the structures in Chapter 4 are essentially small integrated photonics circuits, comprising various components and devices. Therefore, the photonics of the components and devices is discussed here in short.

#### The optical waveguide

The basics of the guiding of light by an optical waveguide are often introduced using the infinite dielectric slab waveguide. A schematic of a symmetric waveguide of this type is presented in Figure 1.2, which shows a core layer sandwiched between identical and thick cladding layers. The three layers have infinite extent in the  $y$ - and  $z$ -direction. Similar to the fiber case, the index of the core is higher than that of the cladding layers. The thickness of the core is on the order of the wavelength or thicker. For the present purpose, the guided modes propagate in the  $z$ -direction and are supposed to be transverse electric (TE). For the geometry of Figure 1.2, the electric field of TE modes is in the  $y$ -direction. In homogeneous media, the solutions of Maxwell's equations are plane waves. For the slab waveguide, translation invariance holds in the  $z$ -direction. This suggests that the following plane wave describes the TE modes [13]:

$$E_y(x, z, t) = E_y(x) \exp[i(\omega t - \beta z)], \quad (1.1)$$

where  $E_y(x, z, t)$  and  $E_y(x)$  are the electric field of the guided mode and its mode profile, respectively. The modes are characterized by the propagation constant  $\beta$ . This is the wavevector of the guided mode, which by definition points in the propagation direction

of the mode. The mode profile is  $y$ -independent.  $\omega$  is the angular frequency of the guided light. By substituting the trial solution Eq. 1.1 into the wave equation [13] that results from Maxwell's equations, one arrives at the following wave equation:

$$\frac{\partial^2 E_y}{\partial x^2} + (k_0^2 n_i^2 - \beta^2) E_y = 0, \quad (1.2)$$

in which  $k_0 = \omega/c$  ( $c$  is the speed of light in vacuum) is the vacuum wavevector of the monochromatic light exciting the guided mode.  $n_i$  is the index of the  $i^{\text{th}}$  layer, with  $i = \text{core, cladding}$ . For  $k_0 n_{\text{cladding}} < \beta < k_0 n_{\text{core}}$ , the solutions of Eq. 1.2 are the profiles of a series of guided modes. The profiles and the related  $\beta$ -values can be found analytically and with arbitrary precision. This is done by solving the Eq. 1.2 in each layer and connecting the solutions by applying the boundary conditions for the electric and magnetic field at the interfaces between the layers, and by numerically solving the eigenvalue equation that involves  $\beta$ . The resulting  $\beta$ -values are discrete and numbered by  $m$ , their number is finite and the highest value corresponds to the lowest order mode. The number of guided TE modes that can exist in the slab increases stepwise with increasing core thickness, decreasing wavelength and increasing contrast of the indices of the core and the claddings.

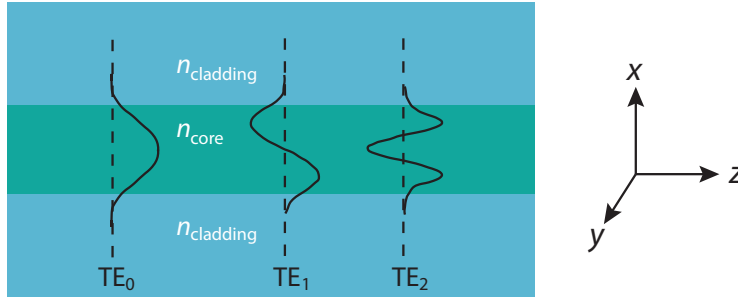


Figure 1.2: Schematic of the slab waveguide.

Based on  $\beta$ , one often defines the effective index  $n_e$  of the mode under consideration:

$$n_e = \frac{\beta}{k_0}. \quad (1.3)$$

$n_e$  is a measure for the reduction of  $\beta$  compared to  $k_0 n_{\text{core}}$ , the value of the vacuum wavevector in the core layer. To calculate the optical path length travelled by a guided mode in the waveguide,  $n_e$  is used instead of  $n_{\text{core}}$ . Since  $\beta$  depends on the wavelength  $\lambda$ ,  $n_e$  depends on wavelength as well. This dependence is expressed in the group velocity, which is defined by:

$$n_g = n_e - \lambda \frac{dn_e}{d\lambda}. \quad (1.4)$$

The lowest three mode profiles  $TE_0$ ,  $TE_1$  and  $TE_2$ , are schematically indicated in Figure 1.2. The tails of the profiles, which describe the evanescent field, extend into the cladding layers. The fields of the TE modes are fully defined by  $E_y$ ,  $H_x$  and  $H_z$ , with  $H_x$  and  $H_z$  the magnetic field in the respective directions. Apart from the TE modes, transverse magnetic (TM) modes can exist in the slab, with field components  $H_y$ ,  $E_x$  and  $E_z$ . Treatment of the TM case is along similar lines as summarized above for the TE case.

Practical waveguides are photonic wires, in which light is confined in two directions and is free to propagate in the third direction. A widely applied type of photonic wire is the so-called ridge waveguide, which has a rectangular cross section. In Figure 1.3(a) the cross section of a ridge waveguide is shown, in this case with a silicon ridge, the cladding material all around the ridge being silicon dioxide. In practice, such a ridge waveguide is fabricated using lithography and dry etching, applied to a thin layer of waveguiding material on a substrate, whether it is silicon or another dielectric waveguiding material. After the etch, a dielectric layer is deposited onto the waveguide to act as the upper cladding.

The wave equation for the ridge waveguide reflects light confinement in two dimensions, meaning that the mode profile and the refractive index in this case depend on both  $x$  and  $y$ :  $E = E(x, y)$  and  $n = n(x, y)$ . By solving the wave equation and applying boundary conditions [13], approximate solutions can be obtained for the mode profiles and the discrete  $\beta$ -values. The mode profiles are now numbered by the two numbers  $n$  and  $m$ . The profiles are the product of two orthogonal modes, one for confinement in the  $x$ -direction and the other for confinement in the  $y$ -direction. Again the modes can be TE or TM.

Nowadays, it is common practice to obtain waveguide modes by numerically solving Maxwell's equations using commercial software, e.g., Lumerical [14] and COMSOL [15]. Figure 1.3(b) and (c) show the TE and TM mode profiles for the waveguide in Figure 1.3(a), respectively, simulated using COMSOL. Simulations also lead to other waveguide properties, for example, the effective index and the group index.

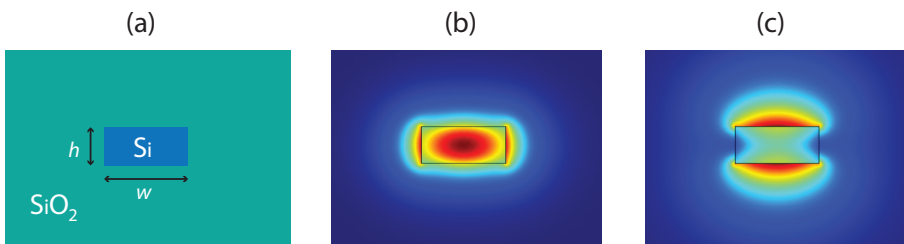


Figure 1.3: Geometry and modes of a silicon ridge waveguide. (a) Cross section of the waveguide with silicon dioxide cladding. The waveguide width and height are 450 nm and 220 nm, respectively. (b)  $TE_{00}$  mode of the waveguide in (a). (c)  $TM_{00}$  mode of the waveguide in (a). The colors in (b) and (c) indicate the magnitude of the electrical field. Note that for the  $TE_{00}$  mode electrical field is strongest inside the core, while for  $TM_{00}$  it is strongest immediately outside the core.

### The directional coupler

The evanescent field of a mode of a waveguide, a feature of the mode profiles in Figure 1.3, can penetrate a second waveguide that is in close proximity. This leads to excitation

of a mode or modes in the second waveguide and thus to coupling of optical power to the second waveguide. This phenomenon of coupling of power from one waveguide to another is used in a directional coupler, which is schematically depicted in Figure 1.4. The coupler has one input port and two output ports, which are called the pass port and the coupled port. Usually, the two waveguides of the coupler are single mode and identical. For an input power  $P_{\text{in}}$  and neglecting propagation loss, coupled mode theory leads to the powers transferred to the output ports [16]:

$$P_{\text{pass}} = P_{\text{in}} \cos^2 [\kappa(\lambda)L_c + \kappa_0(\lambda)] , \quad (1.5)$$

$$P_{\text{coupled}} = P_{\text{in}} \sin^2 [\kappa(\lambda)L_c + \kappa_0(\lambda)] . \quad (1.6)$$

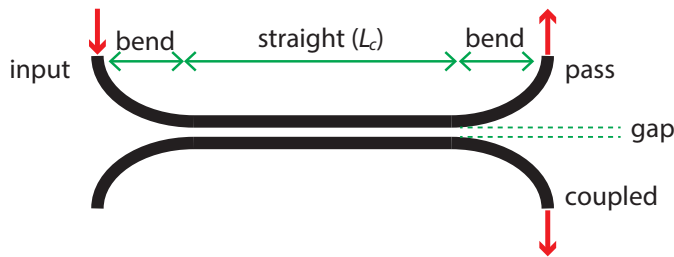


Figure 1.4: Schematic of a directional coupler. The coupling length  $L_c$  of the straight section of the coupler and the bend sections are indicated.

Here  $\kappa(\lambda)$  is the electric field coupling coefficient that describes the coupling strength in the straight section of the coupler, which has length  $L_c$ .  $\kappa(\lambda)$  depends on the difference between the effective indices of the odd and even supermodes of these two waveguides. A larger difference leads to a higher value of  $\kappa(\lambda)$ .  $\kappa_0(\lambda)$  is the electric field coupling coefficient of the bend sections, which depends on the bend geometry. The dispersion of  $\kappa(\lambda)$  and  $\kappa_0(\lambda)$  arises from the wavelength-dependence of the waveguide mode. To avoid a high sensitivity of the directional coupler to fabrication variations, a very narrow gap is not preferred. Starting from small  $L_c$ , the power  $P_{\text{coupled}}$  increases with increasing  $L_c$ , to reach the value  $P_{\text{in}}$  of 100 % coupling for the right value of  $L_c$ . The behavior beyond that point is oscillatory, as described by Eq. 1.6. For any  $L_c$  and in agreement with power conservation,  $P_{\text{pass}}$  and  $P_{\text{coupled}}$  add up to  $P_{\text{in}}$ . By design, the splitting ratio  $P_{\text{coupled}}/P_{\text{in}}$  can thus be varied continuously in the range  $[0,1]$ .

### The ring resonator

The ring resonator (RR) is a commonly used photonic device. It is a waveguide that is looped back to itself to form a ring. The ring is evanescently coupled to one or two bus waveguides, using one or two directional couplers that closely resemble the coupler design depicted in Figure 1.4. This leads to the all-pass RR or add-drop RR shown in Figure

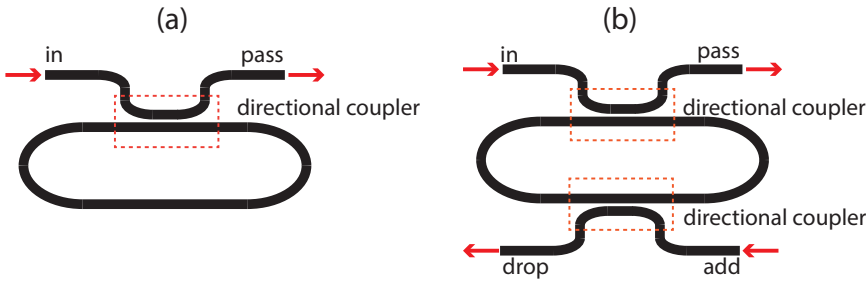


Figure 1.5: The two usual ring-resonator geometries, with the ring shaped as a racetrack. The directional couplers, indicated by the dashed boxes, serve to evanescently couple light between the ring and the bus waveguides. (a) All-pass ring resonator and (b) Add-drop ring resonator.

1.5. The ring is not necessarily circular, but can take many shapes, for example, the shape of a racetrack as in Figure 1.5.

When the optical path length of the ring equals an integer number of wavelengths, a resonance occurs in the ring. The resonance is characterized by an enhanced optical field in the ring. At resonance, the resonance wavelengths  $\lambda_r$  meet the resonance condition, which is given by:

$$k\lambda_r = Ln_e. \quad (1.7)$$

Here,  $k$  is an integer numbering the order of the resonance,  $L$  is the circumference of the ring and  $n_e$  is the effective index of the waveguide mode circulating in the ring. The distance between adjacent resonance wavelengths is the free spectral range (FSR, indicated in Figure 1.6):

$$\text{FSR} = \frac{\lambda^2}{n_g L}. \quad (1.8)$$

Here,  $n_g$  is the group index. In this thesis, only add-drop RRs are used. Assuming that the two directional couplers of the add-drop RR are identical, the transmissions at the drop port and the pass port are given by, respectively [17]:

$$T_p = \frac{r^2 a^2 - 2r^2 a \cos\theta + r^2}{1 - 2r^2 a \cos\theta + (r^2 a)^2}, \quad (1.9)$$

$$T_d = \frac{(1 - r^2)^2 a}{1 - 2r^2 a \cos\theta + (r^2 a)^2}. \quad (1.10)$$

Here,  $r$  is the self-coupling coefficient, defined as the electric field transmission coefficient of the bus waveguide resulting from its coupling to the ring.  $a$  is the electric field transmission coefficient of the ring for a single round trip, which includes the propagation loss in the ring and the loss in the directional couplers.  $\theta = \beta L$  is the accumulated phase of the



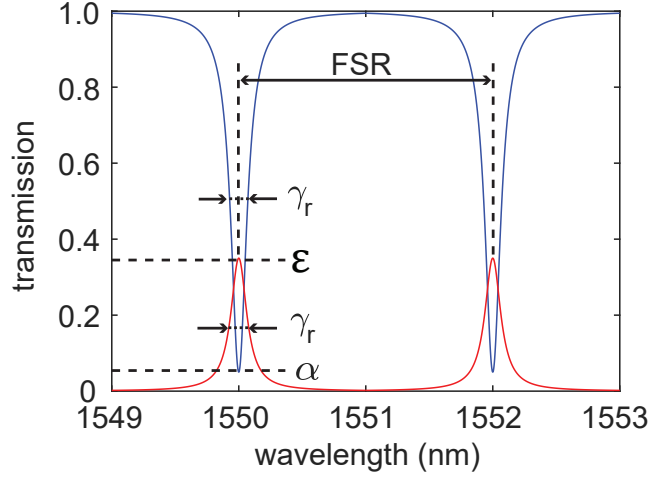


Figure 1.6: The transmissions functions  $T_p$  and  $T_d$  of an add-drop RR, for the pass-port configuration (blue curve) and the drop-port configuration (red curve). Resonance occurs at the positions of the peaks and dips. The parameters are:  $\text{FSR} = 2 \text{ nm}$ ;  $\gamma_r = 150 \text{ pm}$ ,  $\epsilon = 0.35$  and  $\alpha = 0.05$ .

circulating mode in the ring for a single round trip.  $\beta$  is the propagation constant of the mode. The self-coupling coefficient is calculated from the coupling ratio  $P_{\text{pass}}/P_{\text{in}}$  of the directional couplers, which follows from Eq. 1.5:

$$r = \sqrt{(P_{\text{pass}}/P_{\text{in}})}. \quad (1.11)$$

For wavelengths  $\lambda$  close to  $\lambda_r$ , the phase  $\theta$  can be approximated by:

$$\theta = \frac{2\pi}{\lambda} n_e(\lambda)L \cong 2\pi m - 2\pi n_g(\lambda_r)L \frac{\lambda - \lambda_r}{\lambda_r^2}. \quad (1.12)$$

This approximation leads to the following expressions for the transmissions  $T_p$  and  $T_d$ :

$$T_p \approx \frac{(\lambda - \lambda_r)^2 + \alpha (\gamma_r/2)^2}{(\lambda - \lambda_r)^2 + (\gamma_r/2)^2}, \quad (1.13)$$

$$T_d \approx \frac{\epsilon}{1 + \frac{(\lambda - \lambda_r)^2}{(\gamma_r/2)^2}}. \quad (1.14)$$

Here,  $\alpha$ ,  $\gamma_r$  and  $\epsilon$  are given by:

$$\alpha = \frac{r^2(1-a)^2}{(1-r^2a)^2}, \quad (1.15)$$

$$\gamma_r = \frac{\lambda_r^2(1-r^2a)}{\pi n_g L r \sqrt{a}}, \quad (1.16)$$

$$\varepsilon = \frac{(1 - r^2)^2 a}{(1 - r^2 a)^2}. \quad (1.17)$$

$\alpha$  and  $\varepsilon$  are the transmission level at  $\lambda_r$  in the pass-port and the drop-port configuration, respectively.  $\gamma_r$  is the full width at half minimum or the full width at half maximum, both abbreviated by FWHM, of the dip or peak described by Eq. 1.13 or Eq. 1.14, respectively. The quality factor of the RR is  $\lambda_r/\gamma_r$ . The line-shape function given by Eq. 1.13 for  $T_p$  can be written as  $[1 - (1 - \alpha)\Lambda(\lambda)]$ , with  $\Lambda(\lambda)$  a Lorentzian function of maximum value unity, centered at  $\lambda_r$ . The line-shape function given by Eq. 1.14 can be written as  $\varepsilon\Lambda(\lambda)$ . In Figure 1.6 plots are presented of the transmissions functions  $T_p$  and  $T_d$ , for the parameters given in the figure caption. Near the resonance wavelengths of 1550 nm and 1552 nm the line shapes closely resemble the approximate transmission functions given by Eqs. 1.13 and 1.14.

### The multimode interferometer

The multimode interferometer (MMI) is a photonic component for merging and splitting of light. An MMI consists of a wide, multimode center waveguide and a number of single mode input and output waveguides connected to the center waveguide [18]. In general, an MMI is referred to as an  $M \times N$  MMI, where  $M$  and  $N$  are the number of input and output waveguides, respectively. In Figure 1.7 an  $1 \times 2$  and a  $3 \times 3$  MMI are sketched.

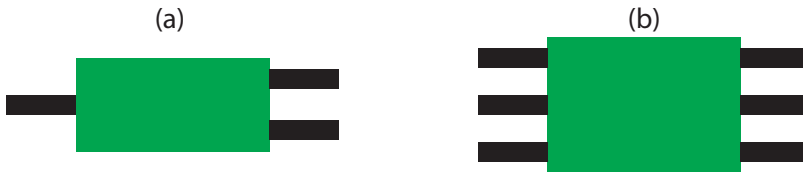


Figure 1.7: Two examples of an MMI: (a)  $1 \times 2$  MMI. (b)  $3 \times 3$  MMI. The black waveguides are single mode waveguides, while the green waveguide is a multimode waveguide.

The light entering the multimode waveguide from an input waveguide is decomposed into the modes that can exist in the central section, where these modes propagate, each with its own propagation constant. Because the multiple modes propagating in the central section are phase related, an interference pattern with field maxima and minima forms along the length of the central section, with the details of the pattern depending on the propagation distance. In case light is injected by several input waveguides, the interference pattern results from interference of the multiple modes excited by all the input waveguides together. By choosing the length of the center waveguide such that interference maxima occur exactly at the end of the center waveguide, and by placing output waveguides at the positions of these maxima, the light entered via the input waveguides can be distributed over the outputs in a pre-determined way. For example, an ideal  $1 \times 2$  MMI of the type in Figure 1.7(a) gives two identical outputs, each with half the power of the input. It thus works as a 50/50 light splitter. Based on the reversibility of the flow of light, the  $2 \times 1$  MMI can be used to combine light as well. An ideal  $3 \times 3$  MMI of the type

in Figure 1.7(b) gives three outputs, with a phase difference of  $120^\circ$  between each output. The power of the three outputs is the same.

### The Mach-Zehnder interferometer

In the late nineteenth century, Zehnder and Mach proposed and demonstrated a free space optics interferometric instrument [19, 20] that later became known as the Mach-Zehnder interferometer (MZI). Their MZI was capable of splitting the light from a single source into two beams, to define two optical paths, and of recombining these beams, to generate interference. Mach and Zehnder used their instrument to study the phase shifts between the two beams induced by insertion of a sample into one of the optical paths.

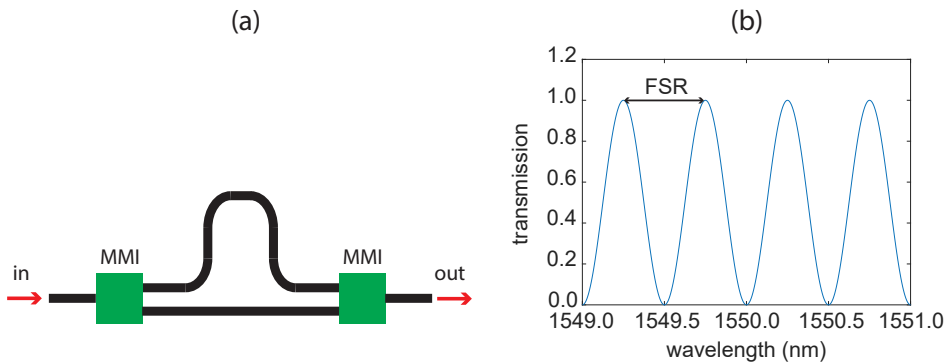


Figure 1.8: (a) Schematic top view of an integrated photonics MZI. (b) The transmission function of the MZI, according to Eq. 1.19. The FSR is 0.5 nm and the visibility is unity.

Nowadays, the MZI finds widespread use as an integrated photonics device for signal processing and sensing. In Figure 1.8(a), a schematic top view is given of an integrated photonics MZI, where the narrow waveguides are single mode waveguides with effective index  $n_e$  and group index  $n_g$ . Monochromatic light offered by the input waveguide is split by a  $1 \times 2$  MMI into two light paths, using two waveguide arms. The arms, which have a path length difference  $\Delta L$ , are merged in a  $2 \times 1$  MMI, where the arriving guided modes interfere. The path length difference gives a phase difference  $\varphi$  of the interfering modes. In the ideal case, the resulting transmission of the MZI is a cosine that as a function of  $\varphi$  oscillates between zero and unity. The transmission function is given by [21]:

$$T_{\text{MZI}} = \frac{1}{2} [1 + \cos \varphi] = \frac{1}{2} \left[ 1 + \cos \left( \frac{2\pi}{\lambda} n_e(\lambda) \Delta L \right) \right]. \quad (1.18)$$

Equation 1.18 describes how a phase difference caused by a path-length difference is converted to a transmission value and thus to a value of the output power of the MZI. Phase-difference changes caused by changes of  $n_e$  or  $\Delta L$  translate to transmission changes, which is the basis of sensing with an integrated photonics MZI. For sensing with the MZI, one typically chooses an operation wavelength such that the changes of  $n_e$  or  $\Delta L$  induce the highest transmission change and thus the strongest sensing signal. These are the wavelengths for which  $\partial T_{\text{MZI}} / \partial \lambda$  is maximum.

In practice, an MZI is subject to imperfections and environmental influences. These can be accounted for by introducing additional parameters  $p$ ,  $q$  and  $\varphi_e$ , leading to

$$T_{\text{MZI}} = \frac{1}{2} \left[ p + q \cos \left( \frac{2\pi}{\lambda} n_e(\lambda) \Delta L + \varphi_e \right) \right] \approx \frac{1}{2} \left[ p + q \cos \left( \frac{2\pi}{\text{FSR}} \lambda + \psi_e \right) \right]. \quad (1.19)$$

The ratio  $q/p$  is the fringe visibility, which is unity in the ideal case.  $\varphi_e$  is a phase offset that includes effects due to imperfections of the MZI and due to environmental influences. The right side of Eq. 1.19 follows by making the practical approach that the period of the transmission function plotted versus wavelength, i.e., FSR of the MZI, is virtually constant in a limited wavelength range. In that case,  $\psi_e$  includes  $\varphi_e$  and an additional phase offset related to this approach. Figure 1.8(b) shows a plot of the transmission function given by Eq. 1.19, in which the  $p = q = 1$  and FSR is given by:

$$\text{FSR} = \frac{\lambda^2}{n_g \Delta L}. \quad (1.20)$$

### The grating coupler

The grating coupler is a component for the coupling of light between a chip and a fiber. It is a periodic grating consisting of grating lines shallowly etched in the silicon layer. In Figure 1.9 the grating lines are illustrated in cross section as rectangular grating teeth. The figure also shows a fiber that offers light to the coupler. The period of the grating is  $p_g = \lambda/n_e$ , where  $n_e$  is the effective index of the guided mode propagating through the grating. As  $n_e$  is different for the TE mode and the TM mode, a grating coupler is polarization dependent. The grating couplers of our devices only work for the TE mode. A fill factor of 0.5 is often used in a grating coupler. Light is coupled from the fiber into the chip through diffraction at the grating. It is designed to use the first order diffraction maximum for incoupling and outcoupling of light [22]. However, other diffraction orders can be present as well. When the first diffraction order couples out at  $90^\circ$  with respect to the surface of the grating coupler, the second diffraction order will reflect back into the waveguide, which may lead to unwanted light interference. To avoid this reflection, the grating coupler is detuned to couple light out at a small angle  $\phi = 10^\circ$  with respect to the surface normal [see Figure 1.9(a)]. With air cladding, a coupling efficiency of 31% has been obtained for wavelengths around 1550 nm [22]. The coupling efficiency of the grating coupler is mainly limited by two factors: i) Not all the light from the waveguide is coupled upward towards the fiber. There is also quite some light transmitted, diffracted and reflected to other directions. ii) There is a mismatch between the coupling field towards the fiber and the fiber mode. Several methods for improving the coupling efficiency are proposed in [22]. The easiest way would be depositing an oxide cladding on top of the grating, which increases the fraction of coupled light because it gives a smaller refractive index mismatch for light passing from the chip to the fiber and vice versa.

As indicated, in the common use of a grating coupler for incoupling of light, the fiber is oriented at an angle  $\phi = 10^\circ$  above the coupler. Light can be outcoupled from the chip to the fiber in the same way. For packaging of photonics chips, the vertical fiber is replaced by an angle polished fiber shown in Figure 1.9(b). By choosing the proper polishing angle,

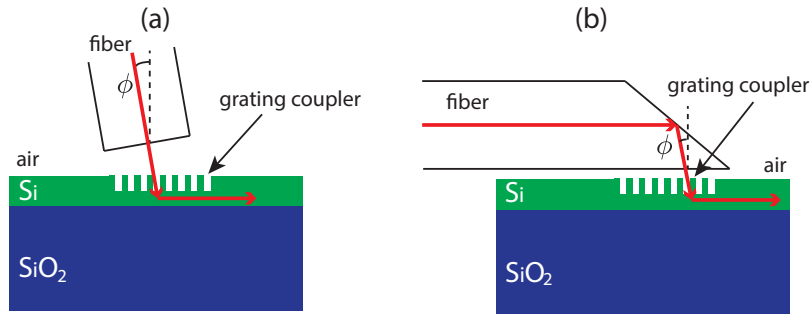


Figure 1.9: Two ways of using a grating coupler: (a) Light coupled into a waveguide from an almost vertical fiber and (b) Light coupled into a waveguide from an angle polished fiber.

total internal reflection happens at the fiber facet, thus again directing the light to the grating coupler with the proper angle. The fiber can be glued on the chip using UV curable glue. This is called the planar fiber packaging method [23], which we used to package the sensors introduced in the Chapters 2 and 3 of this thesis. Because our sensors are operated in water, a reflecting layer of aluminum is deposited on the fiber facet to maintain the internal reflection.

### 1.1.3. PHOTONIC INTEGRATION PLATFORMS USED IN THIS RESEARCH

The above components and devices are passive structures, though in some cases provisions can be added for active external control of the photonic properties. For these passive photonics structures, silicon is a very suitable waveguiding material [24]. However, due to the indirect electronic bandgap of silicon, the silicon platform in general is unsuitable for active integrated photonic devices such as lasers and optical amplifiers. Silicon photonics is based on silicon-on-insulator (SOI) material, which is a highly developed material system. In essence, SOI material is a thin (few hundred nanometers thick), high grade single crystalline and lowly doped silicon layer on top of a thermal oxide. The oxide is thicker than the range of the evanescent field of the modes of the waveguides to be fabricated in the layer. As for fabrication technology, silicon photonics is based on the highly-developed fabrication process of advanced complementary metal-oxide-silicon (CMOS) technology of today's nanoelectronics, leading to low cost and high volume production of PICs. The refractive index contrast between the silicon core ( $n \approx 3.5$ ) and the silicon dioxide or air cladding ( $n \approx 1.5$  or 1) is high, giving strong light confinement in silicon waveguides. This enables compact PICs, because waveguides can be sharply bent without significant bending loss. Several foundries provide commercial silicon-photonics services, for example IMEC, CEA-Leti and AMF. The silicon photonic sensors and other silicon photonic structures for the research of this thesis were fabricated at IMEC (Leuven, Belgium), through the Europractice multi-project wafer (MPW) service [25].

For integrated photonics including active devices and photodetectors in addition to the passive structures and devices discussed above, platforms are available based on a material with a direct electronic bandgap. A prominent one is the platform based in InP,

a III-V material. Waveguides are patterned in an epitaxially grown InP/InGaAsP/InP layered structure. Guided modes propagate in the InGaAsP core, which is sandwiched between InP claddings. The index contrast of the InP platform is smaller than that of the SOI platform (InGaAsP:  $n \approx 3.4$  depending on concentration of the materials; InP:  $n \approx 3.2$ ), giving weaker light confinement and leading to larger bend radii. The PIC for the interrogator (see Chapter 2) was fabricated in InP technology by foundry SMART Photonics (Eindhoven, The Netherlands) [26].

## 1.2. ULTRASOUND TRANSDUCERS AND IMAGING

### 1.2.1. PIEZOELECTRIC TRANSDUCER

An ultrasound transducer is a device for conversion of electrical energy to ultrasound waves and vice versa. In this sense, such a transducer can both generate and sense ultrasound waves. The most widely applied ultrasound transducer is the piezoelectric transducer, in which a disk of piezoelectric material is the key component [27]. Such a material shows the piezoelectric effect, which originates from the material's electrical polarization properties. Upon application of an electrical field, the material deforms, and upon deformation an electrical field is generated that can be measured as an external voltage. The applied electrical field and the dimension change are linearly related around its equilibrium state. The piezoelectric effect can occur over a wide frequency range, from DC into the MHz range, making a piezoelectric material suitable as the base material for ultrasound transducers. The frequency spectrum of the disk vibrations shows resonances determined by its spatial dimensions: the fitting of an odd number of half the acoustic wavelength in the thickness of the disk. There is a whole class of piezoelectric materials. Among these are the piezoceramic lead-zirconate-titanate (PZT), today's main workhorse for ultrasound transducers, and the piezopolymer polyvinylidene fluoride (PVDF), which is better for sensing than for generating of ultrasound.

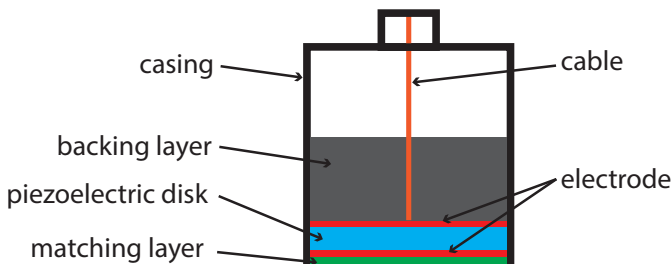


Figure 1.10: Cross section of a conventional piezoelectric transducer, showing its layered structure. The individual layers are: backing layer, upper electrode, piezoelectric disk, lower electrode, and matching layer. A transducer of this type is usually shaped as a cylinder, with a diameter on the order of a few cm to sub mm, depending on the application.

A cross section of a conventional piezoelectric transducer is presented in Figure 1.10. The piezoelectric disk is part of a layered structure with intimate contact between the lay-

ers. The disk has two planar electrodes to enable electrical actuation and sensing. The other layers are the backing layer inside the casing and the matching layer forming the interface to the medium into which ultrasound waves are transmitted. The backing layer is for providing mechanical damping of the vibrations of the piezoelectric disk and for reducing reflection at the inner face of the disk. These effects broaden the bandwidth of the resonances (usually, a transducer is optimized for the fundamental resonance, which is the strongest), to enable the sending and receiving of short ultrasound pulses, i.e., pulses with a certain frequency bandwidth. The broadening of the resonance bandwidth, however, is at the expense of the transducer sensitivity. In practice, the properties of the backing layer are chosen to obtain a good compromise between bandwidth and sensitivity.

The matching layer is for matching the characteristic acoustic impedance of the piezoelectric material to that of the medium into which acoustic waves are sent. The characteristic acoustic impedance  $Z_0$  is given by  $Z_0 = \rho_0 c_0$ , with  $\rho_0$  the equilibrium mass density of the material and  $c_0$  the equilibrium velocity of acoustic waves in the material. The matching layer is chosen such that optimum transfer of acoustic energy into the medium is obtained. The matching layer also has a damping effect.

The production technology of conventional piezoelectric transducers is mature and reliable. These transducers are widely and successfully used in many applications, e.g., ultrasound imaging and nondestructive testing. Disadvantages of the transducer result from thermal and electrical limitations. The poling of the piezoelectric material applied in manufacturing diminishes in time (thermal depoling) [27], gradually at room temperature and faster when used at elevated temperatures or by self heating as a result of the energy absorption by the backing layer. Depoling leads to reduced performance. Electrically, the transducer is sensitive to electromagnetic interference caused by signals from the environment. The effect of the acoustic design on the transducer's electrical impedance should be taken into account in the overall design of the electronics, including the wiring connected to the transducer, for optimum matching and optimum conversion between electrical and acoustic energy.

For medical applications, such as intravascular ultrasound imaging [28], there is an increasing demand for miniaturization of the piezoelectric transducer and for arrays of piezoelectric transducers with lateral dimensions of the individual elements down to 100  $\mu\text{m}$  or even smaller. Developments in this direction are challenging and involve new manufacturing techniques such as diamond-saw cutting and laser cutting. The electrical wiring of this kind of array is a challenging and labor intensive procedure, while the resulting dense wiring may give rise to electric cross talk between the individual elements of the array.

### 1.2.2. CMUT AND PMUT

To meet the demands for miniaturization of transducers and transducer arrays using devices other than the conventional bulk piezoelectric transducers, which use thickness-mode vibrations, micromachined ultrasound transducers (MUTs) have been developed. Benefiting from the type of mature fabrication techniques developed in microelectronics, MUTs with a small dimension and dense packing can be produced on wafer scale. There are two types of MUTs: capacitive micromachined ultrasonic transducers (CMUTs) and piezoelectric micromachined ultrasound transducers (PMUTs).

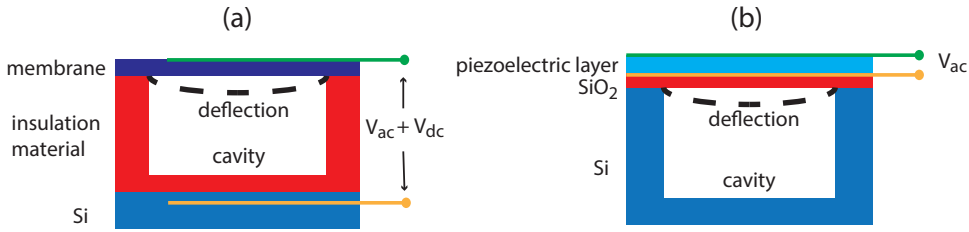


Figure 1.11: Schematic cross sections of (a) a capacitive micromachined ultrasound transducer (CMUT) and (b) a piezoelectric micromachined ultrasound transducer (PMUT), both with a membrane that covers a cavity.

As can be seen in Figure 1.11 (a), a CMUT is a box-type of cavity covered by a membrane [29]. The substrate and the membrane are both equipped with a planar electrode. This makes the device a capacitor, with the capacitance depending on the deflection of the membrane. The membrane can be made to vibrate and generate ultrasound waves by application of an AC voltage. Conversely, ultrasound-induced capacitance modulation leads to a measurable AC voltage. The frequency characteristic of a CMUT is determined by the membrane structure. It depends on the shape, dimensions, mechanical stiffness, and intrinsic stress of the membrane and on the boundary conditions that hold for the membrane [29]. For a high sensitivity, a high DC bias voltage is applied to the CMUT to enable the membrane collapse-mode [30]. However, this increases the risk of failure of the device.

PMUTs have a membrane structure as well [29], as shown in Figure 1.11 (b). A thin layer of piezoelectric material is deposited on the membrane. This layer works as the actuator of the membrane for generating ultrasound or a converter to transduce ultrasound-induced vibrations to an electrical signal, just like for the conventional piezoelectric transducer. The frequency response of a PMUT depends on the entire membrane, including the piezoelectric layer. Unlike CMUTs, PMUTs do not require a large DC bias, enabling integration with low voltage electronics. However, it is rather difficult to deposit a thin layer of high-performance piezoelectric material.

Compared to the piezoelectric transducers, the main operational component of MUTs shifts from piezo disk to a thin membrane with a well-designed vibrational mode. Proper design and fabrication of the membranes, which are layered structures, are crucial for the performance of the MUTs. Efficient modeling methods are needed for accurate prediction of the effects of the intrinsic stress of the membrane [29]. Since CMUTs and PMUTs are also electrical devices, they are not immune to electromagnetic interference. Proper electrical impedance matching is needed for the MUTs as well.

### 1.2.3. ULTRASOUND IMAGING

A main application of ultrasound transducers is ultrasound imaging, which is widely used for medical diagnosis [31]. A typical ultrasound image of a breast is given in Figure 1.12. Ultrasound imaging is based on the pulse-echo principle. The transducer emits a short ultrasound pulse, which travels towards the object via a medium. When the pulse arrives at the object, it partly reflects back as a result of the acoustic impedance difference, giving



an echo at the transducer and resulting in a transducer signal. As the speed of ultrasound in the medium is usually known, the distance between the transducer and the object can be calculated using the time delay between the emitted pulse and the received pulse. The amplitude of the echo signal is a measure of the difference of the acoustic impedance between the medium and the object. The stronger the echo, the larger is the acoustic impedance difference. An ultrasound image of a large object can be obtained by repeating this process using beam scanning, i.e., by placing the transducer at different positions or by mechanically rotating the transducer to steer the beam in different directions.

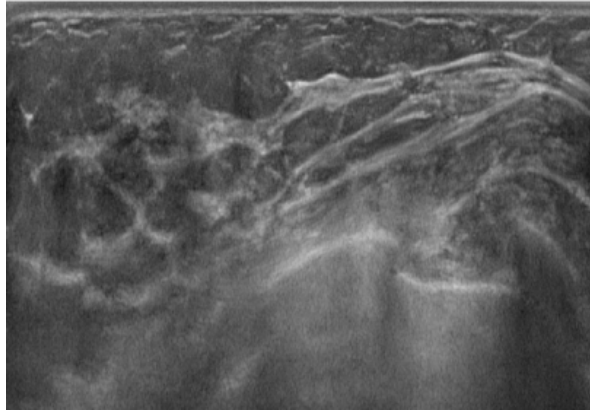


Figure 1.12: Breast ultrasound image obtained with the Siemens Acuson S2000 ultrasound system.

In modern ultrasound-imaging systems, an array of transducers is used instead of the mechanical beam scanning. Two types of transducer arrays exist: phased arrays and linear arrays. All elements of a phased array are used simultaneously. In the most flexible phased array systems, the signal amplitude, waveform and delay time of the pulse generated by each transducer element can be independently controlled, making it possible to adapt the beam shape or to steer the beam to different directions for covering the image plane. For a linear array, only a subset of the elements is used for a scan line. By varying the subset of elements sequentially across the transducer array, the whole image plane is covered.

The quality of an ultrasound image depends on the properties of the elements of the array and on the array itself. In general, the elements should have a high sensitivity, a low detection limit and operate in the desired frequency range. The high sensitivity and low detection limit enable a high signal-to-noise ratio. For clinical ultrasound imaging, the frequency range normally lies between 1 and 40 MHz. As ultrasound imaging is based on the pulse-echo principle, the axial resolution, which is the minimum distance that can be differentiated between two reflectors in the direction of beam propagation, is very important. A high axial resolution is obtained by using a short pulse length in time [32]. This requires a high operating frequency of the element (resulting in a short ultrasound wavelength) and a large bandwidth of the element (a broadband frequency domain signal gives a short time domain signal). It is worth to mention that the penetration depth of ultrasound waves decreases with increasing the frequency, which should be taken into account when selecting the operating frequency of the array element. The lateral reso-

lution, corresponding to the minimum distance that can be differentiated between two reflectors located perpendicular to the beam-propagation direction, is determined by the beam width of the generated ultrasound pulse, which varies with the distance between the object and the transducer [32]. The lateral resolution is high when the beam width is narrow. The lateral resolution can also be improved using special imaging techniques. For example, the synthetic aperture focusing technique (SAFT) [33] is used for this purpose. SAFT is based on delay-and-sum operations. It combines the signals of a series of measurements taken for different pulse-echo geometries of the ultrasound source, the object and the ultrasound receiver, the latter meaning the array element operating in sensing mode. Data summation gives constructive and destructive interference of the measured signals, leading to the reconstructed image. By using a large array that covers a large aperture, the interference of the measured signals gives an improved lateral resolution [34]. To have sufficient signal level from the edge of the aperture, a large opening angle of the single transducer element is desired. The latter is achieved by making the elements small with respect to the wavelength of the probing wave field.

### 1.3. OPTICAL ULTRASOUND SENSORS

Various types of optical ultrasound sensors are being developed to provide an alternative to the sensing functionality of the traditional piezoelectric transducers. There are two main types of optical ultrasound sensors: fiber-based ultrasound sensors and integrated photonics ultrasound sensors. Compared with piezoelectric transducers and MUTs, the optical sensors are immune to electromagnetic interference, while electrical impedance matching does not play a role. However, optical ultrasound sensors cannot generate ultrasound waves. Thus, an ultrasound source is needed. In photoacoustic imaging [28], in which ultrasound waves are generated by the tissue when absorbing incident light, an all-photonics solution can be realized for acoustic imaging by using an optical ultrasound sensor.

Fiber-based ultrasound sensors include fiber interferometric sensors [35, 36], Fabry-Perot cavities built in a fiber or on a fiber tip [37–39], and fiber Bragg gratings (FBGs) [40–43]. These sensors cover the sound-frequency range from kHz up to MHz. Some of these have high sensitivity and a low detection limit [38, 40]. The fiber interferometric sensors are scalable to an array [44]. However, miniaturization of fiber-based ultrasound sensors is rather difficult, because their sensitivity usually depends on the active length for sensing of the fiber. High sensitivity requires a long active length, leading to a large size. In addition, fiber-based ultrasound sensors of the types discussed do not lend themselves to cost effective and high volume production.

Integrated photonics ultrasound sensors have drawn a lot of attention recently. Compared to fiber-based ultrasound sensors, they have the important additional advantages of a small footprint, low cost, and mass producibility using highly developed microfabrication techniques, which are even CMOS compatible for sensors fabricated in SOI technology. A  $\pi$ -phase-shifted Bragg grating ultrasound sensor was developed in a SOI platform [45]. The sensor's response is dominated by the formation of surface acoustic waves. However, its directivity is rather limited and can only measure the ultrasound waves from specific angles.

RRs made in a polymer and a SOI platform were developed as ultrasound sensors as

well [11, 46–48]. The polymer RRs are located on a rigid substrate. Ultrasound waves induce deformation of the polymer, which via the optoelastic effect leads to a resonance-wavelength modulation that can be measured. In [46] a polymer RR sensor is demonstrated for ultrasound in the range of 1–75 MHz, giving a noise equivalent pressure (NEP) of 21.4 Pa. The realized bend radius of the ring in [46] is 40  $\mu\text{m}$ . To have a smaller bend radius, polymers with a higher refractive index than reported are needed.

The silicon RR sensor in SOI developed in our department is located on a thin membrane that is sensitive to ultrasound waves [11, 48], in the sense that ultrasound waves excite a vibrational mode of the membrane. The membrane vibration at ultrasound frequencies introduces oscillatory strain in the RR, causing modulation of the length and effective index of the ring. These, together with an effect of the dispersion, result in modulation of the resonance wavelength of the RR [9]. Experimental results show that this silicon RR sensor has high sensitivity of 2.1 mV/Pa and a NEP down to 0.4 Pa [11]. These favorable properties of this RR sensor, and the general appeal of an integrated photonics silicon sensor fabricated with CMOS compatible fabrication techniques, made further research with this sensor the starting point of the work in this thesis.

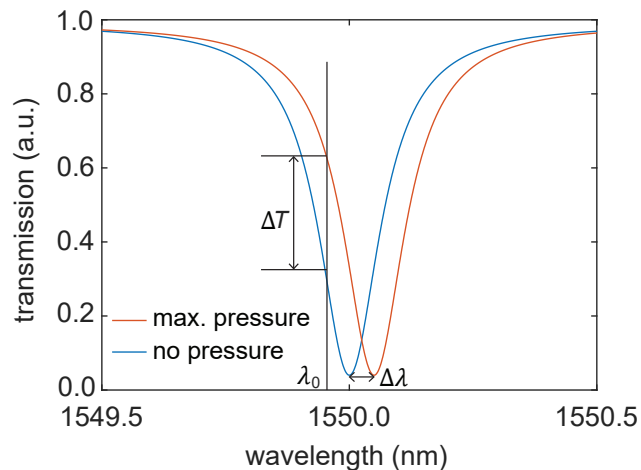


Figure 1.13: Snapshot of the ultrasound-induced modulation of the RR resonance. By using a fixed laser operation wavelength  $\lambda_0$ , the resonance shift  $\Delta\lambda$  is reflected as a transmission change  $\Delta T$ . Here, the sensing mechanism is explained for a resonance dip, but the sensing also works for a resonance peak.

As indicated, the oscillatory pressure of the ultrasound waves is translated to a modulation of the resonance wavelength of the RR. For reading out these RR sensors, the so-called modulation method is often used, which is based on a tunable laser and a high speed photodetector. As shown in Figure 1.13, the laser wavelength  $\lambda_0$  is aligned to the linear and steep flank of the resonance dip. The ultrasound-induced resonance-wavelength modulation leads to a transmission modulation at  $\lambda_0$ , which can be measured using the photodetector. The wavelength-dependent sensitivity of the sensor for this method can be defined as:

$$S(\lambda) = \eta I_{in} \left| \frac{dT}{dp_u} \right| = \eta I_{in} \left| \frac{dT}{d\lambda} \frac{d\lambda}{dp_u} \right| \approx \eta I_{in} \left| \frac{dT}{d\lambda} \frac{\Delta\lambda}{\Delta p_u} \right|, \quad (1.21)$$

where  $\eta$  is the net effect of the loss and gain in the entire light path.  $I_{in}$  is the optical input power,  $T$  is the transmission,  $p_u$  is the ultrasound pressure. For small pressure values, the sensor response is expected to be linear and both  $dT/d\lambda$  and  $\Delta\lambda/\Delta p$  are constant. Therefore, the sensitivity is proportional to  $|dT/d\lambda|$  at  $\lambda_0$ . By choosing  $\lambda_0$  such that  $|dT/d\lambda|$  is maximum, the sensitivity of the sensor is maximized.

Despite of the merits of the silicon RR ultrasound sensor, there are three main challenges that have to be met in relation to this sensor:

1. A better interrogation method is needed for the RR sensor. As mentioned above, the modulation method requires delicate alignment of the operation wavelength to the steep flank of a resonance dip (or peak). For a high value of  $|dT/d\lambda|$ , the RR should have a high quality factor, meaning the FWHM of the resonance dip or peak should be narrow. The typical FWHM of our RRs is about 100 pm. Since the resonance wavelength is very sensitive to the temperature (about 80 pm/K) [7], a small temperature change will lead to misalignment of the operation wavelength to the resonance, which can result in a (much) smaller sensitivity. Moreover, the narrow FWHM limits the maximum pressure that can be measured. When the resonance-wavelength modulation is large,  $|dT/d\lambda|$  can not be regarded as a constant anymore. This gives non-linear behavior of measured signal versus pressure, which is undesired. The tunable laser used in the modulation method is rather large and expensive, and thus is not so suitable. For real applications of the sensor, an interrogator is needed that can deal with the above limitations. In addition, this interrogator should be packaged as a single unit and portable.
2. Disadvantages of the RR sensor itself need to be overcome. The possibility to have a high sensitivity of the sensor by using a high input power as suggested by Eq. 1.21 is rather limited. This is due to the enhancement of the electrical field in the ring at resonance, as a result of which significant nonlinear effects will start to occur at relatively low optical input power (starting at about 0.3 mW [49]). This will cause self-heating of the ring and bistability of the resonance. A low optical input power limits the sensitivity of the sensor and the signal-to-noise ratio of the sensor signal.
3. Design methods for silicon photonics devices, in particular RRs and MZIs, with properties robust to fabrication variations need to be developed. The strong confinement of light in silicon photonics enables sharp bends and a small device footprint. However, this comes at the cost of a high sensitivity of device properties to fabrication variations. Since the fabrication variations are inherent to the fabrication process, these are unavoidable. Thus, robust optimization methods for minimizing the effects of fabrication variations are crucial for further developing silicon photonics. In this context, we focus on making the free spectral range of RRs and MZIs more robust to fabrication variations.

## 1.4. RESEARCH GOALS AND THESIS OUTLINE

We have set three research goals to take up the abovementioned three challenges. These are the subjects of Chapters 2, 3 and 4 of this thesis. To reach the goals, all necessary activities in the complete research chain have been undertaken. This includes photonic design, simulation, fabrication, packaging, characterization of the optical properties of the devices and ultrasound measurements of the developed photonics sensors. For photonic design, Optodesigner of Synopsys [50] is used, while for photonic simulations COMSOL is used. The silicon photonic structures have been fabricated at IMEC through the Europractice MPW service. Sensors are obtained by applying a sequence of post-processing steps, carried out in the Kavli Nanolab Delft, and by packaging steps in our lab. The InP photonic chip has been fabricated at SMART Photonics.

The outline of this thesis is as follows. In Chapter 2 an interrogator, which we call MediGator (medical interrogator), is presented to meet challenge 1. The MediGator comprises a custom light source and a PIC chip with an MZI, a  $3 \times 3$  MMI and photodetectors. Each property of the light source is specially tailored to meet the critical demands of the interrogation of the RR sensor. The full mathematical description of the interrogation is presented. It leads to the optimum MZI design. High interrogation performance is experimentally demonstrated and is compared with the modulation method. Results show that the MediGator overcomes the limitations of the modulation method.

An MZI ultrasound sensor designed to overcome the limitations of the RR sensor is demonstrated in Chapter 3. One arm of the MZI is located on a thin membrane, working as the sensing part of the device. Ultrasound waves excite the membrane's vibrational mode, thus inducing modulation of the MZI transmission. We experimentally demonstrate high sensitivity, low detection limit and large dynamic range of this sensor. Since the transmission characteristic of the MZI is gradual, the wavelength-operation range is wider than that of RRs, providing a more robust interrogation. In addition, unlike RRs, MZIs do not exhibit nonlinear effects for relatively high optical input power, which is advantageous for further improving the performance of the sensor. This chapter is concluded by an addendum on membrane buckling. In this addendum, we explore the causes of the membrane buckling and the possible influence of the buckling on the sensor's acoustic properties.

In Chapter 4 we develop a design method for silicon RRs with a free spectral range (FSR) robust to fabrication variations, in particular variations of the waveguide width of these devices. To obtain an accurate design and well-aimed robust performance, we determine the systematic waveguide-width deviation of the foundry and use it for calibrating the design inputs. Two waveguide widths are used in the RR, compensating the effect of width variations on the free spectral range. Experimental results match well with our theoretical prediction, proving that the method is valid. This design method can be applied to PICs comprising multiple RRs. An MZI with an FSR robust to fabrication variations can be obtained using a similar design method as well. In the addendum of this chapter, design and performance prediction of MZIs with a robust FSR are presented, which shows the feasibility.

In Chapter 5 we present the overall conclusions of the thesis and an outlook, which shortly discusses how to further develop our sensor and interrogator towards imaging applications.

The Appendices provide information on the photonic designs implemented in the two

silicon photonics MPW runs, the membrane fabrication process, and the sensor packaging procedure.

## REFERENCES

- [1] J.-D. Colladon, *On the reflections of a ray of light inside a parabolic liquid stream*, *Comptes Rendus* **15** (1842), pp. 800–802.
- [2] R. Nagarajan, M. Kato, J. Pleumeekers, P. Evans, S. Corzine, S. Hurtt, A. Dentai, S. Murthy, M. Missey, R. Muthiah, R. A. Salvatore, C. Joyner, R. Schneider, M. Ziari, F. Kish, and D. Welch, *InP photonic integrated circuits*, *IEEE Journal of Selected Topics in Quantum Electronics* **16** (2010), pp. 1113–1125.
- [3] T. Komljenovic, M. Davenport, J. Hulme, A. Y. Liu, C. T. Santis, A. Spott, S. Srinivasan, E. J. Stanton, C. Zhang, and J. E. Bowers, *Heterogeneous silicon photonic integrated circuits*, *Journal of Lightwave Technology* **34** (2016), pp. 20–35.
- [4] D. Guckenberger, S. Abdalla, C. Bradbury, J. Clymore, P. De Dobbelaere, D. Foltz, S. Gloeckner, M. Harrison, S. Jackson, D. Kucharski, Y. Liang, C. Lo, M. Mack, G. Masini, A. Mekis, A. Narasimha, M. Peterson, T. Pinguet, J. Redman, S. Schni, B. Welch, K. Yokoyama, and S. Yu, *Advantages of CMOS photonics for future transceiver applications*, in *36th European Conference and Exhibition on Optical Communication* (IEEE, 2010) pp. 1–6.
- [5] C. Doerr, L. Chen, D. Vermeulen, T. Nielsen, S. Azemati, S. Stulz, G. McBrien, X.-M. Xu, B. Mikkelsen, M. Givchchi, C. Rasmussen, and S.-Y. Park, *Single-chip silicon photonics 100-Gb/s coherent transceiver*, in *Optical Fiber Communication Conference* (Optical Society of America, 2014) pp. Th5C–1.
- [6] J. Verbist, J. Zhang, B. Moeneclaey, W. Soenen, J. Van Weerdenburg, R. Van Uden, C. Okonkwo, J. Bauwelinck, G. Roelkens, and X. Yin, *A 40-GBd QPSK/16-QAM integrated silicon coherent receiver*, *IEEE Photonics Technology Letters* **28** (2016), pp. 2070–2073.
- [7] G.-D. Kim, H.-S. Lee, C.-H. Park, S.-S. Lee, B. T. Lim, H. K. Bae, and W.-G. Lee, *Silicon photonic temperature sensor employing a ring resonator manufactured using a standard CMOS process*, *Optics Express* **18** (2010), pp. 22215–22221.
- [8] H. Xu, M. Hafezi, J. Fan, J. M. Taylor, G. F. Strouse, and Z. Ahmed, *Ultra-sensitive chip-based photonic temperature sensor using ring resonator structures*, *Optics Express* **22** (2014), pp. 3098–3104.
- [9] W. J. Westerveld, S. M. Leinders, P. M. Muilwijk, J. Pozo, T. C. van den Dool, M. D. Verweij, M. Yousefi, and H. P. Urbach, *Characterization of integrated optical strain sensors based on silicon waveguides*, *IEEE Journal of Selected Topics in Quantum Electronics* **20** (2013), pp. 101–110.
- [10] E. Hallynck and P. Bienstman, *Integrated optical pressure sensors in silicon-on-insulator*, *IEEE Photonics Journal* **4** (2012), pp. 443–450.
- [11] S. M. Leinders, W. J. Westerveld, J. Pozo, P. Van Neer, B. Snyder, P. O’Brien, H. P. Urbach, N. de Jong, and M. D. Verweij, *A sensitive optical micro-machined ultrasound sensor (OMUS) based on a silicon photonic ring resonator on an acoustical membrane*, *Scientific Reports* **5** (2015), p. 14328.

- [12] P. V. Lambeck, *Integrated optical sensors for the chemical domain*, Measurement Science and Technology **17** (2006), p. R93.
- [13] C. R. Pollock and M. Lipson, *Integrated photonics*, Vol. 20 (Springer, 2003).
- [14] *Lumerical*, Lumerical Inc., Vancouver, BC, Canada.
- [15] *COMSOL*, COMSOL Inc., Burlington, MA, United States.
- [16] Y. Xing, U. Khan, A. R. Alves Júnior, and W. Bogaerts, *Behavior model for directional coupler*, in *Proceedings Symposium IEEE Photonics Society Benelux* (2017) pp. 128–131.
- [17] W. Bogaerts, P. De Heyn, T. Van Vaerenbergh, K. De Vos, S. Kumar Selvaraja, T. Claes, P. Dumon, P. Bienstman, D. Van Thourhout, and R. Baets, *Silicon microring resonators*, Laser & Photonics Reviews **6** (2012), pp. 47–73.
- [18] M. BŁAHUT and D. Kasprzak, *Multimode interference structures—properties and applications*, Optica Applicata **34** (2004), pp. 573–587.
- [19] L. Z. Zehnder, *Ein neuer interferenzrefraktor*, Instrumentenkunde **11** (1981), pp. 275–285.
- [20] L. Z. Mach, *Ueber einen interferenzrefraktor*, Instrumentenkunde **12** (1982), pp. 89–94.
- [21] F. Brosinger, H. Freimuth, M. Lacher, W. Ehrfeld, E. Gedig, A. Katerkamp, F. Spener, and K. Cammann, *A label-free affinity sensor with compensation of unspecific protein interaction by a highly sensitive integrated optical Mach–Zehnder interferometer on silicon*, Sensors and Actuators B: Chemical **44** (1997), pp. 350–355.
- [22] D. Taillaert, F. Van Laere, M. Ayre, W. Bogaerts, D. Van Thourhout, P. Bienstman, and R. Baets, *Grating couplers for coupling between optical fibers and nanophotonic waveguides*, Japanese Journal of Applied Physics **45** (2006), p. 6071.
- [23] B. Snyder and P. O’Brien, *Planar fiber packaging method for silicon photonic integrated circuits*, in *Optical Fiber Communication Conference* (Optical Society of America, 2012) pp. OM2E–5.
- [24] Z. Fang and C. Z. Zhao, *Recent progress in silicon photonics: a review*, ISRN Optics **2012** (2012).
- [25] *Europractice*, <https://europractice-ic.com/>, accessed on March 10, 2020.
- [26] *SMART Photonics*, <https://smartphotonics.nl/>, accessed on March 10, 2020.
- [27] K. Nakamura, *Ultrasonic transducers: Materials and design for sensors, actuators and medical applications* (Elsevier, 2012).
- [28] K. Jansen, A. F. Van Der Steen, H. M. van Beusekom, J. W. Oosterhuis, and G. van Soest, *Intravascular photoacoustic imaging of human coronary atherosclerosis*, Optics Letters **36** (2011), pp. 597–599.



- [29] Y. Qiu, J. V. Gigliotti, M. Wallace, F. Griggio, C. E. Demore, S. Cochran, and S. Trolier-McKinstry, *Piezoelectric micromachined ultrasound transducer (PMUT) arrays for integrated sensing, actuation and imaging*, *Sensors* **15** (2015), pp. 8020–8041.
- [30] K. K. Park, O. Oralkan, and B. T. Khuri-Yakub, *A comparison between conventional and collapse-mode capacitive micromachined ultrasonic transducers in 10-MHz 1-D arrays*, *IEEE Transactions on Ultrasonics, Ferroelectrics, and Frequency Control* **60** (2013), pp. 1245–1255.
- [31] T. L. Szabo, *Diagnostic ultrasound imaging: inside out* (Academic Press, 2004).
- [32] A. Ng and J. Swanevelder, *Resolution in ultrasound imaging*, *Continuing Education in Anaesthesia Critical Care & Pain* **11** (2011), pp. 186–192.
- [33] N. Ozmen, R. Dapp, M. Zapf, H. Gemmeke, N. V. Ruitter, and K. W. van Dongen, *Comparing different ultrasound imaging methods for breast cancer detection*, *IEEE Transactions on Ultrasonics, Ferroelectrics, and Frequency Control* **62** (2015), pp. 637–646.
- [34] B.-Y. Hsieh, S.-L. Chen, T. Ling, L. J. Guo, and P.-C. Li, *All-optical scanhead for ultrasound and photoacoustic imaging—imaging mode switching by dichroic filtering*, *Photoacoustics* **2** (2014), pp. 39–46.
- [35] D. Gallego and H. Lamela, *High-sensitivity ultrasound interferometric single-mode polymer optical fiber sensors for biomedical applications*, *Optics Letters* **34** (2009), pp. 1807–1809.
- [36] H. Lamela, D. Gallego, and A. Oraevsky, *Optoacoustic imaging using fiber-optic interferometric sensors*, *Optics Letters* **34** (2009), pp. 3695–3697.
- [37] H. Grün, G. Paltauf, M. Haltmeier, and P. Burgholzer, *Photoacoustic tomography using a fiber based fabry-perot interferometer as an integrating line detector and image reconstruction by model-based time reversal method*, in *European Conference on Biomedical Optics* (Optical Society of America, 2007) p. 6631\_6.
- [38] J. A. Guggenheim, J. Li, T. J. Allen, R. J. Colchester, S. Noimark, O. Ogunlade, I. P. Parkin, I. Papakonstantinou, A. E. Desjardins, E. Z. Zhang, and P. C. Beard, *Ultrasensitive plano-concave optical microresonators for ultrasound sensing*, *Nature Photonics* **11** (2017), pp. 714–719.
- [39] S. V. Thathachary and S. Ashkenazi, *Toward a highly sensitive polymer waveguide fiber Fabry-Pérot ultrasound detector*, *Journal of Biomedical Optics* **23** (2018), p. 106008.
- [40] A. Rosenthal, D. Razansky, and V. Ntziachristos, *High-sensitivity compact ultrasonic detector based on a pi-phase-shifted fiber Bragg grating*, *Optics Letters* **36** (2011), pp. 1833–1835.
- [41] A. Rosenthal, M. Á. A. Caballero, S. Kellnberger, D. Razansky, and V. Ntziachristos, *Spatial characterization of the response of a silica optical fiber to wideband ultrasound*, *Optics Letters* **37** (2012), pp. 3174–3176.

- [42] T. Liu, L. Hu, and M. Han, *Adaptive ultrasonic sensor using a fiber ring laser with tandem fiber Bragg gratings*, *Optics Letters* **39** (2014), pp. 4462–4465.
- [43] Q. Wu and Y. Okabe, *Waveform reconstruction for an ultrasonic fiber Bragg grating sensor demodulated by an erbium fiber laser*, *Applied optics* **54** (2015), pp. 694–698.
- [44] G. A. Cranch, P. J. Nash, and C. K. Kirkendall, *Large-scale remotely interrogated arrays of fiber-optic interferometric sensors for underwater acoustic applications*, *IEEE Sensors Journal* **3** (2003), pp. 19–30.
- [45] A. Rosenthal, M. Omar, H. Estrada, S. Kellnberger, D. Razansky, and V. Ntziachristos, *Embedded ultrasound sensor in a silicon-on-insulator photonic platform*, *Applied Physics Letters* **104** (2014), p. 021116.
- [46] T. Ling, S.-L. Chen, and L. J. Guo, *High-sensitivity and wide-directivity ultrasound detection using high Q polymer microring resonators*, *Applied Physics Letters* **98** (2011), p. 204103.
- [47] C. Zhang, S.-L. Chen, T. Ling, and L. J. Guo, *Review of imprinted polymer microrings as ultrasound detectors: Design, fabrication, and characterization*, *IEEE Sensors Journal* **15** (2015), pp. 3241–3248.
- [48] F. G. Peternella, B. Ouyang, R. Horsten, M. Haverdings, P. Kat, and J. Caro, *Interrogation of a ring-resonator ultrasound sensor using a fiber Mach-Zehnder interferometer*, *Optics Express* **25** (2017), pp. 31622–31639.
- [49] G. Priem, P. Dumon, W. Bogaerts, D. Van Thourhout, G. Morthier, and R. Baets, *Optical bistability and pulsating behaviour in Silicon-On-Insulator ring resonator structures*. *Optics Express* **13** (2005), pp. 9623–9628.
- [50] *Optodesigner*; Synopsys, Inc., Mountain View, CA, United States.



# 2

## INTEGRATED PHOTONICS INTERFEROMETRIC INTERROGATOR FOR A RING-RESONATOR ULTRASOUND SENSOR

*We present a compact integrated photonics interrogator for a ring-resonator (RR) ultrasound sensor, the so-called MediGator. The MediGator consists of a special light source and an InP Mach-Zehnder interferometer (MZI) with a  $3 \times 3$  multi-mode interferometer. Miniaturization of the MZI to chip size enables high temperature stability and negligible signal drift. The light source has a  $-3$  dB bandwidth of  $1.5$  nm, a power density of  $9$  dBm/nm and a tuning range of  $5.7$  nm, providing sufficient signal level and robust alignment for the RR sensor. The mathematical procedure of interrogation is presented, leading to the optimum MZI design. We measure the frequency response of the sensor using the MediGator, giving a resonance frequency of  $0.995$  MHz. Further, high interrogation performance is demonstrated at the RR resonance frequency for an ultrasound pressure range of  $1.47 - 442.4$  Pa, which yields very good linearity between the pressure and the resulting modulation amplitude of the RR resonance wavelength. The measured signal time traces match well with calculated results. Linear fitting of the pressure data gives a sensor sensitivity of  $77.2$  fm/Pa. The MediGator provides a low detection limit, temperature robustness and a large measurement range for interrogating the RR ultrasound sensor.*

---

This chapter is based on: B. Ouyang, M. Haverdings, R. Horsten, M. Kruidhof, P. Kat, and J. Caro, *Integrated photonics interferometric interrogator for a ring-resonator ultrasound sensor*, Optics Express **27** (2019), pp. 23408-23421.

## 2.1. INTRODUCTION

Integrated photonics sensors are contributing to many fields, including chemical sensing [1–4], temperature sensing [5, 6], and ultrasound detection [7, 8]. Recently, such sensors for detecting ultrasound based on ring resonators (RRs) fabricated in silicon-on-insulator (SOI) and polymer platforms have attracted attention [9–11], in view of their high sensitivity, small footprint, possibility of realizing a sensor array on chip, immunity to electromagnetic interference and mass producibility. Therefore, high quality interrogation of this type of sensors becomes crucial for their further development and applications.

RR sensors are often interrogated using an optical spectrum analyzer (OSA), for measuring the shift of the transmission spectrum [5, 12]. However, its resolution is limited to the pm range and the interrogation speed is low, which makes an OSA unsuitable for sensing narrow and fast periodic signals. An on-chip arrayed waveguide grating was developed for interrogating a RR gas sensor [13]. The arrayed waveguide grating is suitable for high speed, but its resolution is also too low for RR ultrasound sensors. Another method is the so-called modulation method, using a narrow linewidth tunable laser and a high speed photodetector [9–11]. By placing the laser wavelength at the linear flank of a RR resonance and measuring the resulting modulation of the transmitted power, the resonance-wavelength modulation can be extracted. However, the highest modulation amplitude measurable with this method is limited by the narrow width of a resonance, implying a short flank [9]. In [14] we demonstrate an interrogator for a RR ultrasound sensor based on a fiber Mach-Zehnder interferometer (MZI) with a  $3 \times 3$  fiber coupler. Owing to the  $3 \times 3$  coupler, at least two outputs of the MZI are non-zero for any operation wavelength, enabling detecting a resonance-wavelength modulation resulting from a 1.2 Pa ultrasound pressure [14]. However, due to the large footprint of the fiber circuit, the environmental phase drift of the MZI is hard to control, thus making this fiber interrogator unsuited for long-time measurements. In addition, it requires pre-measurement at high ultrasound pressure for a circle fitting procedure with the measured signals, adding complexity in using the fiber interrogator [14].

Here, as the next step in the development started in [14], we present a compact integrated photonics interrogator, consisting of a photonic integrated circuit (PIC) and a special light source. The PIC includes an integrated photonics MZI with a  $3 \times 3$  multimode interferometer (MMI) and three photodetectors. With this miniaturization of the MZI, the temperature of the MZI can be well controlled during interrogation. Therefore, this new interrogator is very suitable for long-time measurements as well. Similar MZIs have been reported for interrogating fiber Bragg grating (FBG) sensors [15], but not for the RR sensors, which are challenging due to the multiple resonances, the limited control of the resonance wavelength, the narrow resonance linewidth and the low transmission of the fiber-to-RR coupling. We developed a novel light source to overcome these issues. The light source comprises a pump laser, an Er-doped fiber and a tunable FBG. It provides a spectrum with high power density, large tuning range and suitable bandwidth. These properties ensure a high S/N ratio of the output signals, a robust alignment of the source to the sensor, and a large measurement range. By taking into account instrumental offsets stably present in the acquired signals, we avoid the above-mentioned circle fitting and thus strongly simplify the interrogation procedure. We analytically present the interrogation procedure and experimentally demonstrate a low detection limit and a large

measurement range of this interrogator. Together with the RR sensor, this integrated interrogator is very promising for medical applications, such as intravascular ultrasound imaging [16]. Therefore, we call this interrogator MediGator (medical interrogator).

## 2.2. RING-RESONATOR ULTRASOUND SENSOR AND MEDI GATOR DESIGN

### 2.2.1. RING-RESONATOR ULTRASOUND SENSOR

Here we provide the background of the operation of the RR ultrasound sensor used in the interrogation experiments and present its main characteristics. The latter serve as input for developing the interrogation procedure and for matching of the MediGator and the RR sensor presented in Section 2.3.

The sensor is very similar to the ones we used in our previous work [14]. It comprises a racetrack-shaped silicon RR located on a silicon dioxide membrane that has its vibrational mode in the MHz range. A difference is that the present sensor has a square membrane, while the previous ones had a circular membrane. Further, the racetrack is parallel to the  $\langle 100 \rangle$  direction instead of the  $\langle 110 \rangle$  direction. This gives a somewhat smaller resonance-wavelength shift in response to the applied strain [17]. A schematic of the sensor, a cross-section of the membrane region and a microscope image of the membrane are presented in Figures 2.1(a)-(c). RRs of the type shown in Figure 2.1(c) were fabricated at IMEC through the ePIXfab MPW service [18] on a CMOS compatible SOI platform [220 nm Si layer, 2  $\mu\text{m}$  buried oxide (BOX) layer]. The two directional couplers of the RR are identical. The realized waveguide width of the RR is 400 nm. Operational ultrasound sensors result from post-processing in the Kavli Nanolab Delft and subsequent packaging, using the same procedures as described in [7]. The truncated pyramidal hole under the membrane [Figure 2.1(b)] is formed in a KOH etch, applied to locally remove the silicon substrate under the RR, using the BOX layer as etch stop. As can be seen in Figure 2.1(c), the 84  $\mu\text{m} \times 84 \mu\text{m}$  membrane is well aligned to the RR.

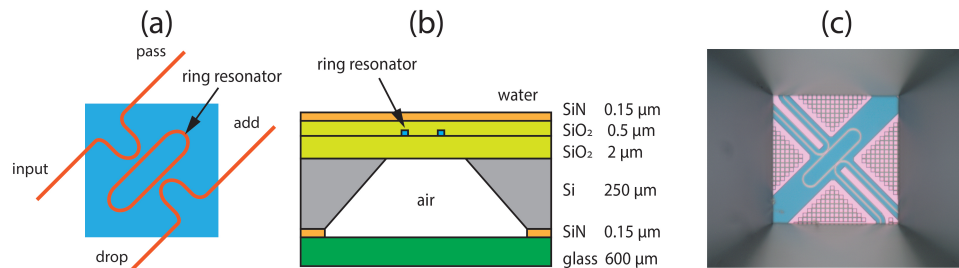


Figure 2.1: (a) Schematic of the RR ultrasound sensor: a RR on a square membrane (blue). (b) Cross-section of the membrane region, showing the various layers and their thickness. Membrane thickness is 2.65  $\mu\text{m}$ . A glass platelet seals the air cavity under the membrane. (c) Microscope image of the membrane with the RR, taken from below. Membrane size is 84  $\mu\text{m} \times 84 \mu\text{m}$ .

In the underwater sensing situation, the membrane's vibrational mode is excited by acoustic waves of proper characteristics. The membrane vibrations induce time-periodic

strain in the RR. This results in a modulation of the circumference  $L$  of the ring and the effective index  $n_e$  of the ring's waveguide [17, 19]. These quantities determine the resonance condition  $n_e(\lambda_r)L = m\lambda_r$  ( $m$  is an integer), for which the ring resonates at resonance wavelength  $\lambda_r$ . Thus, the acoustic waves induce a modulation of the resonance wavelength of a magnitude proportional to the pressure of the waves. By interrogating the sensor, the resonance-wavelength modulation can be obtained. This yields information of the incident waves that is required for acoustic imaging applications.

The RR sensor is packaged for measuring the transmission at the drop port, implying that sensing uses a resonance peak instead of a dip. This strongly simplifies the analytical description of the output interrogation signals. The transmission to the drop port of our sensor with identical directional couplers can be expressed as [20]

$$T_{\text{drop}}(\theta) = \frac{(1 - r^2) a}{1 - 2r^2 a \cos\theta + (r^2 a)^2}, \quad (2.1)$$

where  $r$  and  $a$  are the self-coupling coefficient and single round-trip amplitude transmission, respectively.  $\theta$  is the accumulated phase of the circulating mode for a single round trip in the ring. Following the same line of reasoning as in [14] for a resonance dip, it can be shown that Eq. 2.1 for wavelengths  $\lambda$  close to  $\lambda_r$ , i.e., at or close to resonance, can be approximated by

$$T_{\text{drop}}(\lambda) \approx \frac{\varepsilon}{1 + \frac{(\lambda - \lambda_r)^2}{(\gamma_r/2)^2}}. \quad (2.2)$$

Here  $\varepsilon$  and  $\gamma_r$  are defined by, respectively

$$\varepsilon = \frac{(1 - r^2)^2 a}{(1 - r^2 a)^2}, \quad (2.3)$$

$$\gamma_r = \frac{\lambda_r^2 (1 - r^2 a)}{\pi n_g L r \sqrt{a}}. \quad (2.4)$$

The line shape of the transmission peak given by Eq. 2.2 is Lorentzian.  $\varepsilon$  is the maximum transmission value.  $\gamma_r$  is the full width at half maximum (FWHM) of the transmission peak. Obtained from characterization results, our RR sensors typically have  $\gamma_r \approx 100$  pm. The free spectral range of the RRs [FSR, with  $\text{FSR} = \lambda_r^2 / (n_g L)$ ;  $n_g$  is the group index] is about 5 nm.

### 2.2.2. MEDI GATOR DESIGN

The MediGator comprises two main parts: the light source and the InP PIC. In interrogating the RR sensor, the light source is coupled to the input port of the RR, and the drop port of the RR is coupled to the input of the PIC. A schematic of the MediGator is shown in Figure 2.2.

The light source is designed to have a high power density, a proper bandwidth and a tuning range exceeding the FSR of the RR. A high power density is needed for sufficient S/N ratio of the MediGator output signals, in view of the narrow RR resonance peak and transmission losses in the system, which is mainly due to fiber-chip connections.

The light-source bandwidth should be large compared to  $\gamma_r$  and to the amplitude of the resonance-wavelength modulation resulting from acoustic waves. Further, it should be small compared to the FSR of the RR to enable selecting only a single resonance from the sensor transmission spectrum by tuning the position of the source spectrum. The requirement for the tuning range results from the limited control of the resonance wavelength due to the fabrication variations. A tuning range exceeding the FSR always allows centering the light-source spectrum at a resonance peak.

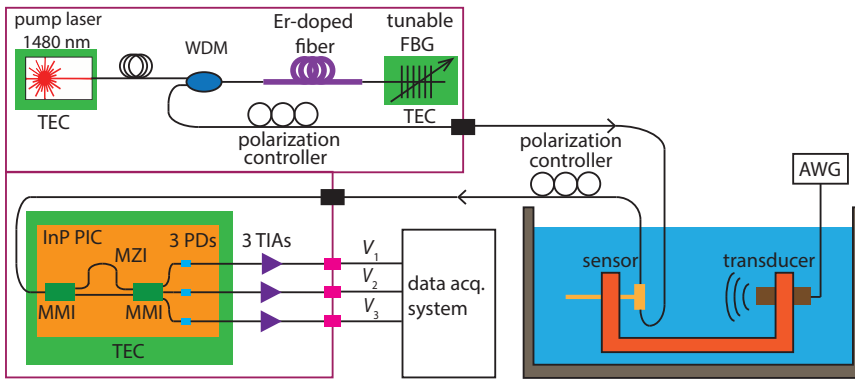


Figure 2.2: MediGator (left) and experimental setup (right). The MediGator comprises the tunable light source of high brightness (upper part) and the photonic integrated circuit of MZI and PDs (lower part). Each PD is connected to a TIA. (TEC, thermoelectric cooling; WDM, wavelength division multiplexer; FBG, fiber Bragg grating; PIC, photonic integrated circuit; PD, photodetector; TIA, trans-impedance amplifier; AWG, arbitrary waveform generator; MMI, multi-mode interferometer)

In more detail, the source has similarities with the Er-doped fiber lasers studied in [21]. Here, however, we use light amplification based on a dual-pass configuration instead of a real cavity (see Figure 2.2). The source is based on a 1480 nm Fabry-Perot pump laser (Anritsu, AF4B125EA75L) with an internal thermoelectric cooler (TEC). The pump laser is operated in continuous mode. Its light is coupled into an Er-doped fiber [Fibercore I-25 (980/125), length 3.5 m] using a wavelength division multiplexer (WDM, Thorlabs, WD1450B). The 1480 nm light excites the Er ions, which partly decay by spontaneous emission. The spontaneously emitted light in turn leads to stimulated emission by excited Er ions. Part of the fiber-guided spontaneously emitted spectrum reaches a tunable FBG (AtGrating, chirped type, 10 mm long). The FBG reflects the spectrum back into the fiber, where it induces further stimulated emission. As a result, a high brightness spectrum dominated by stimulated emission and of a bandwidth determined by the FBG reflection is coupled out from the fiber via the WDM. By stretching the FBG, the spectral position is tunable. The FBG is chosen to have a bandwidth large enough compared to  $\gamma_r$  of the transmission peak, to ensure that the peak remains within the source spectrum, even for high modulation amplitudes. After the WDM the light passes a polarization controller for setting the polarization in the optimum direction for the grating coupler of the RR, which is designed for TE polarization. For further stability of the source, the temperature of the pump laser and the FBG are also TEC regulated.



The InP PIC of the MediGator was fabricated at SMART Photonics [22]. It is designed as an MZI with a  $2 \times 2$  MMI input, a  $3 \times 3$  MMI output, and three photodetectors with a responsivity of 0.85 A/W for the light of wavelengths between 1520 and 1570 nm (see Figure 2.2). In operating the MediGator, at least two of the three outputs of the  $3 \times 3$  MMI are non-zero. This enables measuring very small phase changes when interrogating the sensor, as will become apparent in Section 2.5. Since the chip of the PIC is very small ( $4 \text{ mm} \times 4.6 \text{ mm}$ ), its temperature can be properly stabilized using a TEC, on which the PIC is mounted. Thus, environmental phase drift of the MZI, an issue for the fiber interrogator [14], is virtually absent. Each photodetector output is connected to a trans-impedance amplifier (TIA, Analog Devices, ADA4899-1) with a gain of 2.2 kV/A. Using a practical approach and assuming there is no loss, the wavelength-dependent power transmission  $T_{\text{MZI},i}$  ( $i = 1, 2, 3$ ) to the  $i^{\text{th}}$  output of the  $3 \times 3$  MMI is given by

$$T_{\text{MZI},i}(\lambda) \approx \frac{1}{3} \left[ p + q \cos \left( \frac{2\pi}{\text{FSR}} \lambda + \varphi_i + \psi_e \right) \right]. \quad (2.5)$$

In the ideal case  $p = q = 1$ , implying a fringe visibility  $q/p$  of unity as well. FSR is the free spectral range of the MZI, which is virtually constant in a limited wavelength range. The phase  $\varphi_i$ , with  $\varphi_i = 0^\circ, 120^\circ$  and  $240^\circ$  ( $i = 1, 2, 3$ ), are the phases introduced by the  $3 \times 3$  MMI.  $\psi_e$  represents the summation of the rest phase components that can be regarded as constant within a small wavelength range.

## 2.3. INTERROGATION PROCEDURE AND MATCHING OF THE MEDI-GATOR AND THE RING-RESONATOR SENSOR

### 2.3.1. INTERROGATION PROCEDURE

Using Eqs. 2.2 and 2.5 for the transmission of the RR and MZI, we calculate the MediGator outputs. For incident sinusoidal ultrasound waves of frequency  $f_0$ , the resonance-wavelength modulation is written as  $\delta \widetilde{\lambda}_r(t) = \delta_0 \sin(2\pi f_0 t)$ , where  $\delta_0$  is the resonance-wavelength modulation amplitude. We rewrite Eq. 2.2 as

$$T_{\text{drop}}(\lambda, \delta \widetilde{\lambda}_r(t)) = \frac{\varepsilon}{1 + \frac{(\lambda - \lambda_r - \delta \widetilde{\lambda}_r(t))^2}{(\gamma_r/2)^2}}. \quad (2.6)$$

Following the flow of the signals in Figure 2.2 and using the integrating property of the photodetectors, the output of the three TIAs can be written as

$$V_i(\delta \widetilde{\lambda}_r(t)) = \alpha P_{LS} R_{ph} G \int_0^\infty T_{\text{drop}}(\lambda, \delta \widetilde{\lambda}_r(t)) T_{\text{MZI},i}(\lambda) d\lambda. \quad (2.7)$$

Here  $\alpha$  represents the wavelength independent overall transmission coefficient of components other than the RR and the MZI between the light source and photodetector.  $P_{LS}$  is the power density of the light source. Because  $\gamma_r$  is more than one order smaller than the FBG bandwidth and  $\delta_0$  in practice is below 50 pm, we approximate the light-source spectrum as a constant.  $R_{ph}$  is the responsivity of the photodetector and  $G$  is the gain of the TIAs.

We calculate the integral in Eq. 2.7 by contour integration in the complex plane, using the residue theorem, to arrive at  $V_i$  given by:

$$V_i(\delta\tilde{\lambda}_r(t)) = \frac{\pi\alpha P_{LS}R_{ph}G\epsilon\gamma_r}{6} \left\{ p + qe^{-\frac{\pi\gamma_r}{FSR}} \cos \left[ \frac{2\pi}{FSR} (\lambda_r + \delta\tilde{\lambda}_r(t)) + \varphi_i + \psi_e \right] \right\}. \quad (2.8)$$

The procedure to arrive at Eq. 2.8 is similar to the one in [14], but simpler, as a result of using the drop-port transmission and the wide FBG bandwidth. The cosine in Eq. 2.8 has  $2\pi\delta_0 \sin(2\pi f_0 t)/FSR$  in its argument, leading to Bessel function expansions and harmonics of frequency  $f_0$  [23]. The final result is that the cosine equals a linear combination of an expansion in even harmonics and an expansion in odd harmonics. The prefactors of the expansions are  $\cos(2\pi\lambda_r/FSR + \varphi_i + \psi_e)$  and  $\sin(2\pi\lambda_r/FSR + \varphi_i + \psi_e)$ , respectively. In addition, a DC term is part of the expansion in even harmonics, which as a result of the above prefactor depends on  $\varphi_i$ . The DC term and the term  $p$  in Eq. 2.8 add up to the total DC signal contribution to  $V_i(\delta\tilde{\lambda}_r(t))$ .

Using the values of  $\varphi_i$ , two mutual orthogonal voltages  $V_x$  and  $V_y$  can be calculated from the  $V_i$ :

$$V_x(t) = 2V_1 - V_2 - V_3 = \frac{\pi\alpha P_{LS}R_{ph}G\epsilon\gamma_r q}{2} e^{-\frac{\pi\gamma_r}{FSR}} \cos \left[ \frac{2\pi}{FSR} (\lambda_r + \delta\tilde{\lambda}_r(t)) + \psi_e \right], \quad (2.9)$$

$$V_y(t) = \sqrt{3}(V_3 - V_2) = \frac{\pi\alpha P_{LS}R_{ph}G\epsilon\gamma_r q}{2} e^{-\frac{\pi\gamma_r}{FSR}} \sin \left[ \frac{2\pi}{FSR} (\lambda_r + \delta\tilde{\lambda}_r(t)) + \psi_e \right]. \quad (2.10)$$

The phase modulation  $\Phi(t)$  induced by the acoustic waves can be retrieved from  $V_x$  and  $V_y$  using the arctangent function:

$$\Phi(t) = \tan^{-1} \left( \frac{V_y}{V_x} \right) = \Phi_0 \sin(2\pi f_0 t) + \Delta\Phi. \quad (2.11)$$

Here  $\Phi_0 = 2\pi\delta_0/FSR$  is the phase-modulation amplitude and  $\Delta\Phi = 2\pi\lambda_r/FSR + \psi_e$  is a phase offset.

Equations 2.8-2.11 suggest the following interrogation procedure. First, for a known ultrasound pressure applied to the sensor, time traces of the signals  $V_i(t)$  are measured. Then, from these the orthogonal voltages  $V_x(t)$  and  $V_y(t)$  are constructed, leading to the phase modulation  $\Phi(t)$ . Applying fast Fourier transform (FFT) to  $\Phi(t)$  leads to  $\Phi_0 = 2\pi\delta_0/FSR$ , from which finally  $\delta_0$  is obtained.

### 2.3.2. MATCHING OF THE MEDIATOR AND THE RING-RESONATOR SENSOR

The MediGator should be sensitive enough to detect a resonance-wavelength modulation below 1 pm. Given  $\Phi_0 = 2\pi\delta_0/FSR$ , a smaller FSR of the MZI leads to a higher phase modulation, i.e., a higher sensitivity. However, due to the exponential prefactor of the cosine in Eq. 2.8, the oscillatory part of  $V_i$  strongly decreases with decreasing FSR. To answer the question of the optimum matching of the MediGator and the RR sensor or equivalently the combination of FSR and  $\gamma_r$  giving the maximum signal, we consider the FSR dependence of the sensitivity of  $V_i$  to small changes of  $\lambda_r$ , i.e., the function

$$S = \left| \frac{\partial V_i}{\partial \lambda_r} \right| = \frac{\pi\alpha P_{LS}R_{ph}G\epsilon\gamma_r q}{6} \frac{2\pi}{FSR} e^{-\frac{\pi\gamma_r}{FSR}} \left| \sin \left( \frac{2\pi}{FSR} \lambda_r + \varphi_i + \psi_e \right) \right|. \quad (2.12)$$

To find the optimum FSR, we apply the condition  $\partial S/\partial(\text{FSR}) = 0$ . In this, we treat the sine function in Eq. 2.12 as a constant. This makes sense, since considering the FSR dependence of  $|\partial V_i/\partial \lambda_r|$  [effectively done when considering  $\partial S/\partial(\text{FSR})$ ] should not be affected by a changing argument of the sine. Thus, the phase offset  $\Delta\Phi = 2\pi\lambda_r/\text{FSR} + \psi_e$  is constant or  $\lambda_r$  keeps pace with a change of FSR, such that  $\lambda_r$  remains at the same phase position of  $T_{\text{MZL},i}$ . The condition  $\partial S/\partial(\text{FSR}) = 0$  then readily leads to the matching condition  $\text{FSR} = \pi \times \gamma_r$ . For  $\gamma_r \approx 100$  pm (typical value of our RRs), this implies an optimum FSR of about 314 pm.

To gain further insight in the signals  $V_i(t)$  given by Eq. 2.8 and their FSR dependence, we performed calculations using MATLAB [24]. We first calculate time traces  $V_i(t)$ , using the input parameters  $p = q = 1$ ,  $\lambda_r = 1550$  nm,  $\gamma_r = 100$  pm,  $\delta_0 = 35$  pm,  $f_0 = 1$  MHz and  $\text{FSR} = \pi \times \gamma_r$  (optimum matching). Figure 2.3(a) shows traces  $V_i(t)$ . To obtain these  $V_i(t)$  traces, we choose  $\psi_e$  in the argument of the cosine of Eq. 2.8 such that a minimum of  $T_{\text{MZL},1}(\lambda)$  coincides with  $\lambda_r$ , or equivalently that  $\sin(2\pi\lambda_r/\text{FSR} + \varphi_1 + \psi_e) = 0$ . This is close to the real case in the interrogation experiments reported below.  $V_2$  and  $V_3$  in this situation are the strongest signals of equal strength, both for the DC and AC component. The latter component has a period of 1  $\mu\text{s}$ , corresponding to the ultrasound frequency  $f_0$ .  $V_1$  is dominated by frequency  $2f_0$ , in agreement with the Bessel function expansions of the cosine in Eq. 2.8 and the resonance coinciding with a minimum of  $T_{\text{MZL},1}(\lambda)$ .

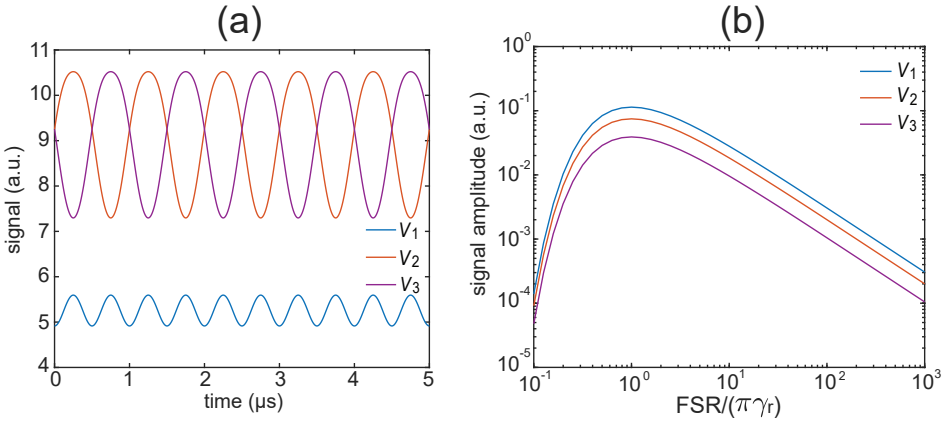


Figure 2.3: Calculated output signals of the MediGator, for the interrogation situation specified in the text. (a) Output signals  $V_i$  in the time domain. Signal  $V_1$  is dominated by the 2nd harmonic of the ultrasound frequency  $f_0$  due to the alignment of the RR resonance wavelength to a minimum of the MZI transmission at output 1. (b) Amplitude of the signals  $V_i$  as a function of the dimensionless ratio  $\text{FSR}/(\pi\gamma_r)$ . The signal amplitude cannot be directly compared with the signal magnitude in (a) in view of the much weaker modulation amplitude.

The FSR dependence of the oscillatory component of  $V_i$  is obtained from traces as in Figure 2.3(a), by calculating from these the amplitude as a function of FSR, in this case for  $\delta_0 = 1$  pm, the required detection limit. In the sweep of FSR, we again maintain a constant phase offset  $\Delta\Phi = 2\pi\lambda_r/\text{FSR} + \psi_e$ . The other parameters are kept as above. We calculate the FSR dependence for 30 random values of  $\Delta\Phi$  in the range  $[0, 2\pi]$  using MATLAB, to check whether the general behavior of the FSR dependence depends on  $\Delta\Phi$ . This turns

out to not be the case. A typical result is presented in Figure 2.3(b), for  $\Delta\Phi = 100.26^\circ$ . The maximum of the three curves occurs for  $\text{FSR}/(\pi \times \gamma_r) = 1$ , in agreement with the above analytical result for optimum matching. It follows that in practice a deviation from optimum matching should be weak in view of the strong FSR dependence of the amplitude of  $V_i$ , in particular for FSR values below the one for optimum matching.

## 2.4. CHARACTERIZATION OF THE RING-RESONATOR SENSOR, THE LIGHT SOURCE AND THE MACH-ZEHNDER INTERFEROMETER

Using the characteristics of the fabricated RR sensor, we arrived at the final design of the MZI and the light source and then fabricated these MediGator components, of which we present the characterization.

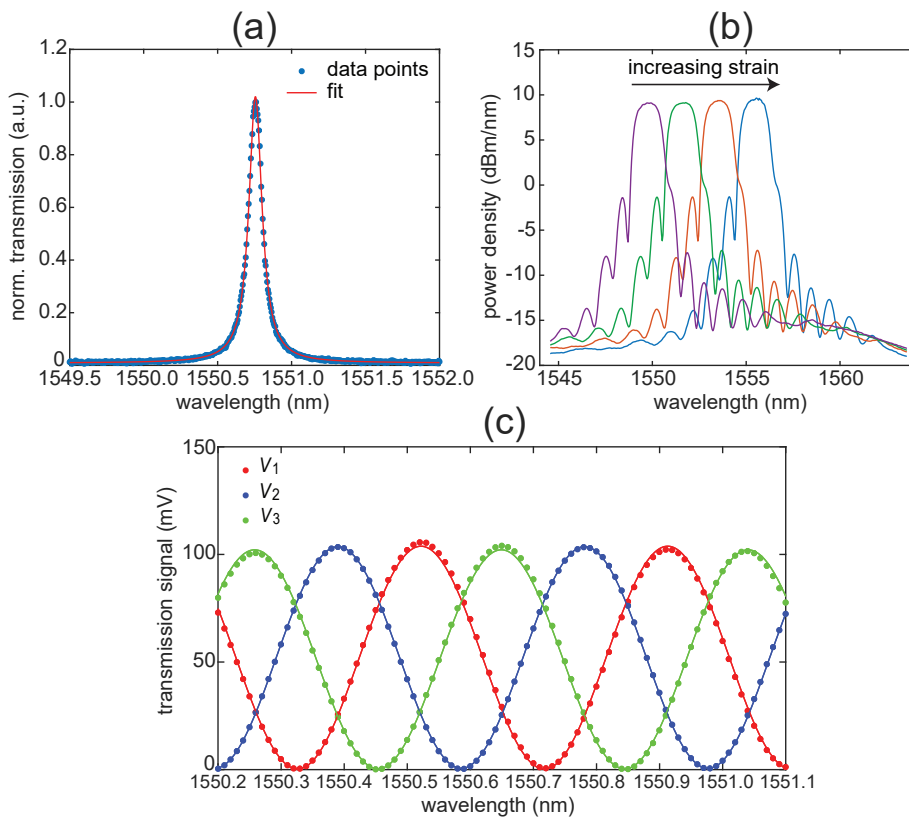


Figure 2.4: (a) Transmission peak of the RR sensor. The red curve is a fit of Eq. 2.2 to the data points. (b) Emission spectra of the MediGator light source. Straining of the FBG results in the observed red shift of the spectra, i.e., the source is tunable. The spectra have a -3 dB bandwidth of 1.5 nm and a maximum power density of 9 dBm/nm. The tuning range shown is 5.7 nm. (c) MZI transmission spectra of the three outputs  $V_i$ . The continuous curves are fits of Eq. 2.5 to the experimental data, giving  $\varphi_i = 0^\circ, 121.1^\circ$  and  $242.7^\circ$  ( $i = 1, 2, 3$ ).

The sensor is characterized from its optical transmission without applied ultrasound, by sweeping the wavelength of a tunable laser (Santec, TSL-550, output power 0.5 mW, step size 5 pm) coupled to the sensor input and by measuring the output power at the sensor drop port with a photodetector (Newport, 1811-FC-AC). Between the laser and the sensor a polarization controller (Thorlabs, FPC562) is used to set the optimum polarization for the grating coupler. In Figure 2.4(a) the resulting normalized transmission of the peak centered at 1550.755 nm is plotted (this peak is used in the interrogation experiments below), along with a fit of Eq. 2.2 to the data points. The fit describes the measured transmission very well, leading to  $\gamma_r = 108.17$  pm. The FSR of the RR sensor is 5.02 nm.

Output spectra of the light source for a drive current of the pump laser of 600 mA (interrogation conditions), measured with an OSA (Anritsu, MS9710C), are presented in Figure 2.4(b) as a function of the strain applied to the FBG. The measured spectra have a rather flat top, decay steeply and show side lobes characteristic of the FBG reflection spectrum. The power density and the spectral shape are virtually strain independent. The maximum power density is approximately 9 dBm/nm, about one order of magnitude higher than for a high end superluminescent diode emitting around 1550 nm [25]. The  $-3$  dB bandwidth of the spectra is 1.5 nm, large compared to  $\gamma_r = 108.17$  pm and to changes of resonance positions of a silicon RR due to typical environmental temperature variations occurring at a rate of about 80 pm/K [5]. This ensures robust alignment of the source spectrum to the resonance and a wide range of applicable resonance-wavelength modulations. In addition, the bandwidth is smaller than the FSR of the sensor. In Figure 2.4(b) we demonstrate a tuning range of the source spectrum of 5.7 nm. This exceeds the FSR of the sensor. The characteristics of the light source make it very suitable for actuating the sensor in the interrogation situation.

The MZI is characterized from its transmission as well, also using the tunable laser and external polarization controller to set the polarization for the PIC, which supposes TE polarization. The three output voltages  $V_i$  of the MediGator are sampled using a data acquisition system (based on National Instruments NI 5734, max. sampling rate 120 MSa/s). We find that the acquisition system has stable DC offsets and the MediGator generates constant DC voltages (offsets). These would be added to the DC components of the real signal. We calibrate the DC offsets and subtract these from the measured transmission signals. This leads to the transmission functions in Figure 2.4(c), which at first glance show an approximately  $120^\circ$  phase difference. This is confirmed by the phases  $\varphi_i = 0^\circ$ ,  $121.1^\circ$  and  $242.7^\circ$  ( $i = 1, 2, 3$ ) extracted from the fits of Eq. 2.5 to the measured transmission data, which are plotted in Figure 2.4(c) as well. The three outputs each have a fringe visibility of 0.99.

From the transmission data we find that  $\text{FSR}=391.2$  pm, to be compared with the design value  $\pi \times \gamma_r = 340$  pm. We attribute the difference to fabrication variations. The ratio  $\text{FSR}/(\pi \times \gamma_r)$  is 1.15, implying only a slight deviation from the optimum in Figure 2.3(b).

From transmission measurements of the MZI we find that its stability, judged from wavelength drift of the transmission curves, amounts to 5 pm in a one hour time period in the stable lab environment. This high stability results from temperature control with the TEC. The temperature control also yields negligible drift of the three DC signals resulting from the MZI transmission drift. These properties enable long time measurements with the MediGator.

## 2.5. EXPERIMENTS WITH THE MEDI GATOR

### 2.5.1. MEASUREMENT OF THE FREQUENCY RESPONSE OF THE SENSOR

For interrogation experiments, the frequency response of the sensor should be known. We measure the frequency response using time-delay spectrometry [26]. We use the interrogator setup of Figure 2.2, but replace the data acquisition system and arbitrary waveform generator (AWG) by a frequency spectrum analyzer (FSA, Rigol, DSA815-TG) and its tracking generator, respectively. The sensor and a transducer (Olympus, V314-SU) are coaxially mounted 240 mm apart on the opposite sides of a U-shaped frame in a water tank (see Figure 2.2), giving a normal incidence of ultrasound onto the sensor. Using the OSA we align the light-source spectrum to the resonance peak by tuning the FBG and then couple the sensor drop port to the MZI via a polarization controller.

The tracking generator drives the transducer with a sine wave that is swept in frequency and the MediGator signals  $V_i$  are sequentially measured by the FSA. The bandwidth filter of the FSA (width 3 kHz) is swept at the same rate as the drive voltage, taking into account the time delay of the acoustic waves between the transducer and the sensor. The frequency is swept from 0.5 MHz to 1.5 MHz. For each  $V_i$  we average 50 individual frequency sweeps to obtain the final results, which still include the transducer's frequency characteristic. From these we choose the result for output 3, which gives the highest signal. Among the three outputs, output 3 is closest to the maximum sensitivity according to Eq. 2.12. The maximum resonance-modulation amplitude is 2.5 pm. By using such small modulation, the second harmonic in  $V_3$  is negligible, which ensures an accurate measurement. We measure the transducer's frequency characteristic using a hydrophone (Precision Acoustics, 1 mm) and correct for it, to obtain the normalized frequency response of the sensor presented in Figure 2.5. The frequency response has its maximum at 0.995 MHz, the frequency of the membrane's lowest vibrational mode. The  $-6$  dB bandwidth, defined as the FWHM of the frequency response divided by the membrane fundamental resonance frequency, is 10.0%.

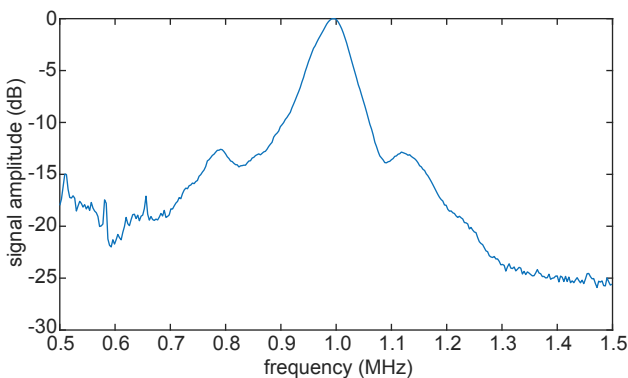


Figure 2.5: The normalized frequency response of the RR sensor, giving the resonance frequency of 0.995 MHz.

### 2.5.2. INTERROGATION EXPERIMENTS

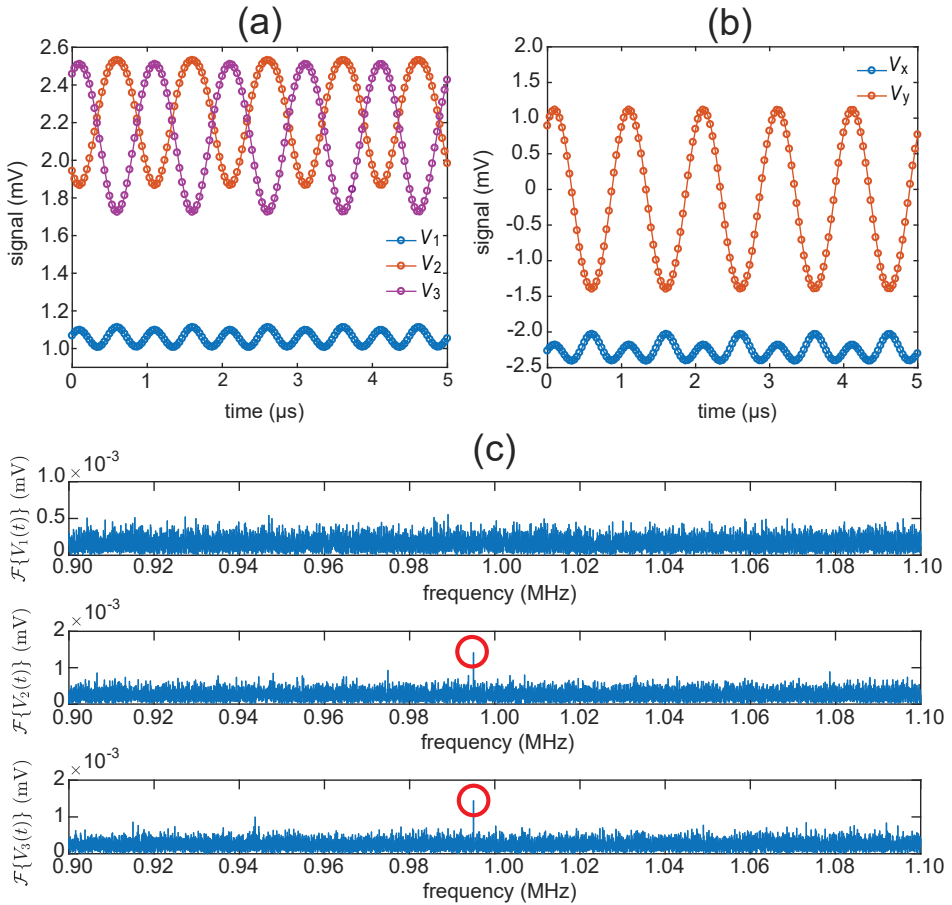


Figure 2.6: (a) Measured output signals  $V_i$  when interrogating the RR sensor. The applied pressure amplitude is 442.4 Pa. A strong 2nd harmonic is observed in  $V_1$ . (b)  $V_x$  and  $V_y$  as a function of time, calculated from  $V_i$  in (a). (c) Fourier transform of the three  $V_i$  for a pressure amplitude of 1.47 Pa. For  $V_2$  and  $V_3$ , spikes at the ultrasound frequency 0.995 MHz clearly stand out of the noise floor at this low pressure.

For the interrogation experiments, we use the complete setup in Figure 2.2. First, the pressure of acoustic waves emitted by the transducer, driven by the AWG (Rigol, DG1022), is calibrated using the hydrophone. As in the frequency response measurement, the light-source spectrum is aligned to the sensor resonance. Then, acoustic waves of frequency  $f_0 = 0.995\text{MHz}$ , the resonance frequency of the membrane, are sent to the sensor. In this situation traces  $V_i(t)$  are measured, using a sampling frequency and measurement time of 30 MHz and 50 ms, respectively. The traces are post-processed using the offset subtraction and noise reduction. For noise reduction we use Gaussian bandpass filters of 100 Hz FWHM and centered at frequency  $f_0 = 0.995\text{MHz}$  and its harmonics. Examples of time

traces  $V_i(t)$  are presented in Figure 2.6(a), for an ultrasound pressure of 442.4 Pa. The measured traces  $V_i(t)$  are close to the calculated traces in Figure 2.3(a). Compared to the case of Figure 2.3(a), the RR resonance is located slightly to the right of the minimum of  $T_{MZI,1}$ , which gives  $V_3$  a larger amplitude but a lower DC component compared to  $V_2$ . The high degree of resemblance of the measured and calculated traces indicates that the interrogator and the interrogation procedure work as predicted. From the  $V_i(t)$  we obtain  $V_x$  and  $V_y$  plotted in Figure 2.6(b). In  $V_x$  the second harmonic is also clearly visible. From  $V_x$  and  $V_y$  and using Eq. 2.11, we extract  $\delta_0 = 34.2$  pm for this pressure.

In Figure 2.6(c) the Fourier transform spectra of  $V_i(t)$  are presented for a pressure of 1.47 Pa, the lowest pressure used. Even at this pressure, signal spikes at 0.995 MHz about two times higher than the noise floor are clearly discernible in the transforms of  $V_2$  and  $V_3$ , which is enough to extract the resonance-modulation amplitude. The signal in the transform of  $V_1$  is below the noise level. The smallness of the latter signal is explained from the resonance wavelength being close to a minimum of  $T_{MZI,1}$ , as indicated before. In that case, according to Eq. 2.12 the signal amplitude of  $V_1$  is very close to zero. The  $V_i(t)$  for 1.47 Pa yield  $\delta_0 = 126$  fm. This value and the S/N ratio of about two indicate that the MediGator is capable of detecting a modulation amplitude down to 100 fm.

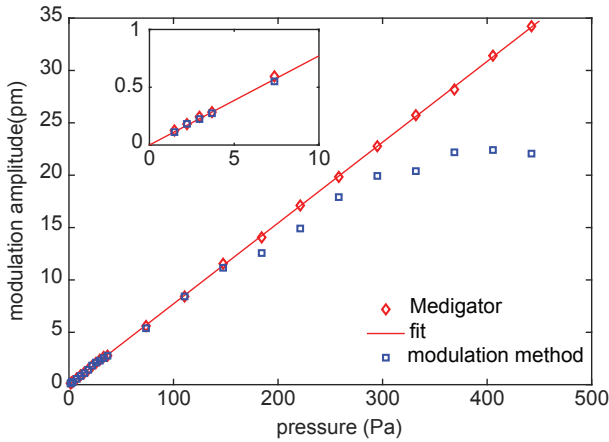


Figure 2.7: Amplitude of the resonance-wavelength modulation of the sensor as a function of the ultrasound pressure, measured with the MediGator. The inset zooms in on the low pressure range. The line is a linear fit to the MediGator data points. Its slope is the sensitivity, which amounts to 77.2 fm/Pa. For reference, results obtained with the modulation method are presented as well. The modulation method only agrees with the MediGator approach below 150 Pa. Above this value the modulation method increasingly underestimates the resonance-wavelength modulation.

Finally, we determine the sensitivity of the sensor, defined as  $\partial\delta_0/\partial P$ , where  $P$  is the pressure of the incident ultrasound. The sensitivity is obtained by interrogating the sensor for 24 pressures in the range 1.47 – 442.4 Pa and determining the related  $\delta_0$  values. The results are plotted in Figure 2.7, along with a linear fit to the data points. The plot shows excellent linearity of the relation between the pressure and the modulation amplitude across the whole pressure range. The slope of the fitted line is 77.2 fm/Pa, which is the sensi-



tivity. For comparison, we also determine the sensitivity using the modulation method explained in Section 2.1, for which the results are shown in Figure 2.7 as well. Very good agreement of the two methods is found for pressures below 150 Pa, leading to the same sensitivity value for both methods. Above 150 Pa, however, the modulation-method points lie increasingly below the MediGator points. This limitation of the modulation method arises from the short linear flank of the transmission peak. We emphasize that the MediGator does not have this limitation, leading to high quality interrogation up to the highest pressure used here, which is not limited by the MediGator itself.

## 2.6. CONCLUSION AND OUTLOOK

We designed, fabricated and demonstrated an integrated photonics interrogator, called MediGator, for interrogating a ring-resonator (RR) ultrasound sensor. The MediGator comprises i) a novel light source with proper bandwidth around 1550 nm, high power density and large tuning range and ii) an InP Mach-Zehnder interferometer (MZI) with a free spectral range matched to the sensor characteristic. Using its tunable FBG, the light-source spectrum can always be aligned to a single resonance peak of the RR spectrum, the feature for ultrasound sensing. The sensor in the present interrogation demonstration has a  $84\mu\text{m} \times 84\mu\text{m}$  square membrane, on which the RR is located, and works in the MHz range. Our mathematical description of the signal flow in the MediGator and sensor, apart from yielding matching of the MediGator to the sensor for maximum MZI outputs, leads to the interrogation procedure applied in the experiments. Thanks to the small size of the integrated photonics MZI with the  $3 \times 3$  MMI output and photodetectors, its temperature can be accurately regulated during long-time measurements for avoiding environmental phase drift, an issue of our previous fiber MZI based interrogator.

Using the MediGator, we obtain the sensor's acoustic frequency response, giving a resonance frequency of 0.995 MHz and a  $-6$  dB bandwidth of 10.0%. Interrogation experiments show high MediGator performance, reflected in ease of aligning the light source to the RR resonance and high linearity of the plot of applied acoustic pressure versus resonance-wavelength modulation. This results in a sensitivity of 77.2 fm/Pa of the sensor. The minimum ultrasound pressure detected is 1.47 Pa, resulting after FFT of the measured signals. Compared to the modulation method, the MediGator exhibits a two times larger measurement range, which in the experiments is limited by the highest applied pressure and not by the MediGator itself. In spite of one MediGator output signal accidentally being rather close to zero as a result of the wavelength position of resonance peak, the MediGator operates very well, underlining the strength of using a  $3 \times 3$  MMI at the MZI output. Summarizing, the primary merits of the MediGator are ease of operation, temperature robustness, low detection limit, large measurement range, compactness and cost effective, making the instrument very suitable for interrogating the RR ultrasound sensor.

Further improving the S/N ratio and enabling even lower detection limit are possible through several methods: improving the fiber-chip coupling, adding second-stage amplifiers after the TIAs, and further shielding of the MediGator for noise from the environment. We envision that real-time interrogation of the RR ultrasound sensor can be realized by implementing real-time signal filtering and processing to obtain the resonance-wavelength modulation. In addition, the architecture of the MZI chip can be adapted for interrogating an array of RR sensors by adding arrayed waveguide gratings or cascaded

MZIs for multiplexing and demultiplexing [27, 28]. Finally, we note that owing to the temperature stabilization of the crucial parts of the MediGator, it can also interrogate RR sensors (not limited silicon ones) for sensing of signals slower than induced by ultrasound waves. This makes the MediGator highly versatile.

## REFERENCES

- [1] N. A. Yebo, P. Lommens, Z. Hens, and R. Baets, *An integrated optic ethanol vapor sensor based on a silicon-on-insulator microring resonator coated with a porous ZnO film*, *Optics Express* **18** (2010), pp. 11859–11866.
- [2] M. Boerkamp, T. van Leest, J. Heldens, A. Leinse, M. Hoekman, R. Heideman, and J. Caro, *On-chip optical trapping and Raman spectroscopy using a TripleX dual-waveguide trap*, *Optics Express* **22** (2014), pp. 30528–30537.
- [3] K. De Vos, I. Bartolozzi, E. Schacht, P. Bienstman, and R. Baets, *Silicon-on-insulator microring resonator for sensitive and label-free biosensing*, *Optics Express* **15** (2007), pp. 7610–7615.
- [4] P. V. Lambeck, *Integrated optical sensors for the chemical domain*, *Measurement Science and Technology* **17** (2006), pp. R93–R116.
- [5] G.-D. Kim, H.-S. Lee, C.-H. Park, S.-S. Lee, B. T. Lim, H. K. Bae, and W.-G. Lee, *Silicon photonic temperature sensor employing a ring resonator manufactured using a standard CMOS process*, *Optics Express* **18** (2010), pp. 22215–22221.
- [6] H. Xu, M. Hafezi, J. Fan, J. M. Taylor, G. F. Strouse, and Z. Ahmed, *Ultra-sensitive chip-based photonic temperature sensor using ring resonator structures*, *Optics Express* **22** (2014), pp. 3098–3104.
- [7] B. Ouyang, Y. Li, M. Kruidhof, R. Horsten, K. W. van Dongen, and J. Caro, *On-chip silicon Mach-Zehnder interferometer sensor for ultrasound detection*, *Optics Letters* **44** (2019), pp. 1928–1931.
- [8] A. Rosenthal, M. Omar, H. Estrada, S. Kellnberger, D. Razansky, and V. Ntziachristos, *Embedded ultrasound sensor in a silicon-on-insulator photonic platform*, *Applied Physics Letters* **104** (2014), p. 021116.
- [9] S. Leinders, W. Westerveld, J. Pozo, P. Van Neer, B. Snyder, P. O'Brien, H. Urbach, N. De Jong, and M. Verweij, *A sensitive optical micro-machined ultrasound sensor (OMUS) based on a silicon photonic ring resonator on an acoustical membrane*, *Scientific Reports* **5** (2015), p. 14328.
- [10] A. Maxwell, S.-W. Huang, T. Ling, J.-S. Kim, S. Ashkenazi, and L. J. Guo, *Polymer microring resonators for high-frequency ultrasound detection and imaging*, *IEEE Journal of Selected Topics in Quantum Electronics* **14** (2008), pp. 191–197.
- [11] C. Zhang, S.-L. Chen, T. Ling, and L. J. Guo, *Review of imprinted polymer microrings as ultrasound detectors: Design, fabrication, and characterization*, *IEEE Sensors Journal* **15** (2015), pp. 3241–3248.
- [12] T. Claes, J. G. Molera, K. De Vos, E. Schacht, R. Baets, and P. Bienstman, *Label-free biosensing with a slot-waveguide-based ring resonator in silicon on insulator*, *IEEE Photonics Journal* **1** (2009), pp. 197–204.

- [13] N. A. Yebo, W. Bogaerts, Z. Hens, and R. Baets, *On-chip arrayed waveguide grating interrogated silicon-on-insulator microring resonator-based gas sensor*, IEEE Photonics Technology Letters **23** (2011), pp. 1505–1507.
- [14] F. G. Peternella, B. Ouyang, R. Horsten, M. Haverdings, P. Kat, and J. Caro, *Interrogation of a ring-resonator ultrasound sensor using a fiber Mach-Zehnder interferometer*, Optics Express **25** (2017), pp. 31622–31639.
- [15] Y. E. Marin, T. Nannipieri, C. J. Oton, and F. Di Pasquale, *Current status and future trends of photonic-integrated FBG interrogators*, Journal of Lightwave Technology **36** (2018), pp. 946–953.
- [16] K. Jansen, A. F. W. van der Steen, H. M. M. van Beusekom, J. W. Oosterhuis, and G. van Soest, *Intravascular photoacoustic imaging of human coronary atherosclerosis*, Optics Letters **36** (2011), pp. 597–599.
- [17] W. J. Westerveld, S. M. Leinders, P. M. Muilwijk, J. Pozo, T. C. van den Dool, M. D. Verweij, M. Yousefi, and H. P. Urbach, *Characterization of integrated optical strain sensors based on silicon waveguides*, IEEE Journal of Selected Topics in Quantum Electronics **20** (2013), pp. 101–110.
- [18] *ePIXfab*, <http://epixfab.eu/>, accessed on July 15, 2019.
- [19] C. Castellan, A. Chalyan, M. Mancinelli, P. Guilleme, M. Borghi, F. Bosia, N. M. Pugno, M. Bernard, M. Ghulinyan, G. Pucker, and L. Pavesi, *Tuning the strain-induced resonance shift in silicon racetrack resonators by their orientation*, Optics Express **26** (2018), pp. 4204–4218.
- [20] W. Bogaerts, P. De Heyn, T. Van Vaerenbergh, K. De Vos, S. Kumar Selvaraja, T. Claes, P. Dumon, P. Bienstman, D. Van Thourhout, and R. Baets, *Silicon microring resonators*, Laser & Photonics Reviews **6** (2012), pp. 47–73.
- [21] A. Escuer, S. Jarabo, and J. Álvarez, *Experimental validation of the improved analytical model for erbium-doped fibre lasers based on the energy conservation principle*, Applied Physics B **81** (2005), pp. 831–840.
- [22] *SMART Photonics*, <https://smartphotonics.nl/>, accessed on July 15, 2019.
- [23] F. W. J. Olver, *Bessel functions of integer order*, in *Handbook of Mathematical Functions with Formulas, Graphs and Mathematical Tables*, M. Abramowitz and I. A. Stegun, eds. (Dover books on Mathematics, 1964).
- [24] *MATLAB R2017a*, The MathWorks, Inc., Natick, Massachusetts, United States.
- [25] *SLED Modules*, <http://www.exalos.com/sled-modules/>, accessed on May 20, 2019.
- [26] R. A. Smith and D. R. Bacon, *A multiple-frequency hydrophone calibration technique*, Journal of the Acoustical Society of America **87** (1990), pp. 2231–2243.

- [27] M. K. Smit and C. Van Dam, *PHASAR-based WDM-devices: Principles, design and applications*, IEEE Journal of Selected Topics in Quantum Electronics **2** (1996), pp. 236–250.
- [28] F. Horst, W. M. Green, S. Assefa, S. M. Shank, Y. A. Vlasov, and B. J. Offrein, *Cascaded Mach-Zehnder wavelength filters in silicon photonics for low loss and flat pass-band WDM (de-) multiplexing*, Optics Express **21** (2013), pp. 11652–11658.

# 3

## ON-CHIP SILICON MACH-ZEHNDER INTERFEROMETER SENSOR FOR ULTRASOUND DETECTION

*A highly sensitive ultrasound sensor based on an integrated photonics Mach–Zehnder interferometer (MZI) fabricated in silicon-on-insulator technology is reported. The sensing spiral is located on a membrane of size  $121\ \mu\text{m} \times 121\ \mu\text{m}$ . Ultrasound waves excite the membrane's vibrational mode, which translates to modulation of the MZI transmission. The measured sensor transfer function is centered at 0.47 MHz and has a  $-6\ \text{dB}$  bandwidth of 21.2%. The sensor sensitivity is linear in the optical input power and reaches a maximum 0.62 mV/Pa, which is limited by the interrogation method. At 0.47 MHz and for an optical power of 1.0 mW the detection limit is  $0.38\ \text{mPa}/\text{Hz}^{1/2}$  and the dynamic range is 59 dB. The MZI's gradual transmission function allows a wide range of wavelength operation points. This strongly facilitates sensor use and is promising for applications.*

---

This chapter is based on: B. Ouyang, Y. Li, M. Kruidhof, R. Horsten, K. W. A. van Dongen, and J. Caro, *On-chip silicon Mach-Zehnder interferometer sensor for ultrasound detection*, Optics Letters **44** (2019), pp. 1928-1931.

### 3.1. INTRODUCTION

Integrated photonics, an enabling technology for many application fields, has widely pervaded photonic sensing [1, 2], with applications in environmental, chemical, and biomedical sensing. Important advantages of integrated photonics sensors are their small size, mass producibility, low cost, and electromagnetic immunity. Ring resonators (RRs) and Mach-Zehnder interferometers (MZIs) are very sensitive sensors in various contexts [1, 2] and have a simple waveguide architecture. The sensor signal of these devices results from a refractive index change of the waveguide section responding to the agent to be sensed. For RR sensors, the signal is a shift of the well-separated and sharp resonance peaks, while for the MZIs it is a shift of the continuous sinusoidal transmission spectrum. The MZI goes back to the pioneering work of Zehnder [3] and Mach [4] on free space optics interferometers, that can be used for sensing of macroscopic samples. Integrated photonics versions of MZIs have also been realized in photonic crystals, using self-collimation of light [5], where the ratio of the two MZI outputs is the sensing signal.

Recently, RRs made in polymer and silicon-on-insulator (SOI) platforms have been used to sense ultrasound [6–9]. For the polymer RRs, located on a rigid substrate, the optoelastic effect leads to ultrasound induced resonance-wavelength modulation. In [6] a polymer RR sensor is demonstrated for ultrasound in the range 1 – 75 MHz, giving a lowest measurable pressure (noise equivalent pressure, NEP) of 21.4 Pa. Polymers with a higher refractive index are suggested for bending radii below 20  $\mu\text{m}$ . In [7] an all-optical photoacoustic imaging is presented using a polymer RR sensor. The RR sensor in SOI [8, 9] developed at our department is located on a membrane sensitive to ultrasound waves, such that periodic membrane deflection at the ultrasound frequency leads to the sensor signal via transduction to the RR. This sensor has a high sensitivity owing to a high quality factor and a NEP as small as 0.4 Pa. Interrogating the sensor requires some care in view of the limited predictability of the quality factor and the resonance wavelengths due to inherent variability of the fabrication and nonlinear effects already occurring at moderate optical power, leading to bistability of the resonances [10].

An MZI sensor for static gas pressures, also based on the membrane principle, is reported in [11]. An MZI optical microphone is demonstrated in [12] for acoustic waves in air up to 20 kHz, i.e., limited to frequencies of human hearing. For waveguides fabricated in SOI, on a rigid substrate and inserted in the arms of a fiber-based MZI, the effect of polarization and waveguide dimensions on the sensitivity of ultrasound detection is analyzed in [13].

Here, we present a robust on-chip MZI sensor for ultrasound, fabricated in CMOS compatible SOI technology. The sensing spiral of the MZI is located on a square  $\text{SiO}_2$  membrane, designed to mechanically resonate at MHz frequencies in water. With our MZI sensor we achieve considerable extension of the frequency-operation range compared to the ranges in [11, 12], in particular reaching frequencies for ultrasound imaging. An MZI does not exhibit nonlinear effects up to relatively high optical power, which is helpful for the sensitivity. As for interrogating the sensor, it is very advantageous that its transmission characteristic is gradual, instead of sharp as it is for a RR. This allows a wide wavelength-operation range, facilitating sensor use and making it robust.

### 3.2. SENSOR DESIGN AND FABRICATION

Figure 3.1(a) shows a schematic of the MZI sensor. Laser light of telecom wavelengths is guided towards two spiral-shaped waveguide arms of different length via a 50:50 multimode interferometer (MMI), using an input grating coupler (GC). The light leaving the arms is combined in a  $2 \times 2$  MMI and coupled out by two other GCs. The sensing arm is located on a square membrane, acting as a mechanical resonator with a resonance frequency in the MHz range. The reference arm is on the intact substrate.

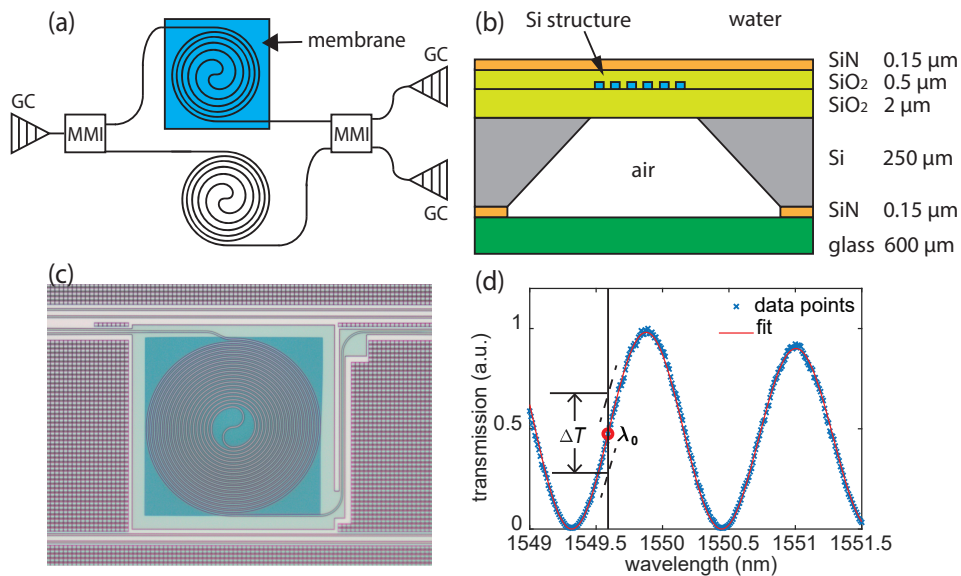


Figure 3.1: (a) Schematic of the MZI ultrasound sensor. (b) Cross section of the membrane region. A glass platelet seals the air cavity under the membrane. (c) Microscope image of the sensing region, showing the spiral on the membrane. Membrane diameter is  $121 \mu\text{m} \times 121 \mu\text{m}$ . The dense non-photonic structures outside the membrane are the so-called tiling. (d) Normalized transmission spectrum of the MZI sensor. The transmission includes the effect of the grating coupler, which explains the decreasing amplitude with increasing wavelength. At operation wavelength  $\lambda_0$  the peak-to-peak transmission modulation  $\Delta T$  resulting from an ultrasound pulse is indicated.

MZIs as in Figure 3.1(a) were fabricated at IMEC through the Europractice MPW service on a CMOS compatible SOI platform [220 nm Si layer, 2 μm buried oxide (BOX)]. The waveguides of the MZI arms are 450 nm wide. Sensors result after post-processing steps. The first step is thinning down the wafer to 250 μm. After dicing, a 0.5 μm thick SiO<sub>2</sub> layer is deposited as waveguide cladding by plasma-enhanced chemical vapor deposition on the chip level. Then, by low pressure chemical vapor deposition on both chip sides a 0.15 μm thick Si<sub>3</sub>N<sub>4</sub> layer is deposited, to act as mask in the etch to follow. On the backside, a square centered at the sensing spirals is opened in the Si<sub>3</sub>N<sub>4</sub> layer, using optical lithography and reactive ion etching in a fluorine based plasma. Then, a membrane of total thickness of 2.65 μm is created under the spiral by locally removing the Si substrate in a KOH etch, using the BOX layer as etch stop. This crystallographic etch yields the typical truncated pyramidal hole shown in Figure 3.1(b). The size of the square opened in the Si<sub>3</sub>N<sub>4</sub> mask



gives accurate control of the membrane size, which in the present case is  $121 \mu\text{m} \times 121 \mu\text{m}$ . In packaging, the chip is glued on a glass platelet. Thus, in water the membrane is water loaded on one side and air loaded on the other side. To couple light into and out of the chip in water, fibers with a reflective coating on a polished angled facet are glued on the input and output GCs using UV curable glue. A schematic cross section of the membrane region and a microscope image of the sensor are presented in Figure 3.1(b) and 3.1(c), respectively. As can be seen in Figure 3.1(c), the membrane is accurately aligned to the spiral. The membrane size is controlled to just cover the spiral. The length of the spiral is 4.5 mm, making the MZI very sensitive for sensing ultrasound waves.

The operation of the MZI sensor is of optomechanical nature. Ultrasound waves of proper characteristics incident on the membrane excite its vibrational mode, giving time-periodic strain of the spiral waveguide according to the profile and amplitude of the mode. This leads to modulation of the spiral length and, due to the optoelastic effect, of the effective index of the spiral waveguide. These, in turn, translate to phase modulation of the guided mode arriving at the combiner MMI and thus to a modulation of the MZI output power at constant operation wavelength  $\lambda_0$ . The amplitude of the phase modulation of the arriving mode is

$$\Delta\varphi(\lambda_0, L_s, L_s^*) = \frac{2\pi}{\lambda_0} \left( \int_{L_s^*} n_e^*(\lambda_0, l) dl - \int_{L_s} n_e(\lambda_0, l) dl \right), \quad (3.1)$$

where  $n_e(n_e^*)$  and  $L_s(L_s^*)$  are the effective index and length of the spiral on the strainless (maximally strained) membrane.

The MZI sensor is first characterized from its optical transmission without applied ultrasound, by sweeping the wavelength of a tunable laser (Santec, TSL-210, step size 10 pm) coupled to its input and by measuring the output power with a photodetector (Newport, 1811-FC-AC). A resulting spectrum is shown in Figure 3.1(d), normalized to its maximum. The spectrum properly shows the expected oscillations, while the smaller amplitude at 1551 nm results from the GC transmission. We fit the following function to the normalized measured transmission

$$T(\lambda) = (a\lambda + b) \left[ \frac{1}{2} \cos \left( 2\pi \frac{\lambda}{\text{FSR}} + \Phi(t) \right) + \frac{1}{2} \right], \quad (3.2)$$

where the factor in square brackets is the MZI transmission and  $(a\lambda + b)$  is the first order approximation of the GC transmission in the relevant range.  $\lambda$  is the wavelength and FSR is the MZI free spectral range. The time dependence of the phase  $\Phi(t)$  applies when ultrasound waves induce a modulation term, as a result of the phase modulation related to Eq. 3.1. The fit, also shown in Figure 3.1(d), gives  $\text{FSR} = 1.13 \text{ nm}$ , corresponding to an OPD of 2.13 mm.

### 3.3. CHARACTERIZATION OF THE ACOUSTIC PROPERTIES OF THE SENSOR

#### 3.3.1. TRANSFER FUNCTION

The sensing properties of the sensor are determined with the setup shown in Figure 3.2(a). The sensor and a piezo-transducer (Olympus, V318-SU) are coaxially mounted 230 mm

apart on the opposite sides of a U-shaped frame, which is submerged in a water tank. The ultrasound waves impinge perpendicularly upon the membrane. An arbitrary waveform generator (Agilent, 33521A) applies Gaussian modulated sinusoidal voltage pulses to the transducer to obtain acoustic pressure pulses in the time domain given by

$$p(t) = p_0 \exp \left[ - \left( \frac{t - \tau_d}{N / (2f_0)} \right)^2 \right] \sin(2\pi f_0 t). \quad (3.3)$$

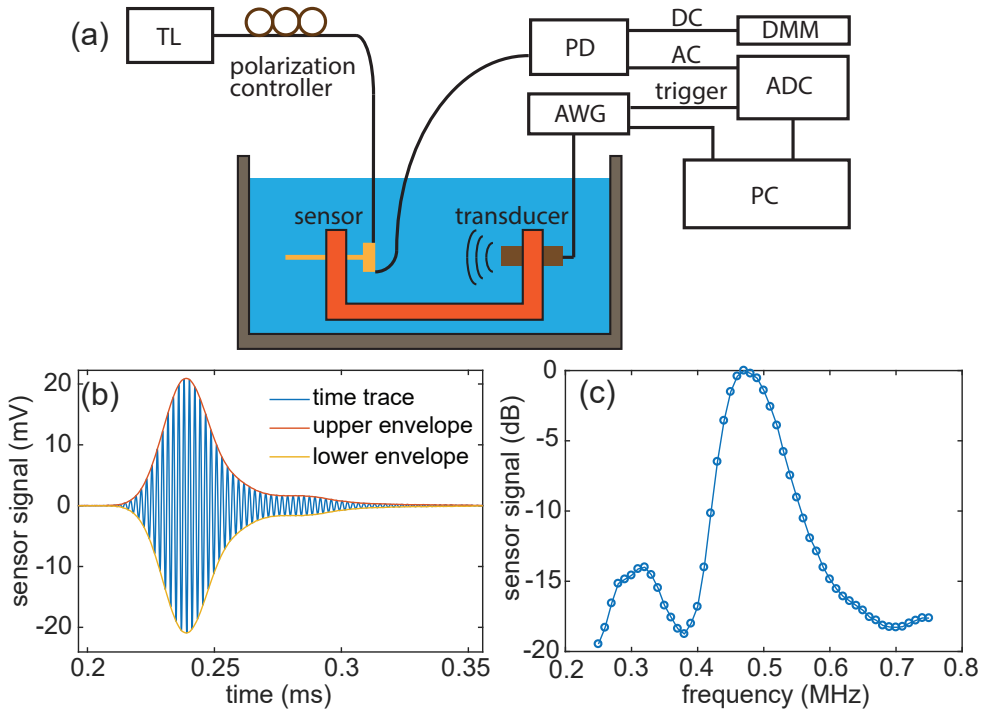


Figure 3.2: (a) Schematic of the experimental setup for characterizing the MZI sensor (TL, tunable laser; PD, photodetector; AWG, arbitrary waveform generator; DMM, digital multimeter; ADC, analog-to-digital converter). (b) Time response of the sensor to a Gaussian ultrasound pulse centered at 0.47 MHz, for a maximum sensitivity operation wavelength discussed in the text related to Eq. 3.4. (c) Normalized transfer function of the sensor, obtained with an input power of 1.0 mW.

Here  $p_0$ ,  $\tau_d$  and  $f_0$  are the pressure amplitude, delay time, and center frequency of the pulse, respectively, and  $N$  is about half the number of cycles in the envelope.  $N$  determines the frequency bandwidth of the pulse. We choose  $N = 10$ , to have a narrow bandwidth pulse. The sensor is actuated by the tunable laser set at an operation wavelength and a constant power, also aligning the polarization with a polarization controller (Thorlabs, FPC562) for maximum GC transmission. The average optical power transmitted by the MZI is monitored at the DC output of the photodetector to keep track of effects due to environmental temperature drift. The resulting wavelength drift of transmission curves

as in Figure 3.1(d) is found within  $\approx 10$  pm in the experiments reported below. The photodetector's AC output, representing the sensor response to incident acoustic pulses, is recorded by a 14-bit analog-to-digital converter (ADC, Spectrum, M3i4142-exp).

A typical time response of the sensor to a pulse given by Eq. 3.3 is shown in Figure 3.2(b), for  $p_0 = 32.2$  Pa, an input power of 1.0 mW and  $f_0 = 0.47$  MHz (the membrane's resonance frequency; see below). The response closely mimics the Gaussian excitation pulse, with the addition of a tail, due to ringing down of the resonance.

To obtain the sensor transfer function, i.e., the sensor signal as a function of frequency  $f$  at constant amplitude  $p_0$ , time responses as in Figure 3.2(b) are measured by sweeping  $f_0$  from 0.25 to 0.75 MHz with 0.01 MHz step size. At each frequency the actual response is obtained as an average of 500 individual responses. The maximum of the signal envelop [see Figure 3.2(b)], calculated from the Hilbert transform of the response, is taken as the sensor signal. We correct for the transducer's frequency characteristic, measured using a hydrophone (Precision Acoustics, 1 mm). In Figure 3.2(c) we present the resulting normalized transfer function, which shows two resonance line shapes. The dominant resonance has its maximum at 0.47 MHz and corresponds to the membrane's lowest vibrational mode. We speculate that the much weaker sub-resonance at 0.32 MHz arises from a mode related to perturbation of the bare membrane by the dense spiral.

3

### 3.3.2. SENSITIVITY

The sensitivity of the sensor at the transfer-function maximum of 0.47 MHz is the next function to determine. We define the wavelength dependent sensitivity as

$$S(\lambda) = \alpha I_{\text{in}} \left| \frac{dT}{dp} \right| = \alpha I_{\text{in}} \left| \frac{dT}{d\lambda} \frac{d\lambda}{dp} \right| \approx \alpha I_{\text{in}} \left| \frac{dT}{d\varphi} \frac{d\varphi}{dp} \right|, \quad (3.4)$$

where  $\alpha$  represents the overall loss and gain,  $I_{\text{in}}$  is the optical input power, and  $p$  is the incident ultrasound pressure.  $\Delta\varphi$  is given by Eq. 3.1.  $\Delta p$  is the change with respect to zero pressure and, thus, equals  $p$ . For small  $p$ , the response is expected linear, and both  $d\lambda/dp$  and  $d\varphi/\Delta p$  are constant. Thus, at contact pressure the sensitivity is proportional to  $I_{\text{in}}$  and to  $|dT/d\lambda|$ . The time response in Figure 3.2(b) is for operational wavelength  $\lambda_0 = 1549.59$  nm [indicated in Figure 3.1(d)], where  $|dT/d\lambda|$  and, thus, the sensitivity are maximum.

The sensitivity is obtained by first measuring the time response for 33 pressure amplitudes of the Gaussian pulse in the range 0.77–341 Pa (maximum pressure 341 Pa limited by voltage range of ADC card, not by the sensor itself; amplitudes calibrated with the hydrophone) and this for 6 optical powers up to 1.0 mW actuating the sensor. The sensor's averaged time response is bandpass filtered (0.1–1.1 MHz, Tukey window) for noise reduction outside the range of interest. The results, presented in Figure 3.3(a), along with fitted straight lines, clearly show linear behavior of the signal amplitude (i.e., maximum of envelope of time response) versus pressure down to the lowest pressure. This confirms that we indeed are working in the linear response regime. A high degree of linearity is also seen in the plot of the sensitivity versus optical input power in Figure 3.3(b), where according to Eq. 3.4 plotted sensitivity values equal the slopes of the lines in Figure 3.3(a). The sensitivity ranges from 0.31 to 0.62 mV/Pa. As a result of these high values, we can measure acoustic pressures down to 0.77 Pa with a high resolution.

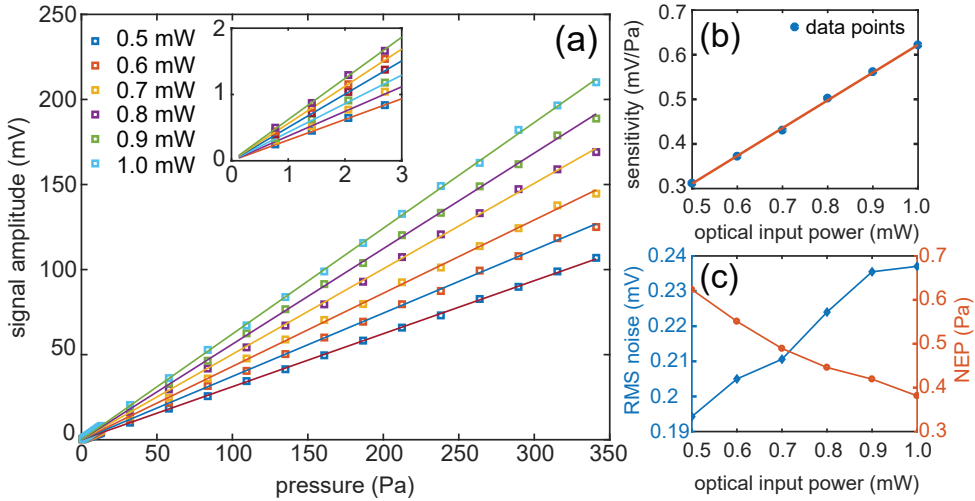


Figure 3.3: (a) Sensor–signal amplitude as a function of the amplitude of the acoustic pressure pulse, for different optical input powers. The lines are linear fits to the data points. Inset: zoom-in of the low pressure range. (b) Sensor sensitivity as a function of optical input power. Again, the line is a linear fit. (c) Root-mean-square noise (blue) and noise equivalent pressure (red) as a function of optical input power.

The lowest measurable acoustic pressure or NEP, is obtained as the root-mean-square (RMS) noise divided by the sensitivity. To obtain the dependence of the NEP on optical power, we record time traces of the photodetector output for 0.5 ms after each data set of Figure 3.3(a) for a specific power, without applying ultrasound and averaging, but with using the bandpass filter. 0.5 ms is the same measuring period as used for a single time response contributing to data points in Figure 3.3(a). Thus, noise traces are taken under the conditions of the acoustic measurements. As shown in Figure 3.3(c), the RMS noise increases from 0.194 to 0.237 mV in the range of applied powers. This behavior mainly results from increasing amplification of the intrinsic sensor noise with increasing power. The noise increase is weaker than the sensitivity increase, causing a notable NEP decrease with increasing power [see Figure 3.3(c)]. For an input power of 1.0 mW, the NEP is 0.38 Pa, corresponding to a detection limit of  $0.38 \text{ mPa/Hz}^{1/2}$ .

As a final experiment, we test the prediction of the wavelength dependence of the sensitivity in Eq. 3.4. We follow the same procedure as used for acquiring the sensitivities in Figure 3.3(b). Operation wavelengths are in the range 1549.30 – 1550.68 nm, with a 0.06 nm increment, thus covering one FSR of the MZI transmission. The optical input power is 1.0 mW. The results are plotted in Figure 3.4 as normalized sensitivity, along with the absolute value of the derivative of the fitted transmission curve in Figure 3.1(d). Excellent agreement of experiment and prediction is observed. The sensor is robust with respect to possible wavelength misalignment to a maximum sensitivity point, as this can be compensated by simply increasing the optical power without inducing nonlinear effects (see below). The wide FWHM of the sensitivity branches ( $\approx 400 \text{ pm}$ ), compared to a FWHM  $\approx 100 \text{ pm}$  for Si RR sensors [8, 9] is of additional help here.

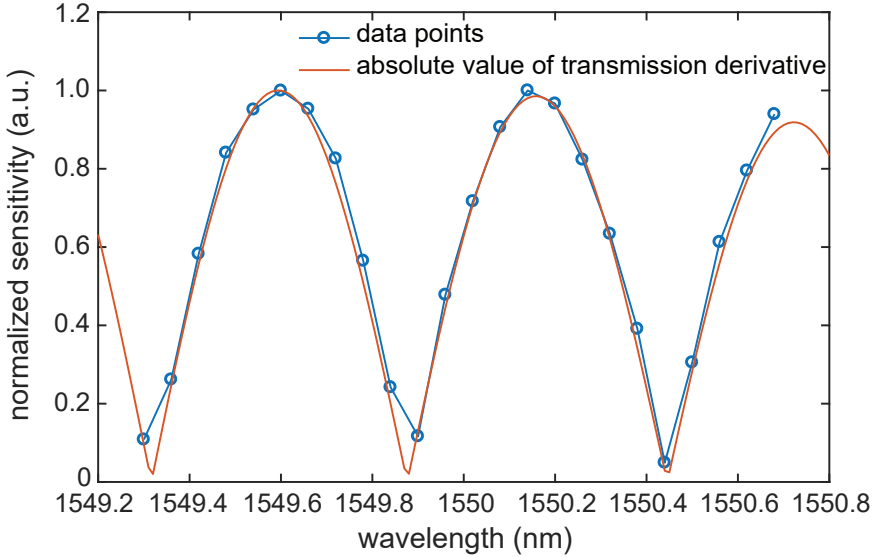


Figure 3.4: Wavelength dependence of the sensor sensitivity. The data points agree excellently with the prediction given by Eq. 3.4.

### 3.4. CONCLUSION AND OUTLOOK

Having reported the experimental results, we now discuss several remaining aspects.

As for the transfer function, specific applications, e.g., photoacoustic imaging [14], may require its frequencies at several MHz and a larger bandwidth. This can be realized with modified membrane designs. The membrane-resonance frequency scales with  $h/d^2$  [15], where  $h$  and  $d$  are the thickness and side of the square membrane, respectively. A frequency increase of 10 times thus can be easily achieved. To increase the bandwidth, the membrane can be made lossy by depositing a polymer layer on it. These adaptations go at the cost of sensitivity, which can be compensated by increasing the optical power.

The sensitivity of the sensor can be increased as follows. A first way is creating a stronger strain response to pressure. This also involves membrane redesign, now a thinner and larger membrane, which counteracts possible requirements for the transfer function. A larger membrane also offers a second way, namely a longer spiral, which adds to the sensitivity via  $\Delta\varphi$  (see Eq. 3.1). Finally, one can simply increase the optical power, as suggested by Eq. 3.4 and Figure 3.3(b). With an MZI not being a resonator, unlike a RR, there is no field enhancement. Thus, higher powers may be applied to the MZI without showing nonlinear effects. The maximum optical input power of 1.0 mW used here will already induce nonlinear effects in a Si RR sensor [10].

Combining the minimum NEP of 0.38 Pa and the maximum pressure of 341 Pa yields a dynamic range of 59 dB, which is appreciable. The trend for the NEP in Figure 3.3(c) and the option to strongly increase the optical power indicate that the NEP can be further decreased and the dynamic range can be further increased. In addition, it is possible to use higher pressures than 341 Pa.

In conclusion, we demonstrate an on-chip MZI ultrasound sensor, fabricated in SOI technology. The sensing spiral is located on a  $121\ \mu\text{m} \times 121\ \mu\text{m}$  membrane, of which the mechanical resonance is excited by ultrasound waves around 0.47 MHz. The mechanical vibrations induce optical transmission modulation, thus defining the sensor signal. As the MZI transmission function is gradual, a wide wavelength-operation range is possible. We envision that a common distributed feedback laser as light source, the MZI sensor, and a photodetector can be integrated into a handheld single unit. The sensor transfer function, centered at 0.47 MHz, has a  $-6\ \text{dB}$  bandwidth of 21.2%. We reach a maximum sensitivity of 0.62 mV/Pa and a dynamic range of 59 dB. In our measurements, the detection limit is  $0.38\ \text{mPa}/\text{Hz}^{1/2}$ . We indicate how each sensor quality can be tailored and improved. Re-designing the membrane properties and increasing the optical power are important and readily attainable means for this. The combination of its merits make this on-chip MZI ultrasound sensor very promising for various applications, e.g., all-optical photoacoustic imaging.

### 3.5. ADDENDUM: MEMBRANE BUCKLING EFFECT

The active part of the MZI sensor for ultrasound detection presented in this chapter is the MZI spiral located on the membrane. As discussed, the membrane of the sensor is fabricated on SOI material. Figure 3.5 again shows the schematic cross section of the membrane region, including part of the substrate. The SOI wafer used in the fabrication process is a 200 mm wafer of thickness around  $725\ \mu\text{m}$ , which was thinned down to  $250\ \mu\text{m}$  using grinding and polishing after the fabrication at IMEC and before membrane formation in the Kavli Nanolab Delft.

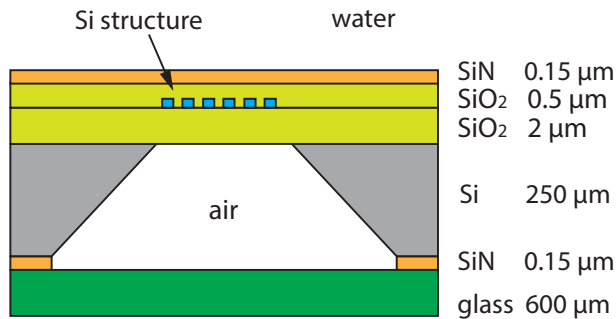


Figure 3.5: Cross section of the membrane region, showing the layered structure of the membrane, along with the supporting silicon substrate.

The fabrication process of SOI wafers includes a thermal oxidation step of silicon to create what becomes the buried oxide (BOX) layer. This step is performed at high temperature<sup>1</sup>. After oxidation, the strain of the SiO<sub>2</sub> layer at room temperature is compressive. In the process of wafer bonding and in the subsequent steps of the SOI wafer fabrication, the

<sup>1</sup>The process is not disclosed by IMEC. Thus, a reliable estimate of the built-in strain cannot be made.

compressively strained  $\text{SiO}_2$  layer is transferred to the silicon handle wafer (substrate), thus maintaining compressive strain in the BOX layer and tensile strain in the substrate and the silicon device layer. Small warpage of the SOI wafer results, to which the device layer gives only a small contribution due to its small thickness (220 nm). Local complete removal of the substrate under the BOX for membrane creation gives rise to strain relaxation of the oxide layer and strain increase of the device layer, and thus to membrane buckling. Buckling effects of membranes fabricated on SOI material have been studied already [16, 17].

3

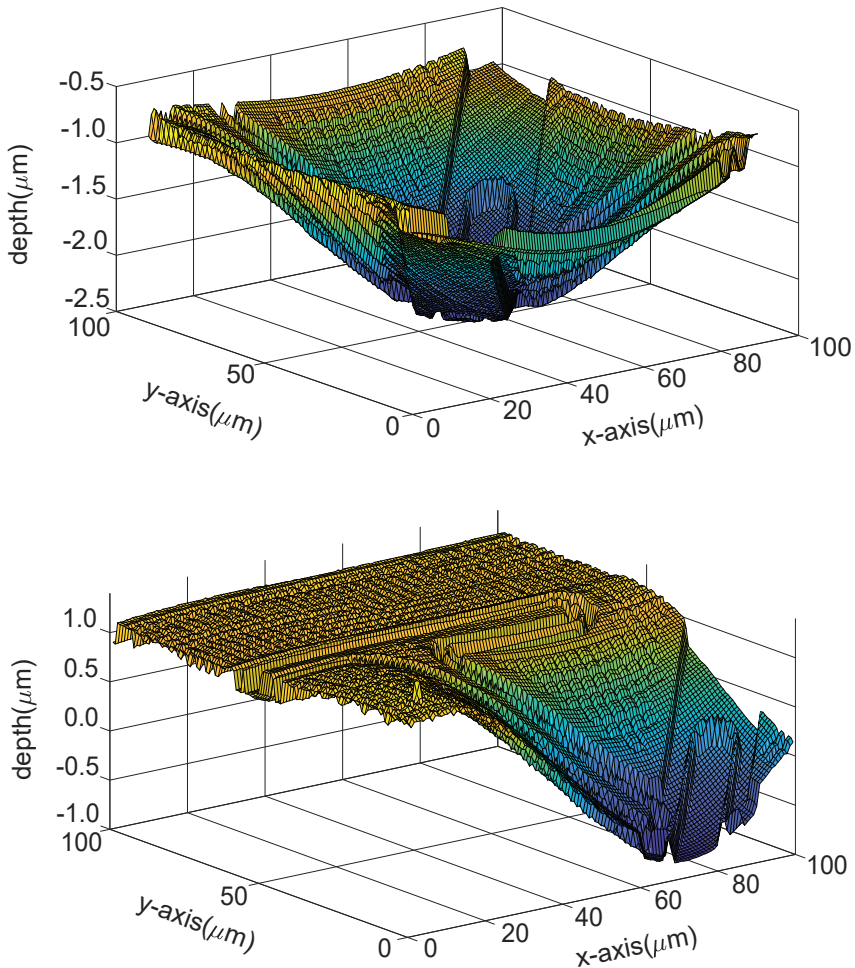


Figure 3.6: Result of an AFM measurement of a dummy membrane with the same layered structure as that of the membrane of the MZI sensor. The regular small scale structure is the tiling etched into the device layer. (a) The middle part of the membrane. (b) The single quadrant of the entire membrane region.



In fabricating the photonic structures, the integrity of the device layer gets lost. Therefore, without further deposition of layers on the chip with photonic structures, the buckling of the resulting membrane of the sensor would almost completely be determined by the silicon-oxide layer. In fabricating the actual sensor, however, two additional layers are deposited using plasma enhanced chemical vapour deposition (PECVD) and low pressure chemical vapour deposition (LPCVD), as shown in Figure 3.5. These are a 500 nm thick  $\text{SiO}_2$  layer (PECVD,  $T_{\text{dep}} = 300^\circ\text{C}$ , resulting in compressive strain in this layer at  $20^\circ\text{C}$ ) and a 150 nm thick  $\text{Si}_3\text{N}_4$  layer (LPCVD,  $T_{\text{dep}} = 850^\circ\text{C}$ , resulting in tensile strain in this layer at  $20^\circ\text{C}$ ). These additional layers will contribute to the internal stress of the layered structure that later becomes the membrane. In Figure 3.6 two atomic force microscope (AFM) images are presented of a  $121\mu\text{m} \times 121\mu\text{m}$  dummy membrane with the same layered structure as that of the membrane of the MZI sensor. The images show the middle part and a single quadrant of the square membrane, due to the limited scan field of the AFM. From the image of the membrane middle part, we see the buckling mode of the membrane has the symmetry of a square, as expected. Therefore, the single quadrant of the membrane can represent the buckling situation of the entire membrane. It is seen that the membrane is buckled downwards. From the figures, a deflection amplitude of the buckling mode of  $2.24\mu\text{m}$  is obtained.

The mechanical properties of the membrane are influenced by its internal stress and buckling. For example, the stiffness of a membrane increases with increasing buckling, an effect used to increase the operation range of DC pressure sensors built in the SOI platform, which use the principle of membrane deflection [18]. In this spirit, it is expected that the properties for sensing of ultrasound are also affected by the buckling. For instance, the vibrational modes will be influenced by the buckling, leading to a membrane-resonance frequency different from that of the corresponding unbuckled membrane. Confirmation of this is found from the simulations in [19]. The deflection amplitude of the vibrational mode in response to ultrasound depends on the initial stress level [19]. The latter effect means a difference in sensitivity of the sensor, whether it is based on an MZI or a ring resonator (RR), as in Chapter 2. In addition, even for a buckled membrane, the sensitivity of the sensor is different for the buckled-up case and the buckled-down case, since the device layer is not in the middle of the membrane. To have better control of acoustical properties of the sensor, the mechanical properties of each layer need to be known in detail for manipulating the internal stress of the membrane. Since the stress of the membrane is currently dominated by the compressive stress of the  $\text{SiO}_2$  layer, a  $\text{Si}_3\text{N}_4$  layer with a high tensile stress can be used to replace the current  $\text{Si}_3\text{N}_4$  layer of the membrane for stress compensation. The thickness of this layer, however, is limited to about 200 nm, the critical thickness beyond which layer cracking occurs due to the relaxation of strain in this layer. In this case, the lower  $\text{SiO}_2$  layer can be thinned down to decrease the compressive stress. Membranes with fully strain-balanced layered structures can be obtained using the proper thickness of each layer. Through controlling the lateral membrane dimension, the thickness and the mechanical properties of each layer, the resonance frequency and sensitivity of the sensor can be tailored to meet the specific requirement of certain applications.

Apart from the sensor characteristics reported in this chapter, another important property is the directivity function of the sensor. This is the dependence of the sensor signal,



normalized to the signal for normal incidence, on the direction of the incident ultrasound under the condition of constant distance between source and sensor. The direction is defined as the angle  $\theta$  between the normal to the membrane plane and the direction of incidence. We performed preliminary measurements of the directivity of the MZI sensor. In the experiment, the directivity is measured in a water tank by rotating an ultrasound transducer on a semicircle that is centered at the stably positioned sensor (the sensor plane is vertical) and that is in the horizontal plane through the axis of the membrane. The axis of the transducer's central lobe (which is much wider than the membrane) points to the membrane for each angle setting. This means that the emission profile of the source is not involved in the measurement results. The distance between the transducer and the sensor is such that the sensor is located in the far field of the transducer. The sensor signal was measured on the semicircle for angles  $\theta = \pm n \times (2 \text{ degrees})$ , with  $n = 0, 1, 2, \dots, 45$ .

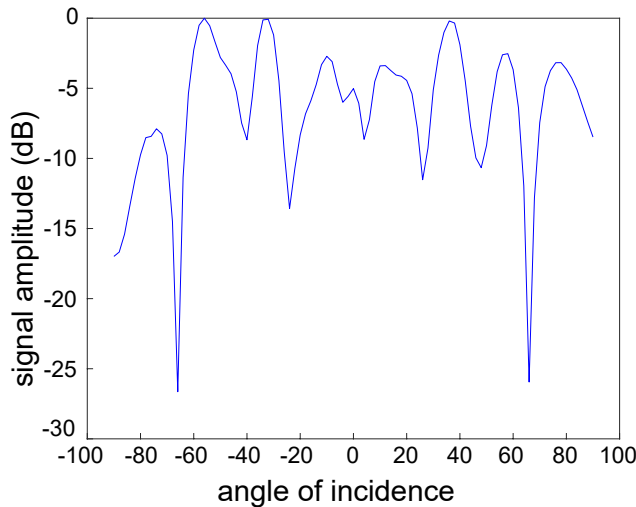


Figure 3.7: Directivity of the MZI sensor. The sensor signal is the maximum of the envelop of the pulse measured in the optical transmission of the sensor.

In Figure 3.7 an example is given of the measured directivity of the sensor. It is close to symmetric around zero degrees, as expected, but shows a strong oscillatory dependence on the angle, with a signal decrease of up to -25 dB at  $\theta = \pm 66$  degrees. A local minimum occurs at zero degrees, which means that the strain induced in the MZI as a result of the membrane vibration has a local minimum for perpendicularly incident ultrasound. This overall behavior is contrary to the expectation for an ideal (i.e., strain free and flat) clamped square membrane of a size much smaller than the acoustic wavelength. The directivity of the ideal membrane can be predicted using reciprocity. According to reciprocity, the directivity of an ultrasound sensor can be approximated by the directivity of an ultrasound source of similar characteristics, which then can be modeled using the various piston models in the literature [20]. The shape and size of the oscillating piston surface are equal to those of the membrane. For the operation regime of our sensor, de-

finned by  $ka \ll 1$  ( $k = 2\pi/\lambda$ ,  $\lambda$  = acoustic wavelength =  $3200\mu\text{m}$  and  $a$  = half the membrane side =  $60\mu\text{m}$ ), the piston models produce a completely smooth directivity that only decays weakly from unity for larger angles [20]. This is completely different from what is observed for the sensor. Roughly, for  $\theta$  in the range  $(-60, 60)$  degrees one may see a constant average directivity in Figure 3.7, but this leaves unexplained the strong oscillatory behavior and the local minimum at zero degrees. The occurrence of buckling of the membrane and the dense MZI spiral buried under the two layers constitute the main difference between the fabricated membranes and equivalent ideal membranes. This makes it plausible that the origin of the peculiar directivity can be found in the buckling effect, while possibly the dense buried spiral has an influence as well. To make this a hard conclusion, further work on the directivity is needed. An important experimental check then is measuring the directivity of a sensor with a membrane based on the fully strain-balanced layered structure discussed above.

## REFERENCES

- [1] P. V. Lambeck, *Integrated optical sensors for the chemical domain*, Measurement Science and Technology **17** (2006), p. R93.
- [2] E. Luan, H. Shoman, D. M. Ratner, K. C. Cheung, and L. Chrostowski, *Silicon photonic biosensors using label-free detection*, Sensors **18** (2018), p. 3519.
- [3] L. Z. Zehnder, *Ein neuer interferenzrefraktor*, Instrumentenkunde **11** (1981), pp. 275–285.
- [4] L. Z. Mach, *Ueber einen interferenzrefraktor*, Instrumentenkunde **12** (1982), pp. 89–94.
- [5] H. M. Nguyen, M. A. Dundar, R. W. Van Der Heijden, E. W. J. M. Van der Drift, H. W. M. Salemink, S. Rogge, and J. Caro, *Compact Mach-Zehnder interferometer based on self-collimation of light in a silicon photonic crystal*, Optics Express **18** (2010), pp. 6437–6446.
- [6] T. Ling, S.-L. Chen, and L. J. Guo, *High-sensitivity and wide-directivity ultrasound detection using high Q polymer microring resonators*, Applied Physics Letters **98** (2011), p. 204103.
- [7] B.-Y. Hsieh, S.-L. Chen, T. Ling, L. J. Guo, and P.-C. Li, *All-optical scanhead for ultrasound and photoacoustic imaging—Imaging mode switching by dichroic filtering*, Photoacoustics **2** (2014), pp. 39–46.
- [8] S. M. Leinders, W. J. Westerveld, J. Pozo, P. Van Neer, B. Snyder, P. O’Brien, H. P. Urbach, N. de Jong, and M. D. Verweij, *A sensitive optical micro-machined ultrasound sensor (OMUS) based on a silicon photonic ring resonator on an acoustical membrane*, Scientific Reports **5** (2015), p. 14328.
- [9] F. G. Peternella, B. Ouyang, R. Horsten, M. Haverdings, P. Kat, and J. Caro, *Interrogation of a ring-resonator ultrasound sensor using a fiber Mach-Zehnder interferometer*, Optics Express **25** (2017), pp. 31622–31639.
- [10] G. Priem, P. Dumon, W. Bogaerts, D. Van Thourhout, G. Morthier, and R. Baets, *Optical bistability and pulsating behaviour in Silicon-On-Insulator ring resonator structures*. Optics Express **13** (2005), pp. 9623–9628.
- [11] E. Hallynck and P. Bienstman, *Integrated optical pressure sensors in silicon-on-insulator*, IEEE Photonics Journal **4** (2012), pp. 443–450.
- [12] H. Gao, C.-H. Huang, W. Westerveld, R. Haouari, B. Troia, F. Verhaegen, R. Jansen, B. Figeys, X. Rottenberg, and V. Rochus, *Simulation and characterization of a high-sensitive micro-opto-mechanical microphone*, in *2018 19th International Conference on Thermal, Mechanical and Multi-Physics Simulation and Experiments in Microelectronics and Microsystems (EuroSimE)* (IEEE, 2018) pp. 1–4.

- [13] S. Tsesses, D. Aronovich, A. Grinberg, E. Hahamovich, and A. Rosenthal, *Modeling the sensitivity dependence of silicon-photonics-based ultrasound detectors*, *Optics Letters* **42** (2017), pp. 5262–5265.
- [14] K. Jansen, A. F. Van Der Steen, H. M. van Beusekom, J. W. Oosterhuis, and G. van Soest, *Intravascular photoacoustic imaging of human coronary atherosclerosis*, *Optics Letters* **36** (2011), pp. 597–599.
- [15] A. W. Leissa and M. S. Qatu, *Vibrations of Continuous Systems*. (McGraw-Hill, 2011) p. 238.
- [16] K. K. Ziegler, *Selectively tuning a buckled Si/SiO<sub>2</sub> membrane MEMS through joule heating actuation and mechanical restriction*, Thesis at the Air Force Institute of Technology, Ohio, USA .
- [17] R. A. Lake and R. A. Coutu, *Tunable pressure sensing applications of a MEMS buckled membrane*, in *2015 National Aerospace and Electronics Conference (NAECON)* (IEEE, 2015) pp. 228–231.
- [18] R. A. Lake and R. A. Coutu Jr, *Variable response of a thermally tuned MEMS pressure sensor*, *Sensors and Actuators A: Physical* **246** (2016), pp. 156–162.
- [19] W. J. Westerveld, S. M. Leinders, P. van Neer, H. P. Urbach, N. de Jong, M. D. Verweij, X. Rottenberg, and V. Rochus, *Optical micro-machined ultrasound sensors with a silicon photonic resonator in a buckled acoustical membrane*, in *2019 20th International Conference on Thermal, Mechanical and Multi-Physics Simulation and Experiments in Microelectronics and Microsystems (EuroSimE)* (IEEE, 2019) pp. 1–7.
- [20] K. A. Wear, C. Baker, and P. Miloro, *Directivity and frequency-dependent effective sensitive element size of needle hydrophones: Predictions from four theoretical forms compared with measurements*, *IEEE Transactions on Ultrasonics, Ferroelectrics, and Frequency Control* **65** (2018), pp. 1781–1788.



# 4

## SILICON RING RESONATORS WITH A FREE SPECTRAL RANGE ROBUST TO FABRICATION VARIATIONS

*We propose a design method for silicon ring resonators (RRs) with a free spectral range (FSR) insensitive to fabrication variations. Two waveguide-core widths are used in the RR, with opposite signs of the group-index derivative with respect to the width. This results in cancellation of the width-dependent FSR changes. The systematic deviation of the realized width from the design width is determined, and is used for calibrating the calculated relation of group index versus width. This enables a more accurate FSR value and well-aimed robust performance. We present two robust design examples. Experimental results match well with the predictions. For the deliberately introduced  $\pm 10$  nm core-width change, the FSR variation of the robust designs is only about 30% of the value measured from the RR with a single core width. This design method can be used to improve the performance of photonic integrated circuits using multiple RRs. As the FSR of a RR is not easily tunable, the robust design is beneficial to applications where an accurate FSR is required, such as in microwave photonics.*

---

This chapter is based on: B. Ouyang, Y. Xing, W. Bogaerts, and J. Caro, *Silicon ring resonators with a free spectral range robust to fabrication variations*, Optics Express **27** (2019), pp. 38698-38707.

## 4.1. INTRODUCTION

Silicon photonics has become a highly promising platform for photonic integrated circuits (PICs). Benefiting from a high refractive index contrast and a CMOS compatible fabrication process, silicon photonics enables a small device footprint, high-density packing, large-scale integration, and high-volume, low-cost production. However, the strong light confinement of silicon photonics and the nanometer-scale dimensions of the photonic structures also lead to high sensitivity of device properties to waveguide-width variations inherent to the fabrication process [1]. As a result, the performance of the PIC will deviate from the designed one. With the upscaling of PICs, the performance deviations can accumulate and get more severe rapidly, ruining the functionality. The width variations of the waveguide core result from inherent variations of various steps in the fabrication process, e.g., lithography dose and etch rate, making these variations unavoidable. Even for a well-developed silicon photonics foundry, the fabricated core width can have tens of nanometers systematic deviation from the design value, with notable variations across the wafer superimposed on the systematic deviations [2–4]. Therefore, robust optimization methods for minimizing the effects of variability in the phase of the PIC design are crucial for further developing silicon photonics [5].

Mach-Zehnder interferometers (MZIs) and ring resonators (RRs) are commonly used silicon photonic devices. Fabrication tolerant design of silicon MZIs with a robust peak-wavelength positioning has already been reported [6]. By utilizing different widths for the two arms of the MZI, width-variation induced effective index changes can be compensated, enabling a wavelength shift of  $< 60$  pm per nm width variation [6]. Similar approaches have been used for making thermally robust MZIs [7–10], again taking advantage of the two optical paths.

Unlike MZIs, RRs have only a single optical path. So, the method used for MZIs cannot be used to make the RR resonance wavelength insensitive to fabrication variations. Therefore, the resonance wavelength is, in practice, often tuned thermally after fabrication [11]. Another important RR quantity is the free spectral range (FSR), which is influenced by waveguide-width variations as well. Accurate control of the FSR is needed in many applications. For example, the channel spacing of wavelength filters and wavelength division multiplexers [12–15] based on RRs relies on the FSR. The channel spacing of such devices can go down to 25 GHz in telecom applications in the C-band, where high channel-spacing accuracy is needed. In microwave photonic applications, the FSR of the RR can be used to select carrier frequencies [16], requiring large rings with an accurate FSR. Further, the RR is a basic component of programmable PICs [17]. When these programmable PICs become large, it is important to have control of the FSR of RRs across the entire chip. The thermal tunability of the FSR is rather limited. Therefore, there is a clear need for a design method that yields a robust, well-controlled FSR for silicon RRs.

Here, we propose and demonstrate a design method for silicon RRs with an FSR robust to fabrication variations. The method is based on using two waveguide widths in the RR with opposite signs of  $\partial n_g / \partial w$  ( $n_g$  = group index,  $w$  = core width), resulting in cancellation of the effect of fabrication-induced width variations on the FSR. For the design of robust RRs according to our method, we derive a design rule and calibrate the design inputs using our experimental determination of the systematic width deviation. We successfully test the design method, both numerically and experimentally, by comparison with results

from RRs designed in the normal way, i.e., with a single waveguide width. This method does not require adjustment of the fabrication process. Our method is another example of a generic design approach that exploits cancellation effects used in MZIs [6–10]. To our knowledge, this is the first time that in a RR cancellation effects using two waveguides are exploited.

## 4.2. DESIGN METHOD

### 4.2.1. RING-RESONATOR DESIGN WITH A ROBUST FREE SPECTRAL RANGE

The FSR of a RR with a single waveguide width, expressed as frequency difference, is given by

$$\text{FSR}_f = \frac{c}{n_g L}. \quad (4.1)$$

Here,  $c$  is the speed of light in vacuum.  $L$  is the circumference of the RR. Within a first order approximation of the dispersion and expressed as a wavelength difference, the FSR equals

$$\text{FSR}_\lambda = \frac{\lambda^2}{n_g L}, \quad (4.2)$$

where  $\lambda$  is the operation wavelength. As  $c$  is a constant and  $\lambda$  is virtually constant, while  $L$  in general has a very small deviation from the design value, fabrication-induced FSR variations dominantly originate from  $n_g$  variations.

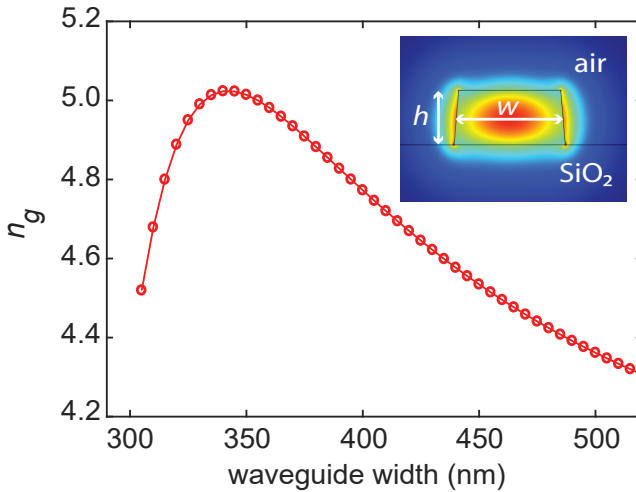


Figure 4.1: Calculated group index  $n_g$  of air-cladding silicon waveguides ( $h = 220$  nm) as a function of waveguide width  $w$  at  $\lambda = 1550$  nm. As an example, the inset shows the profile of the  $\text{TE}_{00}$  mode with  $w = 450$  nm and  $h = 220$  nm, for which  $n_g$  is calculated.

To obtain the waveguide-width dependence of  $n_g$  for the guided transverse electric  $\text{TE}_{00}$  mode in our waveguide, the basis of our design method, we use finite element sim-



ulations with COMSOL. We sweep the width of air-cladding silicon strip waveguides from 305 nm to 520 nm, using a 220 nm height and an 85° sidewall angle of the waveguide (angle given by the IMEC technology handbook; all devices used in this work have been fabricated at IMEC through the Europractice MPW service). In Figure 4.1 we present the calculated  $n_g$  as a function of waveguide width  $w$  at  $\lambda = 1550$  nm, with in the inset the calculated TE<sub>00</sub> mode profile of the waveguide with  $w = 450$  nm.  $n_g(w)$  is a relatively strong function in this width range, showing a relative change of up to 17%.  $n_g$  reaches a maximum for  $w = 340$  nm. Thus, the derivative  $\partial n_g / \partial w$  reverses sign when crossing  $w = 340$  nm. Our design method is based on this sign reversal.

Using two widths  $w_1$  and  $w_2$  for the RR, the FSR can be expressed as

$$\text{FSR}_f = \frac{c}{n_g(w_1)L_{w_1} + n_g(w_2)L_{w_2} + 2\bar{n}_{g,t}L_t}. \quad (4.3)$$

Here,  $L_{w_1}$  and  $L_{w_2}$  are the two waveguide lengths.  $L_t$  is the length of the taper.  $n_g(w_1)$  and  $n_g(w_2)$  are the corresponding group indices.  $\bar{n}_{g,t}$  is the average group index of the tapers. Figure 4.2 shows the schematic of this RR design robust to width variations. The condition for this robustness is expressed by the following design rule:

$$\left. \frac{\partial n_g(w)}{\partial w} \right|_{w_1} L_{w_1} + \left. \frac{\partial n_g(w)}{\partial w} \right|_{w_2} L_{w_2} = 0. \quad (4.4)$$

Equation 4.4 can be satisfied for opposite signs of the derivatives, i.e., for  $w_1$  and  $w_2$  on each side of the maximum of  $n_g(w)$ . Thus, the effect of fabrication-induced  $n_g$  variations on the FSR can be cancelled for proper choice of  $L_{w_1}$  and  $L_{w_2}$ . In this, we assume that the variations of  $w_1$  and  $w_2$  have a very similar and small magnitude, such that both derivatives may be considered as constant. The effect of tapers is neglected in Eq. 4.4, because these are very short compared to the circumference of the RR. Besides, the abovementioned cancellation effect also occurs between the wide and narrow side of a taper.

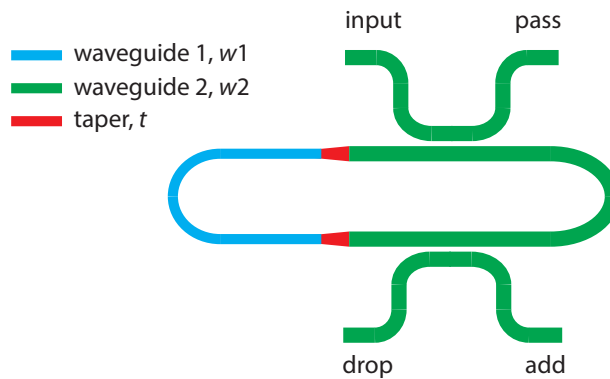


Figure 4.2: Schematic of the RR design with two waveguide widths, giving an FSR robust to waveguide-width variations.

### 4.2.2. CALIBRATION OF THE DESIGN INPUTS USING THE SYSTEMATIC WIDTH DEVIATION

As can be seen in Figure 4.1, the width-dependence of  $\partial n_g / \partial w$  is particularly strong below 340 nm, making it hard to satisfy Eq. 4.4 for fabricated widths with a strong systematic deviation from the design value. This implies that the systematic deviation of the widths needs to be known. The systematic width deviation for the IMEC process is provided for a rather limited number of design values as part of their design kit. Therefore, we experimentally determine the systematic width deviation from measurements of the optical transmission of ten test MZIs. These MZIs have a constant path-length difference  $\Delta L$ , but various waveguide widths. The width of the two arms of the MZIs is the same, ranging from 310 nm to 490 nm among the MZIs. The applied wavelength range is 1549–1551 nm. A cosine function, the common transmission function of an MZI, is fitted to the measured transmission curves, yielding the FSR of each MZI as a fit parameter. The FSR, in turn, gives the  $n_g$  of the waveguide at  $\lambda = 1550$  nm, using the equivalent of Eq. 4.2, with  $L$  replaced by  $\Delta L$ . Figure 4.3(a) shows an example of a measured MZI transmission spectrum, for a design width of 450 nm, along with the cosine fitted to the data points.

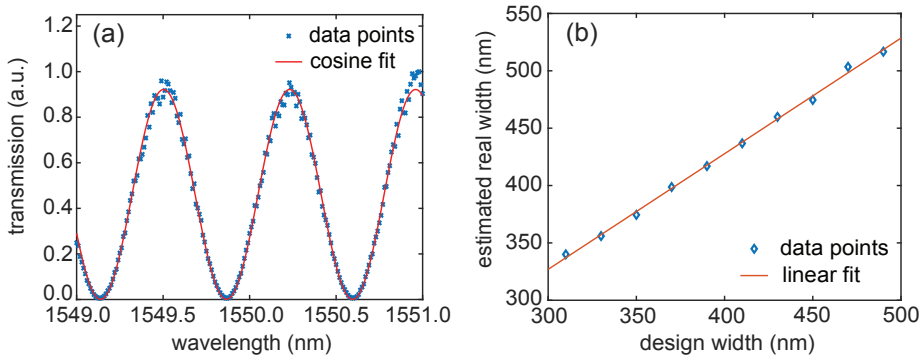


Figure 4.3: (a) Measured transmission of a test MZI with a design width of 450 nm, together with the fitted cosine. (b) Estimated real waveguide width as a function of design width.

To arrive at a single  $n_g$  value for each width that sufficiently represents the whole wafer, we measure several MZIs of the same design across a proper fraction of the wafer and repeat the  $n_g$  extraction. The final experimental  $n_g$  values for each width are obtained by averaging over the extracted values from MZIs of the same design. In this procedure, the  $n_g$  variations across the wafer are averaged out to a certain extent.

For each design width, we then estimate the real width after fabrication with the aid of the simulated  $n_g$  versus  $w$  relation in Figure 4.1, which we use as a lookup table. By picking the various measured  $n_g$  values in the simulation data, we find the fabricated width of the measured MZIs. Here, we use as a guide that according to the IMEC technology handbook the fabricated width exceeds the design width. Moreover, this width bias should depend smoothly on the design width. As we are using average  $n_g$  values, our procedure gives the best estimate of the average real width, while across the wafer the width will vary around the estimate. This procedure leads to the relation between the design width and the esti-

mated real width presented in Figure 4.3(b), which also shows a high quality linear fit to the data points. The relation provides the systematic width deviation for designs in this work. From our estimate, the fabricated width for the design width of 450 nm is 478.1 nm. This is rather close to 475.4 nm stated in the IMEC handbook.

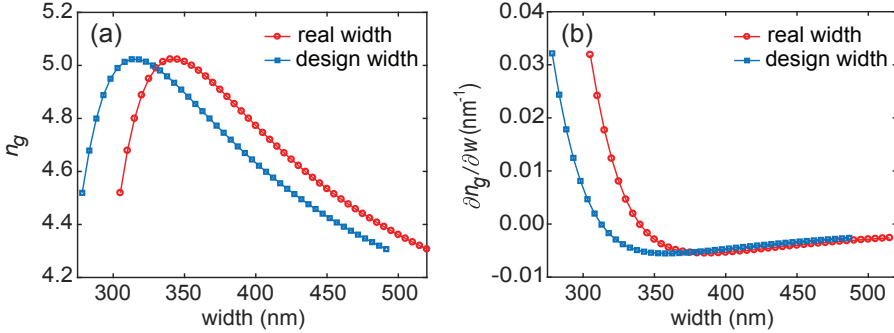


Figure 4.4: (a)  $n_g$  versus width. The blue curve is obtained by calibrating the red curve from Figure 4.1 using the linear function in Figure 4.3(b). (b) Derivative curves  $\partial n_g / \partial w$  calculated from the curves in (a).

Using the linear fit in Figure 4.3(b), the function  $n_g(w)$  in Figure 4.1 can now be calibrated to take into account the width-dependent core-width increase after fabrication. Assuming the width in Figure 4.1 is the real width, the corresponding design width is calculated using the linear function in Figure 4.3(b). This process yields the calibrated function (blue curve) in Figure 4.4(a), which has shifted to the left with respect to the red curve. Plots of the related derivative curves  $\partial n_g / \partial w$  are shown in Figure 4.4(b). The calibrated  $n_g$  and  $\partial n_g / \partial w$  curves serve as inputs for Eqs. 4.3 and 4.4 in the design process of robust RRs.

### 4.3. DESIGN IMPLEMENTATION

Here, we study in detail two designs for robust RRs, robust 1 and robust 2. We choose  $\text{FSR} = 1 \text{ nm}$  (124.783 GHz) at  $\lambda = 1550 \text{ nm}$ . Robust 1 has design widths  $w_1 = 296 \text{ nm}$  and  $w_2 = 450 \text{ nm}$ .  $w_2$  is a commonly used width, which has a negative  $\partial n_g / \partial w$  value. The value of  $w_1$  is chosen such that the derivative  $\partial n_g / \partial w$  is positive, but relatively small. This is to arrange, according to the shape of  $\partial n_g / \partial w$  in Figure 4.4(b), that  $\partial n_g / \partial w$  varies relatively weakly for width variations around  $w_1$ . In this way, the range of width variations that can be tolerated before the design rule (Eq. 4.4) breaks down is maximized. Using the same argument, we arrive for robust 2 at the values  $w_1 = 300 \text{ nm}$  and  $w_2 = 360 \text{ nm}$ . For both robust RRs the taper length is  $9 \mu\text{m}$ , enabling a smooth transition between the two widths. The average group index  $\overline{n_{g,t}}$  of the tapers is calculated by averaging the group indices of the waveguides with the widths between  $w_1$  and  $w_2$ , using the points of the calibrated curve in Figure 4.4(a). For robust 1 and robust 2, this gives average group index values of 4.76 and 4.96, respectively. The values of  $L_{w_1}$  and  $L_{w_2}$  are calculated using Eqs. 4.3 and 4.4. For robust 1 (robust 2), we obtain  $L_{w_1} = 120.4 \mu\text{m}$  ( $212.1 \mu\text{m}$ ) and  $L_{w_2} = 389.5 \mu\text{m}$  ( $260.2 \mu\text{m}$ ).

To demonstrate the robustness of the FSR of robust 1 and robust 2 to width variations,

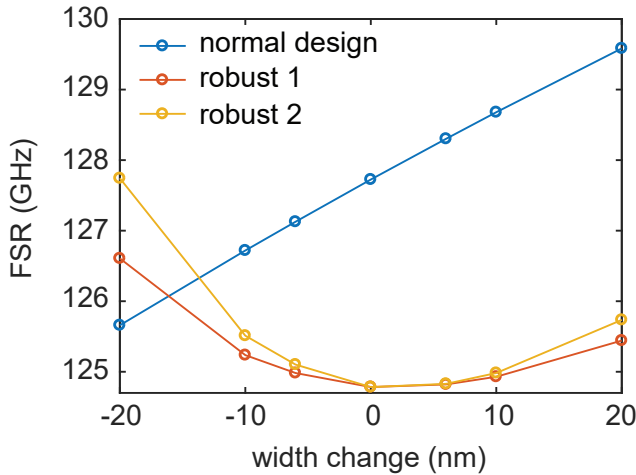


Figure 4.5: Predicted FSR as a function of waveguide-width variation, for devices robust 1 and robust 2. For comparison, the behavior for a normal design is also included.

we duplicate these devices by applying intentional width variations of  $\pm 6$  nm,  $\pm 10$  nm and  $\pm 20$  nm, and calculate the predictions for the FSR using Eq. 4.3 and the calibrated  $n_g$  curve. Thus, design sets result that each have seven devices. For comparison, we also include a RR with a single design width of 450 nm and implement the same width variations. For this normal design, we use the red curve in Figure 4.4(a), as would be done without prior knowledge of the systematic width increment. Similar to the robust RRs, the geometry of the normal design RRs is a racetrack. The total length of the normal design RRs is  $529.8 \mu\text{m}$ . All RRs have the same bend radius of  $30 \mu\text{m}$ . The directional coupler gap of all RRs is designed to be 250 nm when there is no intentional width change. The calculated results are given in Figure 4.5. For the range given by the  $\pm 10$  nm variation, the FSR variation for robust 1 and robust 2, defined by the maximum FSR minus the minimum FSR in the range, is only 23% and 37% of the normal design's FSR variation, respectively. This clearly indicates that the design method works in theory and thus is ready for application in RR fabrication.

#### 4.4. EXPERIMENT RESULTS

To make an experimental test of our design method, robust RRs and normal design RRs have been fabricated in one MPW run, which followed the run of the test MZIs. RRs from four dies are characterized, for comparison of the FSR values. The die locations cover the range from the center to the edge of the 200 mm wafer. The pitch of the dies is 21.84 mm. Transmission spectra of the RRs are measured by sweeping the wavelength of a tunable laser coupled to the input port of the RR and measuring the output power at the pass port with a photodetector. The transmission spectrum of RR robust 1 on die 3 is presented in Figure 4.6(a), showing ten resonance dips. The depth of the dips shows a rather strong variation (8.6 dB) across the spectrum. This results from unresolved resonance splittings

due to backscattering in the ring [18], with the degree of splitting and its asymmetry depending on wavelength. We find, as expected according to this explanation, that variation of the dip depth occurs in a similar way for the normal design RRs. This indicates that indeed the observed behavior is not due to the robust design. Attribution of the behavior to resonance splitting is confirmed from the somewhat deviating line shape of the dips of smaller depth. For example, the dip close to 1551.2 nm [marked with an arrow in Figure 4.6(a)] shows a rather small, but observable asymmetry, contrary to the deeper dips, and has a full width at half minimum exceeding that of the deeper dips, features typical for a (weak) asymmetric resonance splitting.

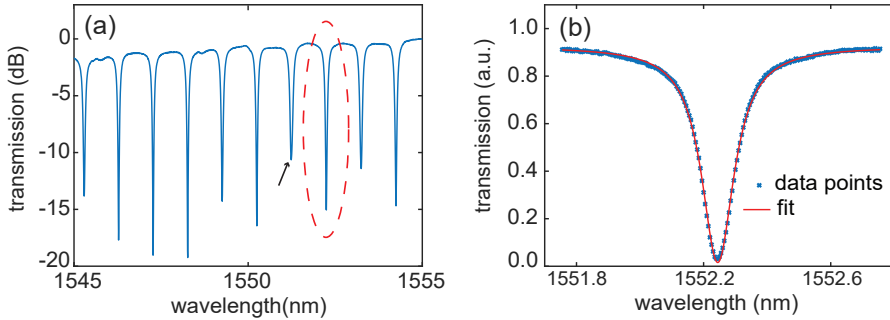


Figure 4.6: (a) Measured normalized transmission spectrum of RR robust 1 from die 3. (b) Zoom-in of the dip near 1552 nm in (a) (highlighted by the red ellipse). The red curve is a fit of Eq. 4.5 to the data points.

From the spectrum, the FSR at 1550 nm is extracted as follows. We first normalize the spectrum and locate the two resonance dips near 1548 and 1552 nm, each in a 1 nm wavelength range. We then fit the following function for the transmission at the pass port of an add-drop RR [19] to the dips:

$$T_{\text{pass}}(\lambda) = a \frac{(\lambda - \lambda_r)^2 + \alpha (\gamma_r/2)^2}{(\lambda - \lambda_r)^2 + (\gamma_r/2)^2}. \quad (4.5)$$

$\lambda_r$  and  $\gamma_r$  are the resonance wavelength and the full width at half minimum of the dip, respectively.  $\alpha$  gives the transmission level at  $\lambda_r$ . The prefactor  $a$  is included, as the wing of the dip may not reach the value unity due to the overall spectrum normalization. The measured dip near 1552 nm in Figure 4.6(a) is shown in Figure 4.6(b), together with the resulting fit. For the two dips, the fits yield the two  $\lambda_r$  values, which span 4 FSRs. The curve fitting also yields the confidence bounds of the  $\lambda_r$  values. We use these to obtain the uncertainty of the FSR to be calculated. In spite of the weak resonance splitting, the quality of the fit of Eq. 4.5 to the measured dips is high. The weak asymmetry of the dip may slightly influence the quality of fits. But this influence is taken care of by the confidence bounds of the fits and is reflected in the error bars of the FSR points, which are small, as can be seen in Figure 4.7. By converting the  $\lambda_r$  values to frequencies in vacuum and dividing the frequency difference by 4, we arrive at the FSR at 1550 nm expressed as a frequency difference. In this procedure, which we follow for all measured FSRs discussed below, we neglect the dispersion of the FSR, since the range considered is short.

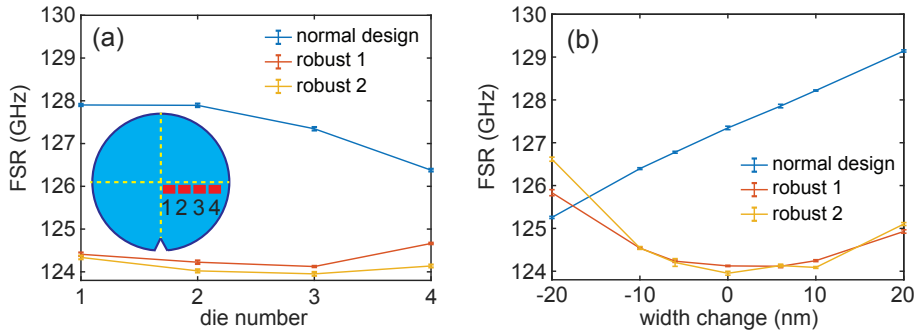


Figure 4.7: (a) Measured FSRs from die 1 to die 4, for RRs without intentional width variations. The inset shows the die locations on the wafer. (b) The measured FSR from die 3 as a function of intentional waveguide-width change.

Figure 4.7(a) shows the measured FSRs of the RRs robust 1 and robust 2 and of the normal design RR, from the four dies with locations as given in the inset of the figure. These RRs do not have intentional width variations. For robust 1 and robust 2, the FSR first decreases very similarly from die 1 to die 3 and then shows a somewhat dissimilar increase from die 3 to die 4. Along with this, the FSR of the normal design decreases from die 1 to die 4, i.e., from the wafer center towards its edge. The latter behavior is explained from a width decrease between die 1 and die 4 [see Eq. 4.1 and Figure 4.4(a)]. Such a width decrease towards the wafer edge agrees with the results in [3, 4]. This decrease for the normal design also applies to robust 1 and robust 2, leading to a minimum of FSR on die 3. The FSR behavior of these robust RRs is consistent with the FSR behavior in Figure 4.5, which shows a minimum with decreasing width as well. The minimum suggests that the robust RRs of die 3 obey  $\partial\text{FSR}/\partial w \approx 0$ , implying that the realized width on die 3 is closest to the estimate of Figure 4.3(b). It is logical that a die between the wafer center and edge, in this case die 3, gives results closest to our estimate, since the width decreases from the center to the edge and the relation in Figure 4.3(b) (used to obtain the design inputs for the robust RRs) represents the average width deviation across the wafer. Further, the FSR of the robust RRs is considerably closer to the design value (124.783 GHz) than the FSR of the normal design. This goes together with a clearly smaller FSR variation across the dies for the robust RRs than for the normal design RR. The findings from Figure 4.7(a) constitute experimental proof for the validity of our design method for robust devices.

Because the widths on die 3 are closest to the estimate, we further measure the RRs with deliberately applied width variations on die 3. This leads to the FSR values in Figure 4.7(b). The FSR behavior of robust 1, robust 2 and the normal design is highly similar to that in Figure 4.5, albeit that the FSR values from die 3 are slightly smaller. This provides further proof that our method works. The FSR difference may result from the interplay of several possible causes not considered here, such as a small variation of the waveguide height and a small change for this fabrication run of the function describing the systematic width deviation [given in Figure 4.3(b)]. We also see the strong similarity of Figure 4.5 and Figure 4.7(b) as an apparent proof that reliable determination of the FSR is indeed not prevented by occurrence of the unresolved splittings of transmission dips discussed

above.

In Table 4.1 we give the deviation of the FSR from the design value and the range-dependent FSR variation,  $\Delta_{\text{FSR}}$ . For example, for the  $[-10 \text{ nm}, 10 \text{ nm}]$  range,  $\Delta_{\text{FSR}}$  of robust 1 and robust 2 are only 23% and 32% of  $\Delta_{\text{FSR}}$  measured from the normal design, respectively. These more detailed results from die 3 confirm the validity of our method. Though the FSR variation of robust RRs becomes larger for deliberately applied width changes approaching  $-20 \text{ nm}$  due to breakdown of the design rule (see Eq. 4.4), this will rarely occur in practice. For a well-developed foundry such as ours (IMEC), the width change across a 200 mm wafer is mostly within 20 nm [3, 4]. By using the calibration of the systematic width deviation of Figure 4.3(b), the fabrication-induced width changes across the wafer will thus mainly occur in the  $[-10 \text{ nm}, 10 \text{ nm}]$  range (total change still 20 nm) around the estimated real width. Therefore, for the robust RRs, the resulting FSR variations will have small magnitudes according to the values we obtain in Table 4.1 for the  $[-10 \text{ nm}, 10 \text{ nm}]$  range by applying intentional width variations. FSR variations with stronger magnitudes due to fabrication-induced width variations are not likely to occur. This is proven in Figure 4.7(a), where the data points only involve fabrication-induced effects on the FSR.

Table 4.1: Measured FSR deviations from the design value (124.783 GHz) and range-dependent FSR variations  $\Delta_{\text{FSR}}$  for the measured devices on die 3. The uncertainty of each number results from the uncertainties of the FSR values derived from the transmission data. The uncertainties of the FSR values result from the confidence bounds of the two  $\lambda_r$  values (see Section 4.4), using uncertainty propagation.

	normal design ( $w = 450 \text{ nm}$ )	robust 1 ( $w_1 = 296 \text{ nm}$ ) ( $w_2 = 450 \text{ nm}$ )	robust 2 ( $w_1 = 300 \text{ nm}$ ) ( $w_2 = 360 \text{ nm}$ )
FSR deviation (GHz)	$2.56 \pm 0.04$	$0.66 \pm 0.02$	$0.83 \pm 0.05$
$\Delta_{\text{FSR}}$ (GHz), $[-6 \text{ nm}, 6 \text{ nm}]$ range	$1.08 \pm 0.05$	$0.12 \pm 0.04$	$0.3 \pm 0.1$
$\Delta_{\text{FSR}}$ (GHz), $[-10 \text{ nm}, 10 \text{ nm}]$ range	$1.82 \pm 0.03$	$0.42 \pm 0.04$	$0.59 \pm 0.06$
$\Delta_{\text{FSR}}$ (GHz), $[-20 \text{ nm}, 20 \text{ nm}]$ range	$3.89 \pm 0.04$	$1.72 \pm 0.08$	$2.66 \pm 0.07$

## 4.5. CONCLUSION AND OUTLOOK

In conclusion, we have demonstrated an approach for making the FSR of silicon RRs robust to waveguide-width variations, comprising two steps: i) Estimating the systematic width deviation using transmission measurements on test MZIs, leading to calibration of our calculated  $n_g(w)$  and  $\partial n_g / \partial w(w)$  functions and ii) Including two waveguide widths in a single RR. The two widths have opposite signs of  $\partial n_g / \partial w$ , thus compensating the FSR variation resulting from width variations superimposed on the systematic deviation. For two design cases, we aim for an FSR of 124.783 GHz (1 nm). Measurements show that the FSR deviation and variation of the robust designs drop clearly compared to those of the normal design. For the deliberately introduced  $\pm 10 \text{ nm}$  width change, the FSR variations in this range are only 0.42 GHz and 0.59 GHz for the two robust designs. These values are about 30% of the value measured from the normal design.

Our method, a new example of the generic design method that exploits cancellation effects using two waveguides, can be applied to PICs comprising multiple RRs. As a step in this direction, it will be important to explore the design freedom for the robust RRs in obtaining certain characteristic quantities (e.g., a predefined quality factor) subject to the

restrictions imposed by the two waveguide widths and lengths, in particular the narrow width ( $\approx 300$  nm in this work) in view of its higher propagation loss. In this, the loss in the directional couplers should be taken into account and tailored. Finally, our type of estimate of the systematic width deviation and the resulting calibration of the design inputs can be applied to other robust methods in [6–10] for more accurate designs, effectively improving performance.

#### 4.6. ADDENDUM: SILICON MZIs WITH A FREE SPECTRAL RANGE ROBUST TO FABRICATION VARIATIONS

In this addendum, it is demonstrated that the design method for silicon RRs with an FSR robust to fabrication variations can be applied to MZIs as well. Similar to the robust RRs, two waveguide widths are used, each for an arm of the MZI. In Figure 4.8 the schematic of a robust MZI is given.



Figure 4.8: Schematic of the MZI design with two waveguide widths, giving an FSR robust to waveguide-width variations. The sketched MZI is shaped differently from the one in Figure 1.8, but is topologically the same.

The FSR of this MZI with two waveguide widths, expressed as a frequency difference, is given by

$$\text{FSR}_f = \frac{c}{n_g(w1)L_{w1} - n_g(w2)L_{w2} + 2n_{g,t1}L_{t1} - 2n_{g,t2}L_{t2}}, \quad (4.6)$$

where the various quantities that are defined as before. The indices  $t1$  and  $t2$  refer to the tapers of arm 1 and 2, respectively, which are 450 nm wide at the connection to the central section of the MMIs. The main difference with the expression of the FSR of a RR is the occurrence of the minus signs in the denominator, which results from the phase difference between the guided modes arriving via the two arms at the output MMI. Neglecting the contribution of the tapers as before, the condition for robustness is given by the following design rule:

$$\left. \frac{\partial n_g}{\partial w} \right|_{w1} L_{w1} - \left. \frac{\partial n_g}{\partial w} \right|_{w2} L_{w2} = 0. \quad (4.7)$$



Eq. 4.7 can be satisfied in this case for equal signs of the derivatives, i.e.,  $w_1$  and  $w_2$  on the same side of the maximum of the function  $n_g(w)$  plotted in Figure 4.4(a). In the same way as for robust RRs, the effect of fabrication-induced  $n_g$  variations on the FSR is then cancelled. In this, we again assume that the variations of  $w_1$  and  $w_2$  have very similar and small magnitude, such that both derivatives may be considered as constant. The calibration of the design inputs introduced before is also used here. From the calibrated curves in Figure 4.4(a), we choose the widths at the right side of the maximum, where the width-dependence of  $\partial n_g / \partial w$  is weak for avoiding the breakdown of the design rule. For widths in this range the propagation loss is also smaller than for widths to the left of the maximum.

Here, design examples are given for two robust MZIs, called robust MZI 1 and robust MZI 2. We choose FSR = 4 nm (499.134 GHz) at  $\lambda = 1550$  nm. Robust MZI 1 has design widths  $w_1 = 450$  nm and  $w_2 = 360$  nm. For robust MZI 2 we take  $w_1 = 470$  nm and  $w_2 = 400$  nm. To make Eq. 4.7 applicable, the taper length for both robust MZIs should be chosen such that the contribution of the tapers to the FSR variations can indeed be neglected. The values of  $L_{w_1}$  and  $L_{w_2}$  are calculated using Eqs. 4.6 and 4.7. For robust 1 (robust 2), we obtain  $L_{w_1} = 400.9 \mu\text{m}$  ( $409.4 \mu\text{m}$ ) and  $L_{w_2} = 242.4 \mu\text{m}$  ( $255.9 \mu\text{m}$ ).

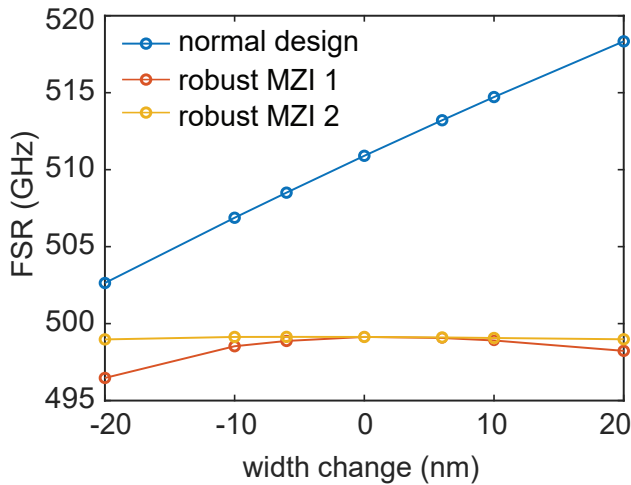


Figure 4.9: Predicted FSR as a function of waveguide-width change for devices robust MZI 1 and robust MZI 2. For comparison, the behavior for a normal design is also included.

To demonstrate the robustness of the FSR of the two design examples to width variations, we duplicate these devices by applying intentional width variations of  $\pm 6$  nm,  $\pm 10$  nm and  $\pm 20$  nm, and calculate the predictions for the FSR using Eq. 4.6 and the calibrated  $n_g$  curve in Figure 4.4(a). Thus, design results of seven devices are obtained. For comparison, we also include an MZI of normal design, with a single waveguide width of 450 nm, and implement the same width variations. For this normal design, we use the red curve in Figure 4.4(a), as would be done without prior knowledge of the systematic width increment. The calculation results are given in Figure 4.9. The width-dependent FSR variation

of the normal MZIs shows a similar trend as for the normal RRs in Figure 4.5. For the robust MZI 1, the FSR clearly decreases on either side of the zero width change. This behavior is opposite to that of the robust RRs, which show an FSR increase (see Figure 4.5). For the robust MZI 2, a weak maximum occurs at the  $-6$  nm width change, with the FSR decreasing on either side of the maximum. The FSR variation of robust MZI 2 is hardly visible in the figure. For the range given by the  $\pm 10$  nm width change, the FSR variation for robust MZI 1 and robust MZI 2, defined by the maximum FSR minus the minimum FSR in the range, is only 8% and 1% of the normal design's FSR variation, respectively. Since we avoid narrow waveguides (widths around 300 nm, as used for the robust RRs), which have a strong width-dependence of  $\partial n_g / \partial w$ , this predicted performance of robust MZIs is much better than that of robust RRs. Based on the very good agreement between the predictions and the experimental results of robust RRs, we can expect that the design method for robust MZIs will also work in practice and can be tested on devices fabricated according to the above specifications. As discussed previously, for a well-developed foundry such as IMEC, the fabrication-induced width variations across the wafer will mainly occur in the  $[-10$  nm, 10 nm] range around the estimated real width. The design method for robust MZIs can lower the FSR variations by two orders of magnitude for this range (see above the result for robust MZI 2). This is a very significant effect. This generic design method for MZIs can be applied to PICs with many MZIs as well, such as cascaded MZI based filters [20, 21].

## REFERENCES

- [1] W. Bogaerts, Y. Xing, and U. Khan, *Layout-aware variability analysis, yield prediction, and optimization in photonic integrated circuits*, IEEE Journal of Selected Topics in Quantum Electronics **25** (2019), pp. 1–13.
- [2] Z. Lu, J. Jhoja, J. Klein, X. Wang, A. Liu, J. Flueckiger, J. Pond, and L. Chrostowski, *Performance prediction for silicon photonics integrated circuits with layout-dependent correlated manufacturing variability*, Optics Express **25** (2017), pp. 9712–9733.
- [3] Y. Xing, J. Dong, S. Dwivedi, U. Khan, and W. Bogaerts, *Accurate extraction of fabricated geometry using optical measurement*, Photonics Research **6** (2018), pp. 1008–1020.
- [4] Y. Xing, M. Wang, A. Ruocco, J. Geessels, U. Khan, and W. Bogaerts, *Extracting multiple parameters from a compact circuit for performance evaluation*, in *European Conference on Integrated Optics, Belgium* (2019).
- [5] W. Bogaerts and L. Chrostowski, *Silicon photonics circuit design: methods, tools and challenges*, Laser & Photonics Reviews **12** (2018), p. 1700237.
- [6] S. Dwivedi, H. D’heer, and W. Bogaerts, *Maximizing fabrication and thermal tolerances of all-silicon FIR wavelength filters*, IEEE Photonics Technology Letters **27** (2015), pp. 871–874.
- [7] M. Uenuma and T. Motooka, *Temperature-independent silicon waveguide optical filter*, Optics Letters **34** (2009), pp. 599–601.
- [8] B. Guha, A. Gondarenko, and M. Lipson, *Minimizing temperature sensitivity of silicon Mach-Zehnder interferometers*, Optics Express **18** (2010), pp. 1879–1887.
- [9] S. Dwivedi, H. D’heer, and W. Bogaerts, *A compact all-silicon temperature insensitive filter for WDM and bio-sensing applications*, IEEE Photonics Technology Letters **25** (2013), pp. 2167–2170.
- [10] P. Xing and J. Viegas, *Broadband CMOS-compatible SOI temperature insensitive Mach-Zehnder interferometer*, Optics Express **23** (2015), pp. 24098–24107.
- [11] P. Dong, W. Qian, H. Liang, R. Shafiiha, D. Feng, G. Li, J. E. Cunningham, A. V. Krishnamoorthy, and M. Asghari, *Thermally tunable silicon racetrack resonators with ultralow tuning power*, Optics Express **18** (2010), pp. 20298–20304.
- [12] Y. Yanagase, S. Suzuki, Y. Kokubun, and Sai Tak Chu, *Box-like filter response and expansion of FSR by a vertically triple coupled microring resonator filter*, Journal of Lightwave Technology **20** (2002), pp. 1525–1529.
- [13] F. Xia, M. Rooks, L. Sekaric, and Y. Vlasov, *Ultra-compact high order ring resonator filters using submicron silicon photonic wires for on-chip optical interconnects*, Optics Express **15** (2007), pp. 11934–11941.

- [14] M. S. Dahlem, C. W. Holzwarth, A. Khilo, F. X. Kärtner, H. I. Smith, and E. P. Ippen, *Reconfigurable multi-channel second-order silicon microring-resonator filterbanks for on-chip WDM systems*, *Optics Express* **19** (2011), pp. 306–316.
- [15] S. Feng, T. Lei, H. Chen, H. Cai, X. Luo, and A. W. Poon, *Silicon photonics: from a microresonator perspective*, *Laser & Photonics Reviews* **6** (2012), pp. 145–177.
- [16] J. Lloret, J. Sancho, M. Pu, I. Gasulla, K. Yvind, S. Sales, and J. Capmany, *Tunable complex-valued multi-tap microwave photonic filter based on single silicon-on-insulator microring resonator*, *Optics Express* **19** (2011), pp. 12402–12407.
- [17] D. Pérez, I. Gasulla, L. Crudgington, D. J. Thomson, A. Z. Khokhar, K. Li, W. Cao, G. Z. Mashanovich, and J. Capmany, *Multipurpose silicon photonics signal processor core*, *Nature Communications* **8** (2017), p. 636.
- [18] A. Li, T. Van Vaerenbergh, P. De Heyn, P. Bienstman, and W. Bogaerts, *Backscattering in silicon microring resonators: a quantitative analysis*, *Laser & Photonics Reviews* **10** (2016), pp. 420–431.
- [19] F. G. Peternella, B. Ouyang, R. Horsten, M. Haverdings, P. Kat, and J. Caro, *Interrogation of a ring-resonator ultrasound sensor using a fiber Mach-Zehnder interferometer*, *Optics Express* **25** (2017), pp. 31622–31639.
- [20] F. Horst, W. M. Green, S. Assefa, S. M. Shank, Y. A. Vlasov, and B. J. Offrein, *Cascaded Mach-Zehnder wavelength filters in silicon photonics for low loss and flat pass-band WDM (de-) multiplexing*, *Optics Express* **21** (2013), pp. 11652–11658.
- [21] H. Yu, M. Chen, P. Li, S. Yang, H. Chen, and S. Xie, *Silicon-on-insulator narrow-passband filter based on cascaded MZIs incorporating enhanced FSR for downconverting analog photonic links*, *Optics Express* **21** (2013), pp. 6749–6755.



# 5

## CONCLUSION AND OUTLOOK

## 5.1. CONCLUSION

In Chapter 1, the background knowledge relevant to the work of this thesis is first introduced, followed by the formulation of research goals. The research described in this thesis partly is a continuation of previous work on a silicon RR ultrasound sensor developed in our department [1]. This sensor has a high sensitivity and a low detection limit [1]. Benefiting from the CMOS compatible fabrication techniques for integrated photonics, this sensor holds the promise of high volume production, low cost and small footprint, while its photonic nature implies immunity to electromagnetic interference. These properties make this RR sensor very appealing for applications requiring ultrasound detection. The goal of the present research is to overcome the main challenges that derive from the aforementioned previous work. These challenges are: i) An improved interrogation method to meet the special requirements of the RR sensor. ii) An alternative integrated photonics sensor that does not have the inherent disadvantages of the RR sensor. iii) Special design methods of silicon integrated photonics devices, in particular RRs and MZIs, for avoiding the high sensitivity of their properties to fabrication variations. These three challenges are sequentially addressed in Chapters 2, 3, and 4.

In Chapter 2, a compact integrated photonics interrogator, the so-called MediGator, for the RR ultrasound sensor is presented. It consists of a special light source and an InP MZI with a  $3 \times 3$  MMI and three integrated photodetectors. The small footprint of the MZI chip enables high temperature stability and negligible signal drift during interrogation of the sensor. The light source has a  $-3$  dB bandwidth of 1.5 nm, a power density of 9 dBm/nm and a tuning range of 5.7 nm, providing a wide measurement range, sufficient signal level and robust alignment to the resonance of the RR sensor, respectively. The mathematical procedure of the interrogation and the numerically calculated results are given, which yield the optimum design of the MZI of the Medigator. Using the MediGator, the frequency response and the sensitivity at the resonance frequency of the sensor were measured. The time traces of the three output signals match well with the calculated results. Interrogation of the RR sensor at its resonance frequency shows good linearity of the relation between the ultrasound pressure and the resulting amplitude of the resonance-wavelength modulation for ultrasound pressures in the range of 1.47–442.4 Pa. This linear range is two times larger than the value obtained for the modulation method. The high interrogation performance, ease of operation, temperature robustness, compactness and cost effectiveness of the MediGator make it very suitable for interrogating the RR ultrasound sensor.

In Chapter 3, a silicon MZI ultrasound sensor is demonstrated. One spiral arm of the MZI is located on a thin membrane, which is sensitive to incident ultrasound waves, similar to the case of a RR sensor on a membrane. The membrane's vibrational mode is excited, resulting in length modulation of the spiral and strain-induced effective index modulation of the spiral's waveguide. These effects lead to modulation of the transmission of the MZI at a fixed operation wavelength. The transmission modulation characterizes the incident ultrasound. Experimental results show that the transfer function of the sensor is centered at 0.47 MHz and has a  $-6$  dB bandwidth of 21.2%. The sensor sensitivity is a linear function of the optical input power. Using an input power of 1.0 mW, we obtain a high sensitivity of 0.62 mV/Pa, a low detection limit of 0.38 mPa/Hz<sup>1/2</sup>, and a large dynamic range of 59 dB. As the MZI is not a resonator, unlike a RR, there is no field enhancement. Higher op-

tical powers may therefore be used without the penalty of strong nonlinear effects. Since the noise level increases slower than the sensitivity with increasing optical input power, higher optical power gives a smaller detection limit. In addition, the transmission characteristic of the MZI is gradual, instead of sharp as for the resonances of the RR. This allows a more robust operation of the sensor. However, the MZI sensor also has a drawback in comparison with the RR sensor. The spiral on the membrane should be long enough to ensure proper sensitivity, which limits the minimum footprint of the sensor. For a RR, the strain induced resonance-wavelength shift does not depend on the length of the racetrack [2, 3]. Assuming a constant quality factor of the RR, the sensitivity of a RR sensor is independent of the RR size. Thus, the RR sensor can be very small without compromising the sensitivity. In the addendum of Chapter 3, the effect of buckling of the membrane is discussed, along with a measurement of the degree of buckling of a dummy membrane. Buckling exists for both the RR sensor and the MZI sensor. The cause of the buckling and its influence on the sensor acoustic properties are discussed.

In Chapter 4, a design method for silicon RRs with a free spectral range robust to fabrication variations is presented. The method includes two steps: i) Estimating the systematic deviation of the waveguide width from the design value using transmission measurement on test MZIs and simulation results. This step leads to calibrated design inputs, which give more accurate designs. ii) Using two waveguide widths in the RR with opposite signs of the derivative of the group index with respect to the width. This step results in compensating the FSR variations resulting from the fabrication-induced width variations superimposed on the systematic width deviation. Two robust design examples are fabricated and characterized. Experimental results show that the robustly designed RRs have clearly smaller FSR variation and FSR deviation from the design value. For a deliberately introduced  $\pm 10$  nm width change, the FSR variations of the robust RRs are only about 30% of the value measured from the normal design RRs. In the addendum of this chapter, a similar robust design method is proposed for silicon MZIs. Quantitative predictions show that the method works for MZIs as well. These generic design methods for RRs and MZIs do not require adjustment of the fabrication process and can be applied to improve the performance of PICs using multiple RRs and MZIs.

## 5.2. OUTLOOK

In the three subsections of this outlook, three promising developments are sketched as possible directions for continuation of this research, two based on the MZI ultrasound sensor and one based on the RR ultrasound sensor.

### 5.2.1. APPLYING THE MZI ULTRASOUND SENSOR TO INTRAVASCULAR PHOTOACOUSTIC IMAGING

Intravascular photoacoustic imaging (IVPA) is a technique for characterizing atherosclerotic plaques, which are mainly health-threatening lipids on the wall of an artery. IVPA provides useful information for preventing rupture of vulnerable plaques [4–6]. In IVPA, the arterial wall is irradiated by short monochromatic laser pulses. The pulses are selectively absorbed by certain constituents of the wall's tissue, resulting in generation of ultrasound waves. These waves are usually detected with a conventional (i.e., piezoelectric)



ultrasound transducer, leading to an image. The advantage of IVPA is that it provides not only the resolution and the viewing depth of ultrasound, but also the chemical specificity of optical absorption [6]. Thus, IVPA not only provides information on the geometrical structure of the artery, but also on its chemical composition.

It is proposed here to apply the integrated photonics MZI sensor developed in Chapter 3, with all its merits, to IVPA. This leads to a very promising all-photonics solution for IVPA, with the piezoelectric transducer for detecting ultrasound waves being replaced by the MZI sensor. An IVPA catheter with the MZI sensor can be built by adding the sensor to the usual fiber arrangement for delivering the laser pulses, similar as done in [7] by adding a polymer RR sensor. A configuration for such a catheter is suggested in Figure 5.1. The diameter of the catheter should be within 1 mm. This is certainly feasible, because the footprint of the sensor is small enough and only three fibers are needed (two for the sensor and one for the laser pulses).

To fulfill the requirements of IVPA, the sensor properties need to be tailored. As discussed in the addendum of Chapter 3, the sensitivity and resonance frequency of the sensor depend on the buckling of the membrane, and there is also the question of the relation between the oscillations in the directivity and the buckling. Thus, the effects of the initial stress in the layers on the mechanical properties of the resulting membrane should be further researched for a better membrane design. A stress-balanced membrane can be obtained by depositing a  $\text{Si}_3\text{N}_4$  layer with tensile stress on top of the chip, which compensates the compressive stress of the (thinned)  $\text{SiO}_2$  layer. The membrane should further be re-designed for a higher resonance frequency, because most of the acoustic energy emitted by coronary atherosclerotic plaque lies in the frequency range of 2-8 MHz [8]. This can be achieved by changing the lateral dimensions of the membrane, since a smaller membrane gives a higher resonance frequency. The bandwidth of the present MZI sensor (21.2% at -6 dB) is limiting the axial resolution of the imaging. A larger bandwidth can be obtained by depositing a lossy layer on the membrane, for example, a polymer layer. The effect of this layer on the resonance frequency should be taken into account in the design phase. These adaptations for the resonance frequency and bandwidth will lead to a lower sensitivity. But the sensitivity can be simply increased by using a higher optical input power.

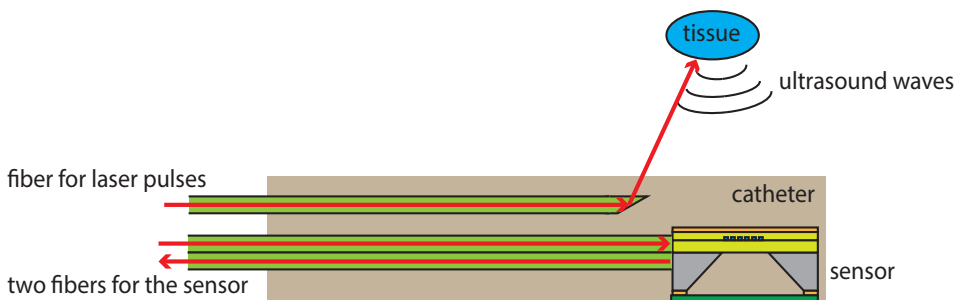


Figure 5.1: Configuration of an all-photonics catheter for IVPA using the integrated photonics MZI sensor. Three fibers are used in the catheter: one for the laser pulses, two for the sensor input and output.

### 5.2.2. DEVELOPING AN ARRAY OF MZI ULTRASOUND SENSORS

In modern ultrasound imaging, an array of ultrasound transducers is often needed [9]. An array of MZI sensors can be realized on chip.

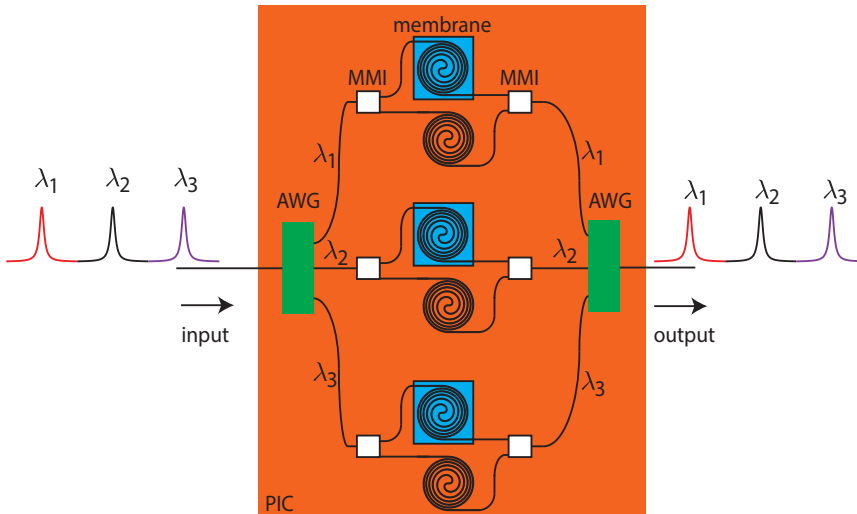


Figure 5.2: Schematic of an array of three MZI ultrasound sensors and related circuitry with MMIs and AWGs. Light is coupled in and out of the chip using two single mode fibers.  $\lambda_1$ ,  $\lambda_2$  and  $\lambda_3$  are the operation wavelengths of the three sensors. Two arrayed waveguide gratings (AWGs) are used on-chip for (de)multiplexing. The array of the three sensors and circuitry can fit in a  $1\text{mm} \times 1\text{mm}$  chip.

An example of MZI sensor array, here with three elements, is presented in Figure 5.2. The elements are identical by design. The number of elements and their spacing can be chosen depending on the application. The configuration of Figure 5.2 requires only two fibers for coupling light in and out of the chip, thus avoiding a relatively large fiber array unit. The input and output grating couplers (not shown) can be put on the same side of the chip if needed. CW laser light of wavelengths  $\lambda_1$ ,  $\lambda_2$  and  $\lambda_3$ , which are the operation wavelengths of the three sensors for maximum sensitivity, can be coupled into the chip through an optical multiplexer. Channel position and spacing of the multiplexer should match with the operation wavelengths. Very accurate tuning of the operation wavelength is not required, owing to the gradual shape of the MZI transmission spectrum. Therefore, distributed feedback (DFB) lasers, which can be tuned with a heater across a range of several nanometers [10], are very suitable and cost effective external light sources. By choosing a proper FSR of the MZIs, an optimum operation wavelength can always be found in the tuning range of the DFB lasers. Two identical arrayed waveguide gratings (AWGs) [11] are included for wavelength demultiplexing and multiplexing on chip. Therefore,  $\text{FSR}/2$  of the MZIs should be smaller than the channel bandwidth of the AWG, to arrange that the operation wavelengths can be sent to and taken out of the corresponding MZI. In general, proper matching of all components needs to be taken care of during the design. Ultra-

sound waves arriving at each element of the array can be detected from the modulation of the optical power at the three wavelengths, similar as described in Chapter 3. The number of AWG channels limits the number of elements in the array. Design trade-offs between the AWG properties, such as the number of channels, footprint, channel spacing and FSR of the AWG, should be considered at the design phase [12]. The AWGs can be replaced by cascaded MZIs to fulfill the same function [13]. Fabrication and thermal tolerances of the cascaded MZIs can be maximized for high performance by following the design methods in [14].

### 5.2.3. DEVELOPING AN ARRAY OF RR SENSORS AND ITS INTERROGATOR

Compared with the MZI ultrasound sensor, the RR ultrasound sensor has advantages for applications that require a very small device footprint. The reason is that the sensitivity of the RR sensor does not depend on the length of the strain-sensitive section of the racetrack (assuming that the whole racetrack is on the membrane and the quality factor does not depend on the racetrack length).

5

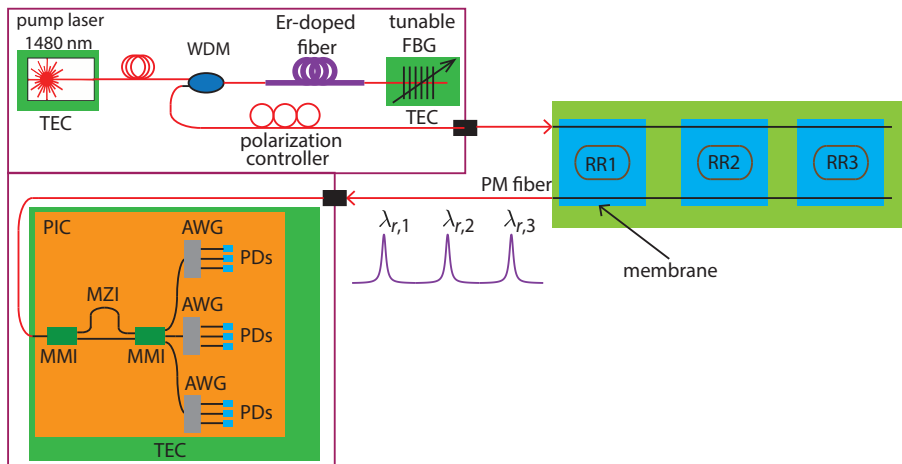


Figure 5.3: Schematic of an array of three RR ultrasound sensors on chip (right), connected to an interrogator (left). The interrogator has a tunable light source with a high power density (upper part). The tunability and the bandwidth of the light source are determined by the fiber Bragg grating (FBG). PIC of the interrogator is in the lower part, which comprises an MZI with three AWGs and nine integrated photodetectors (PDs).

An array of RR ultrasound sensors can be built in the configuration in Figure 5.3, which was already demonstrated for polymer RR sensors [15]. The proposed interrogator is also shown in the figure. Since the RR properties, especially the resonance wavelengths, are very sensitive to fabrication variations [16], robust design approaches [17] or improved fabrication are needed for the realization of a useful sensor array of this type. The three resonance wavelengths  $\lambda_{r,1}$ ,  $\lambda_{r,2}$  and  $\lambda_{r,3}$  of the three RRs should be equally and well separated. The light source of this interrogator is similar to that of MediGator in Chapter 2. But its bandwidth and the FSR of each RR should be such that only one resonance peak of each

sensor is sent to the MZI of the interrogator. For demultiplexing, each of the three outputs of the MMI is connected to an AWG. The channel spacing of the AWGs should match the spacing of  $\lambda_{r,1}$ ,  $\lambda_{r,2}$  and  $\lambda_{r,3}$ . Three interrogator signals (corresponding to  $V_1$ ,  $V_2$  and  $V_3$  in Chapter 2) of each sensor are measured at the outputs of the three AWGs using photodetectors (PDs). The interrogation procedure is also similar to that of MediGator. The variation of the specifications of the AWGs and the PDs should be as small as possible for a good performance. This again requires robust design methods or precise fabrication.

## REFERENCES

- [1] S. M. Leinders, W. J. Westerveld, J. Pozo, P. Van Neer, B. Snyder, P. O'Brien, H. P. Urbach, N. de Jong, and M. D. Verweij, *A sensitive optical micro-machined ultrasound sensor (OMUS) based on a silicon photonic ring resonator on an acoustical membrane*, Scientific Reports **5** (2015), p. 14328.
- [2] W. J. Westerveld, J. Pozo, P. J. Harmsma, R. Schmits, E. Tabak, T. C. van den Dool, S. M. Leinders, K. W. van Dongen, H. P. Urbach, and M. Yousefi, *Characterization of a photonic strain sensor in silicon-on-insulator technology*, Optics Letters **37** (2012), pp. 479–481.
- [3] W. J. Westerveld, S. M. Leinders, P. M. Muilwijk, J. Pozo, T. C. van den Dool, M. D. Verweij, M. Yousefi, and H. P. Urbach, *Characterization of integrated optical strain sensors based on silicon waveguides*, IEEE Journal of Selected Topics in Quantum Electronics **20** (2013), pp. 101–110.
- [4] B. Wang, J. L. Su, A. B. Karpouk, K. V. Sokolov, R. W. Smalling, and S. Y. Emelianov, *Intravascular photoacoustic imaging*, IEEE Journal of Selected Topics in Quantum Electronics **16** (2010), pp. 588–599.
- [5] K. Jansen, A. F. Van Der Steen, H. M. van Beusekom, J. W. Oosterhuis, and G. van Soest, *Intravascular photoacoustic imaging of human coronary atherosclerosis*, Optics Letters **36** (2011), pp. 597–599.
- [6] K. Jansen, G. van Soest, and A. F. W. van der Steen, *Intravascular photoacoustic imaging: a new tool for vulnerable plaque identification*, Ultrasound in Medicine & Biology **40** (2014), pp. 1037–1048.
- [7] B.-Y. Hsieh, S.-L. Chen, T. Ling, L. J. Guo, and P.-C. Li, *Integrated intravascular ultrasound and photoacoustic imaging scan head*, Optics Letters **35** (2010), pp. 2892–2894.
- [8] V. Daeichin, M. Wu, N. De Jong, A. F. van der Steen, and G. van Soest, *Frequency analysis of the photoacoustic signal generated by coronary atherosclerotic plaque*, Ultrasound in Medicine & Biology **42** (2016), pp. 2017–2025.
- [9] T. L. Szabo, *Diagnostic ultrasound imaging: inside out* (Academic Press, 2004).
- [10] S. Sakano, T. Tsuchiya, M. Suzuki, S. Kitajima, and N. Chinone, *Tunable DFB laser with a striped thin-film heater*, IEEE Photonics Technology Letters **4** (1992), pp. 321–323.
- [11] M. K. Smit and C. Van Dam, *PHASAR-based WDM-devices: Principles, design and applications*, IEEE Journal of Selected Topics in Quantum Electronics **2** (1996), pp. 236–250.
- [12] S. Pathak, D. Van Thourhout, and W. Bogaerts, *Design trade-offs for silicon-on-insulator-based AWGs for (de)multiplexer applications*, Optics Letters **38** (2013), pp. 2961–2964.

- [13] F. Horst, W. M. Green, S. Assefa, S. M. Shank, Y. A. Vlasov, and B. J. Offrein, *Cascaded Mach-Zehnder wavelength filters in silicon photonics for low loss and flat pass-band WDM (de-) multiplexing*, *Optics Express* **21** (2013), pp. 11652–11658.
- [14] S. Dwivedi, H. D'heer, and W. Bogaerts, *Maximizing fabrication and thermal tolerances of all-silicon FIR wavelength filters*, *IEEE Photonics Technology Letters* **27** (2015), pp. 871–874.
- [15] C. Zhang, S.-L. Chen, T. Ling, and L. J. Guo, *Review of imprinted polymer microrings as ultrasound detectors: Design, fabrication, and characterization*, *IEEE Sensors Journal* **15** (2015), pp. 3241–3248.
- [16] W. Bogaerts, Y. Xing, and U. Khan, *Layout-aware variability analysis, yield prediction, and optimization in photonic integrated circuits*, *IEEE Journal of Selected Topics in Quantum Electronics* **25** (2019), pp. 1–13.
- [17] W. Bogaerts and L. Chrostowski, *Silicon photonics circuit design: methods, tools and challenges*, *Laser & Photonics Reviews* **12** (2018), p. 1700237.



# A

## APPENDIX A: THE CHIP LAYOUTS FOR THE TWO MULTI-PROJECT WAFER RUNS

With reference to the layouts of the two multi-project wafer (MPW) runs in Figure A.1, the photonic designs of the various areas are identified as follows.

### First MPW run:

- Chip dimension: 10.45 mm × 2.5 mm
- Areas 1, 3, 7: Test structures for characterizing the directional coupler
- Area 2: RRs for ultrasound sensors
- Areas 4, 8: Test MZIs for characterizing the systematic width deviation of the foundry
- Area 5: Small RRs for small pressure sensors
- Area 6: MZIs for ultrasound sensors
- Area 9: Structures for characterizing the strain-induced changes of waveguides

### Second MPW run:

- Chip dimension: 10.45 mm × 2.5 mm
- Area 1: Test cascaded MZIs for characterizing the systematic width deviation of the foundry
- Area 2: RRs with a free spectral range robust to fabrication variations. These RRs are for the air cladding case.



## A

- Area 3: MZIs with a free spectral range robust to fabrication variations. These MZIs are for the air cladding case.
- Area 4: MZIs with a free spectral range robust to fabrication variations. These MZIs are for the SiO<sub>2</sub> cladding case.
- Areas 5, 8: Test structures for characterizing the directional coupler
- Area 6: RRs for ultrasound sensors
- Area 7: MZIs for ultrasound sensors

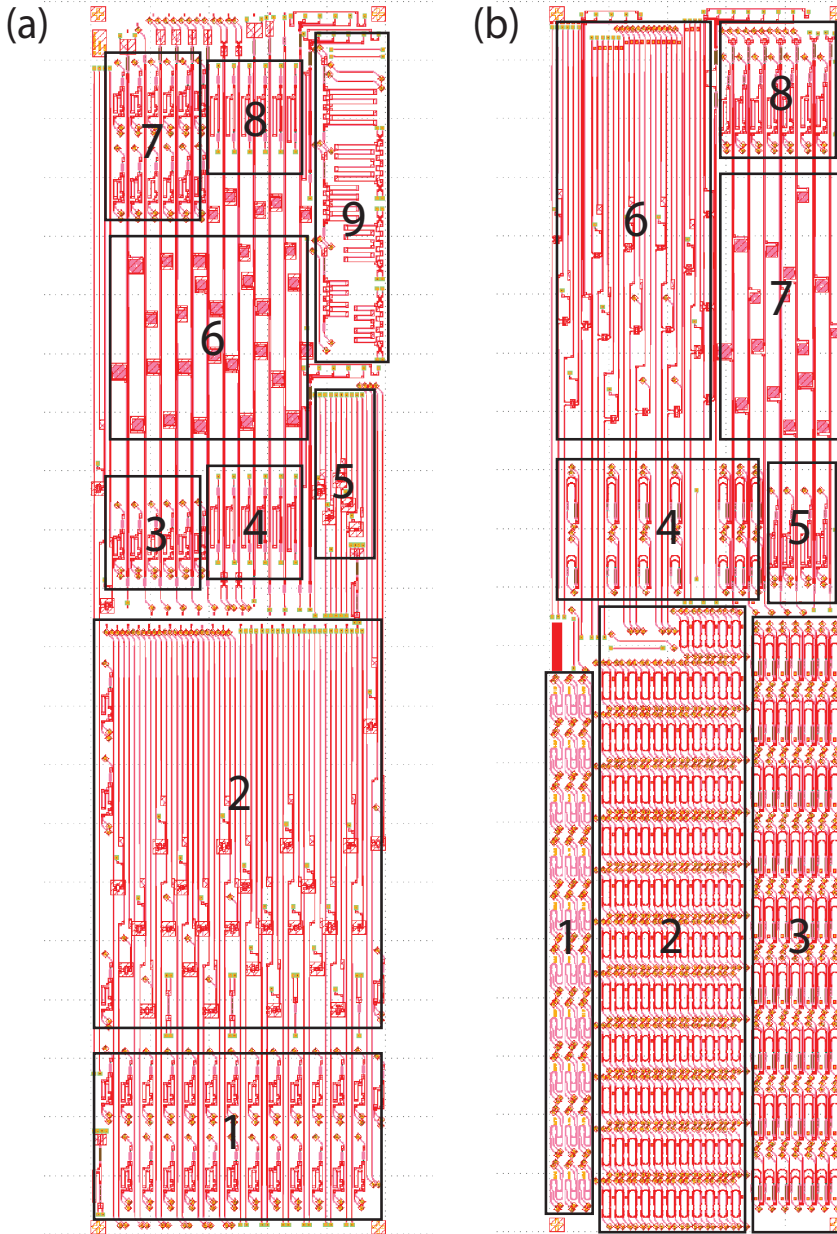


Figure A.1: Chip layouts of the multi-project wafer runs. The chip dimension is 10.45 mm  $\times$  2.5 mm. (a) chip for the first MPW run. (b) chip for the second MPW run. The numbered chip areas are explained in the text. Each chip has been rotated 90° anticlockwise compared to the regular design view.



# B

## APPENDIX B: POST-PROCESSING STEPS FOR SENSOR FABRICATION

The post-processing starts on 200 mm SOI wafers processed at IMEC through the Europractice MPW service (photonic structures etched in 220 nm device layer, 2  $\mu\text{m}$  BOX, 725  $\mu\text{m}$  thick substrate). In this stage, the front side of the wafer is covered by a photoresist layer, as protective coating. The steps are as follows.

1. Grinding and polishing of wafer, to a thickness of 250  $\mu\text{m}$ 
  - Resulting surface roughness:  $R_a \approx 0.7 \text{ nm}$
2. Dicing of wafer to dies
3. Removing photoresist from dies
  - sequence: acetone, IPA, DI water
  - drying with  $\text{N}_2$  gun
4. PECVD of 500 nm  $\text{SiO}_2$  on front side of die (upper cladding)
  - reactor: Plasmalab 80 Plus, Oxford Instruments
  - $T = 300^\circ\text{C}$
  - $\text{SiH}_4$ , 8.5 sccm
  - $\text{N}_2$ , 162.5 sccm
  - $\text{N}_2\text{O}$ , 710 sccm
  - pressure 1000 mTorr
  - RF power 20 W
  - dep. rate about 70  $\mu\text{m}/\text{min}$
5. RCA-1 clean, 10 min

6. Rinsing in H<sub>2</sub>O
7. RCA-2 clean, 10 min
8. Rinsing in H<sub>2</sub>O
9. Drying on spinner
10. LPCVD of 150 nm Si<sub>3</sub>N<sub>4</sub> (two-sided deposition of “low stress” silicon nitride: 200 ±75 MPa; the Si<sub>3</sub>N<sub>4</sub> layer serves as mask during etching in KOH)
  - reactor: Tempress Furnaces, Tempress Systems
  - T = 850°C
  - SiH<sub>2</sub>Cl<sub>2</sub> : NH<sub>3</sub> = 10 : 3
  - dep. rate about 3-5 nm/min
11. Spin coating photoresist on backside
  - HMDS, 5000 rpm + 200°C bake for 2 mins
  - AZ 5214, 5000 rpm + 90°C bake for 1 min (layer thickness 1.4 μm)
12. Lithography on backside
  - mask aligner: EVG-620 NUV, EV Group
  - Alignment using markers on front side
  - soft contact exposure
  - exposure time 8 sec
13. Developing resist
  - MF321 developer, 60 sec
  - rinsing in H<sub>2</sub>O, 30 sec
  - drying with N<sub>2</sub> gun
14. Reactive ion etching of 150 nm Si<sub>3</sub>N<sub>4</sub> (to open mask for etch in KOH)
  - Etcher: Leybold Fluor F1, Leybold Heraeus
  - CHF<sub>3</sub>, 25 sccm
  - Ar, 25 sccm
  - pressure 8 μbar
  - RF power 50 W
  - bias voltage -600 V
  - etch rate about 21 nm/min
15. Spin coating of photoresist on front side (protective coating for dicing)
  - S1813, 3000 rpm + 120°C bake for 5 mins

16. Dicing to final chip dimension
17. Stripping photoresist
  - fuming  $\text{HNO}_3$ , 5 mins
  - rinsing in  $\text{H}_2\text{O}$
  - drying with  $\text{N}_2$  gun
18. Anisotropic etching of silicon in KOH, to form membrane
  - etching solution: 33% KOH in water, by weight
  - $T = 85^\circ\text{C}$
  - stirring 3 rpm
  - etch rate about  $100\ \mu\text{m}/\text{hr}$
  - The reaction gives bubbles. When the bubbling stops, giving clearance of the etched hole, the BOX layer has been reached and the chip is taken out of the solution.
19. Cleaning, to remove KOH residues
  - rinsing in diluted HCl
  - rinsing in  $\text{H}_2\text{O}$ , using a sequence of several beakers
  - Let chip carefully dry in wet bench, without using  $\text{N}_2$  gun, to avoid possible damage to the membrane.



# C

## APPENDIX C: PACKAGING STEPS FOR THE SILICON MZI ULTRASOUND SENSOR

After the post-processing in the cleanroom, the MZI sensor is packaged in our lab for the characterization experiments. The packaging procedure described here can be used for the RR ultrasound sensor as well. Photographs of the top view and the side view of the packaged sensor are presented in Figure [C.1](#).

The packaging steps are listed below:

1. Prepare the polyvinyl chloride (PVC) holder and a clean glass plate that can be fitted in the PVC holder.
2. Place the chip on the glass plate and apply UHU epoxy glue (UHU plus endfest, Bolton Group) at the long edges of the photonic chip for mounting it on the glass plate. Let the UHU cure for 7 hours.
3. Place the glass plate with photonic chip on the stage of the grating coupler setup (GC setup), for transmission measurements. Align the two almost vertical fibers of the setup to the input and output GC for maximum transmission of the MZI.
4. Perform a wavelength sweep to obtain the transmission spectrum of the MZI and fix the wavelength at a transmission maximum.
5. Replace the vertical fiber on the output GC by an angle polished fiber with an aluminum coating on its facet (angle polished fiber on the translation stage). The axis of the fiber is oriented horizontally.
6. Align the angle polished fiber to the output GC for maximum transmission, using the translation stage.



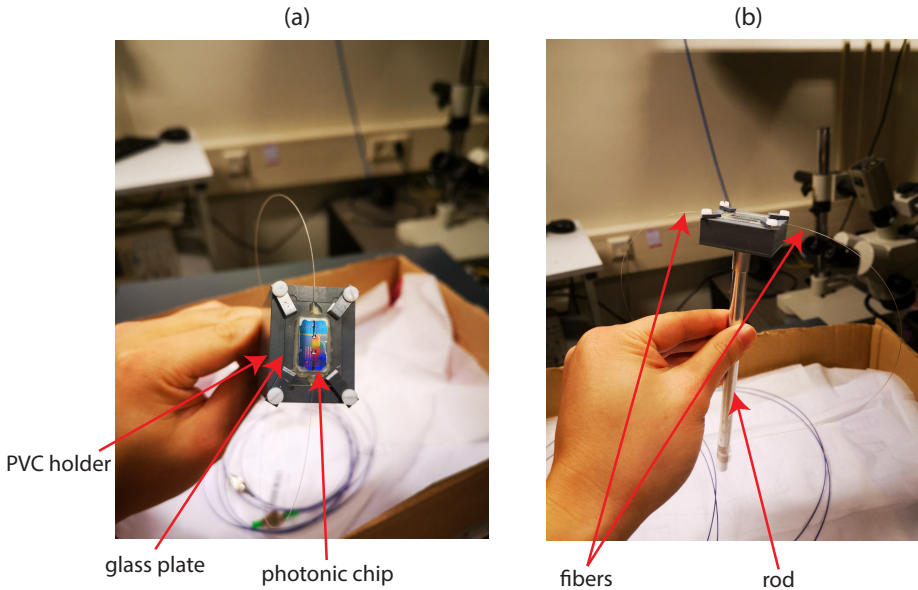


Figure C.1: Photographs of the packaged MZI ultrasound sensor. (a) top view and (b) side view. The PVC holder, glass plate, photonic chip, fibers, and the rod are indicated.

7. Apply a small amount of UV curable glue (NOA 61, Norland Products Inc.) to the angled tip of the fiber. Applying the glue may lead to a small misalignment between fiber and GC. Therefore, some re-alignment of the fiber may be needed before curing the glue, guided by the transmission level.
8. Illuminate the glue with UV light for 1 min, for curing.
9. Replace the vertical fiber on the input GC by a second angle polished fiber.
10. Repeat steps 6 – 8 for the second fiber on the input GC.
11. Apply UHU epoxy glue to the part of the angled polished fibers without coating layer, thus covering that part for protection and reinforcement purposes. Also apply UHU epoxy glue at the two short edges of the chip, to completely seal the chip. Let the UHU cure for 7 hours. In this way water cannot enter the etched hole under the membrane when the chip is immersed in water for sensing experiments.
12. Clamp the glass plate with chip on the PVC holder, using the 4 clamps. Attach the rod to the holder. Now the situation of the photographs in Figure C.1 of this Appendix has been reached.

The location of the chip on the glass plate and the location of the glass plate on the PVC holder should be chosen such that the membrane of the sensor is centered on the axis

of the rod. This is important, since in the sensing experiments the membrane and the ultrasound transducer should be coaxially mounted in a U-shaped frame (see Chapter 3).



# ACKNOWLEDGEMENT

Finally, the thesis writing comes to this part. When I put my hands on the keyboard, all the memories are flashing in front of my eyes. It is my pleasure to thank everyone who has offered me help and guidance to get this work done.

My thanks first go to **Prof. Paul Urbach**. I initially contacted you for a master project in TU Delft. Then you forwarded my application to **Dr. Jaap Caro** and I got the chance to do the master project in Imphys, which later extended to a Ph.D. project.

I would like to give my special thanks to **Dr. Jaap Caro**, my daily supervisor during the Ph.D. period. When I started this work, I did not know much about integrated photonics. You really took time to guide me into this field. We have spent a lot of time together on discussing the design, fabrication and experiment related to my work. You valued my ideas and always gave useful and critical feedback. Ph.D. period has many up and down times. I sometimes get pushing when feeling worried. I remember that you once said: "Boling, you are the type of Ph.D. students who push their supervisors." Even in this case, you were still patient with me, trying to help me out and cheer me up. Thank you for all your support and guidance. I also want to express my gratitude to my promoter, **Prof. Lucas van Vliet**. You actively monitored my Ph.D. progress and helped me solve many problems to get this thesis done. The monthly meeting with you was always fruitful because the suggestions given by you inspired me greatly.

Many faculty members have offered me great help. **Prof. Bernd Rieger**, **Prof. Sjoerd Stallinga**, **Dr. Frans Vos** and **Dr. Jeroen Kalkman** have provided me useful feedback during the QI seminars. **Dr. Koen W. A. van Dongen** has guided me into the ultrasound field and answered all my acoustic related questions. I am happy that I joined the IEEE-UFFC summer school with you and I have learned a lot from there.

I am grateful to the staff members who have provided me invaluable help. **Annelies** and **Angela** were always patient and efficient in helping me with all the issues. **Ron**, the customized mechanic components you made for my experiment setup worked perfectly. **Roland**, the master of LabView, your photo is still in the lab right next to the NI machine programmed by you. Because the machine only works properly under your supervision. **Ronald**, your technical support was very helpful. **Henry**, your help with the measurement equipment was valuable. **Nicolette**, your management of the whole Imphys department is great.

I would like to recognize the invaluable assistance that people provided to me in the cleanroom. **Marc**, **Charles**, **Eugene**, **Pauline**, **Ewan**, **Marco**, **Anja**, **Roel** and **Hozanna**, thank you for introducing me to the cleanroom equipment and helping me with all the issues that I encountered there. **Mariya**, your advice for developing my sensor fabrication recipe was really helpful. Sometimes I feel the cleanroom is like a dungeon, since there is no daylight and I can easily be trapped there for one whole day without any good results. But I am glad that I have all your help and I got very good results in the end.

I am grateful to **Prof. Roel Baets, Prof. Wim Bogaerts, Yanlu and Yufei** from Ghent University. I visited Ghent quite often and the assistance I got from you was invaluable. I want to thank **Michael, Elvis and Pim** for working together to build the MediGator. I would not be able to do that without your help. **Luis**, thanks for guiding me to Opto-designer. I have used it to generate all my design layouts. **Dejan**, thank you for helping me build an in-house vibrometer. **Behnam**, thanks for helping me with the linear scanner. **Wouter**, thanks for your ring design. I also want to thank **Erwin** for helping me with this beautiful cover of my thesis. It nicely reflects the content of the work.

Special thanks go to colleagues at Impphys. **Fellipe**, you were my daily supervisor during the master project and your guidance was valuable. **Aloys**, you are my first master student. The packaging method developed by you resulted in the first underwater measurement of our sensor. **Marten**, I really enjoyed pushing our sensors for imaging applications with you. We generated the first ultrasound image using the MZI sensor. **Ulas**, your help with the acquisition system bought me good results. **Gyllion, Mohammad, Jeroen Heldens and Arnica**, I enjoyed working with you in the “Jaap team”. **Gyllion and Jos van Rooij**, we shared the office for more than 4 years and had many interesting discussions and table soccer competitions. **Tian**, you are like the big brother to me. We shared many happy moments and went through tough times together. **Pierre, Leon, Jos de Wit, Jelle van der Horst, Jin, Dong, Junhai, Tiexing, Shan, Tian, Gyllion and Jos van Rooij**, you have made my time after lunch become the relaxing table soccer time. **Robert Moerland, Christiaan and Taylor**, I like the beer, BBQ and hotpot time we had together. **Yan Guo**, you are not only a good colleague but also a good neighbour. **Shan, Junhai, Tiexing, Dong, Sixue, Wenxiu and Kefei**, we always joked with each other while eating lunch together. **Shan**, we all like to drink beer and play table tennis in your place. **Junhai**, the noodles you made is really delicious. **Tiexing**, I enjoyed playing basketball and drinking beer with you. **Dong**, I hope you have learned all my table soccer skills. **Sixue**, I hope we will find another time to taste a bottle of good wine with the whole “lunch team” together. **Wenxiu**, your skill in making jokes improves very fast. **Kefei**, “black coffee”, I look forward to the Dongbei journey you promised to me. I also want to thank **Robert Nieuwenhuizen, Jeroen van Schie, Hamid, Joor, Mojtaba, Nadya, Lena, Anna, Willem, Babak, Tom, Juan, Rasmus, Jelle Storteboom, Dirk and Martijn** for being supportive.

I want to express my gratitude to all my Chinese friends in The Netherlands. **Yifeng**, you are the one who took me to the social life in Delft when I arrived. **Meng**, you are a good teammate for playing cards. **Fei and Jiao**, playing Mahjong in your place always gave me perfect Friday nights. **Jin and Yun**, you are always willing to help me when needed. I enjoyed hanging out with you. **Min and Qian**, you have rich experience in dealing with issues that a Chinese may encounter in The Netherlands and have helped me a lot. **Chuyi and Yang**, my classmates when I was an undergraduate student, we call us “three idiots in The Netherlands” and have spent many weekends travelling in and around The Netherlands. The first time I heard about TU Delft was from **Chuyi**, when he was applying for the master study in Delft. Two years later, I also came here. **Yue and Rong**, it is amazing to know you since we all come from the same high school and study in TU Delft. We can even communicate with each other using our dialect, which makes me feel like back to my hometown. We had a lot of spicy food to comfort the homesick stomach together with **Jun**, who has low tolerance to the spicy food but joined every time. I also learned a lot

from **Ying, Zhe, Lei, Zhongwen, Zheng, Xukang, Min** and **Peiwen**.

I sincerely thank my parents and parents-in-law for their encouragement, support, love and care. No matter which way I choose to go, I know that you will always back me up and provide me a warm harbour for a rest when I am tired. Finally, my deepest gratitude goes to my wife, **Yan Xu**. It's my greatest fortune to meet you at the beginning of my Ph.D. time. I would not be able to finish this thesis without your support. The long-distance relationship is hard, but we never give it up. The new journey is about to start. I feel so blessed to be able to spend the rest of my life with you.

Boling Ouyang  
May, 2020



# CURRICULUM VITAE

## **Boling OUYANG**

09-Mar-1992      Born in Hengyang, Hunan, China.

### EDUCATION

2006–2009      High School  
Hengyang No. 8 High School, Hengyang, China

2009–2013      B.Sc. in Information Engineering  
South China University of Technology, Guangzhou, China

2013–2015      M.Sc. in Nanoscale Engineering (Summa Cum Laude)  
École Centrale de Lyon, Écully, France

2015–2020      Ph.D. in Applied Science  
Delft University of Technology, Delft, The Netherlands





# LIST OF PUBLICATIONS

- 1 **B. Ouyang**, Y. Li, M. Kruidhof, R. Horsten, R. Baets, K. W. A. van Dongen, and J. Caro, *Highly sensitive silicon Mach-Zehnder interferometer-based ultrasound sensor*, in *Proceedings SPIE 11283, Integrated Optics: Devices, Materials, and Technologies XXIV* (SPIE, 2020) 11283R.
- 2 **B. Ouyang**, Y. Xing, W. Bogaerts, and J. Caro, *Silicon ring resonators with a free spectral range robust to fabrication variations*, *Optics Express* **27** (2019), pp. 38698-38707.
- 3 **B. Ouyang**, M. Haverdings, R. Horsten, M. Kruidhof, P. Kat, and J. Caro, *Integrated photonics interferometric interrogator for a ring-resonator ultrasound sensor*, *Optics Express* **27** (2019), pp. 23408-23421.
- 4 **B. Ouyang**, Y. Li, M. Kruidhof, R. Horsten, K. W. A. van Dongen, and J. Caro, *On-chip silicon Mach-Zehnder interferometer sensor for ultrasound detection*, *Optics Letters* **44** (2019), pp. 1928-1931.
- 5 **B. Ouyang**, W. Bogaerts, and J. Caro, *Design of silicon Mach-Zehnder interferometer and ring resonator with a free spectral range tolerant against waveguide-width variations*, in *Proceedings Symposium IEEE Photonics Benelux Chapter* (2018).
- 6 F. G. Peternella, **B. Ouyang**, R. Horsten, M. Haverdings, P. Kat, and J. Caro, *Interrogation of a ring-resonator ultrasound sensor using a fiber Mach-Zehnder interferometer*, *Optics Express* **25** (2017), pp. 31622-31639.